

**THE ENIGMA OF IMAGING IN THE  
MAXWELL FISHEYE MEDIUM**

**Sahar Sahebdivan**

**A Thesis Submitted for the Degree of PhD  
at the  
University of St Andrews**



**2016**

**Full metadata for this item is available in  
St Andrews Research Repository  
at:**

**<http://research-repository.st-andrews.ac.uk/>**

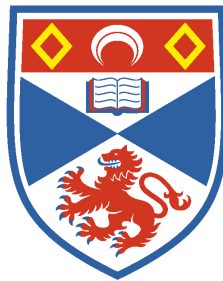
**Please use this identifier to cite or link to this item:  
<http://hdl.handle.net/10023/9894>**

**This item is protected by original copyright**

**This item is licensed under a  
Creative Commons Licence**

# **The Enigma of Imaging in the Maxwell Fisheye Medium**

**Sahar Sahebdivan**



University of  
St Andrews

This thesis is submitted in partial fulfilment for the degree of PhD

at the

University of St Andrews

March 2016



UNIVERSITY OF ST ANDREWS

DOCTORAL THESIS

# The Enigma of Imaging in The Maxwell Fisheye Medium

---

*Author:*

Sahar SAHEBDIVAN(1)

*Supervisor:*

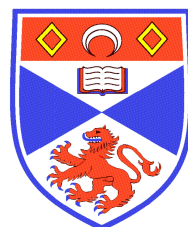
Dr. Natalia KOROLKOVA

Prof. Ulf Leonhardt

*A thesis submitted in fulfilment of the requirements  
for the degree of Doctor of Philosophy in Theoretical Physics*

*in the*

School of Physics and Astronomy



University  
of  
St Andrews

**1. Candidate's declarations:**

I, Sahar Sahebdivan(i), hereby certify that this thesis, which is approximately 25,000 words in length, has been written by me, and that it is the record of work carried out by me, or principally by myself in collaboration with others as acknowledged, and that it has not been submitted in any previous application for a higher degree.

I was admitted as a research student in October 2009 and as a candidate for the degree of Doctor of Philosophy in October 2009 the higher study for which this is a record was carried out in the University of St Andrews between 2009 and 2014 and also at the in University of Vienna, as a visiting student, between 2012 and 2014.

**Sahar Sahebdivan**

**2. Supervisor's declaration:**

I hereby certify that the candidate has fulfilled the conditions of the Resolution and Regulations appropriate for the degree of Doctor of Philosophy in Theoretical Physics in the University of St Andrews and that the candidate is qualified to submit this thesis in application for that degree.

**Prof Ulf Leonhardt**

**Dr Natalia Korolkova**

**3. Permission for publication:**

In submitting this thesis to the University of St Andrews I understand that I am giving permission for it to be made available for use in accordance with the regulations of the University Library for the time being in force, subject to any copyright vested in the work not being affected thereby. I also understand that the title and the abstract will be published, and that a copy of the work may be made and supplied to any bona fide library or research worker, that my thesis will be electronically accessible for personal or research use unless exempt by award of an embargo as requested below, and that the library has the right to migrate my thesis into new electronic forms as required to ensure continued access to the thesis. I have obtained any third-party copyright permissions that may be required in order to allow such access and migration, or have requested the appropriate embargo below.

The following is an agreed request by candidate and supervisor regarding the publication of this thesis:

Access to printed copy and electronic publication of the thesis through the University of St Andrews.

**Sahar Sahebdivan**

**Prof Ulf Leonhardt**

**Dr Natalia Korolkova**

*I appreciate my supervisors Prof Ulf Leonhardt and Dr Natalia Korolkova for all of their supports during the years of my study. I am also thankful to the University of Vienna for their generous hospitality in hosting me, particularly Prof Markus Aspelmeyer and Prof Anton Zeilinger. I acknowledge Prof Tomáš Tyc for his scientific collaboration during the project of the perfect imaging and also hosting me for a short visit to the Masaryk University, Brno, Czech Republic.*

Sahar Sahebdivan

*To Mahmood and Alois*

UNIVERSITY OF ST ANDREWS

## *Abstract*

School of Physics and Astronomy

Doctor of Philosophy in Theoretical Physics

### **The Enigma of Imaging in The Maxwell Fisheye Medium**

by Sahar SAHEBDIVAN(I)

The resolution of optical instruments is normally limited by the wave nature of light. Circumventing this limit, known as the diffraction limit of imaging, is of tremendous practical importance for modern science and technology. One method, super-resolved fluorescence microscopy was distinguished with the Nobel Prize in Chemistry in 2014, but there is plenty of room for alternatives and complementary methods such as the pioneering work of J. Pendry on the perfect lens based on negative refraction that started the entire research area of metamaterials. In this thesis, we have used analytical techniques to solve several important challenges that have risen in the discussion of the microwave experimental demonstration of absolute optical instruments and the controversy surrounding perfect imaging. Attempts to overcome or circumvent Abbe's diffraction limit of optical imaging, have traditionally been greeted with controversy. In this thesis, we have investigated the role of interacting sources and detectors in perfect imaging. We have established limitations and prospects that arise from interactions and resonances inside the lens. The crucial role of detection becomes clear in Feynman's argument against the diffraction limit: "as Maxwell's electromagnetism is invariant upon time reversal, the electromagnetic wave emitted from a point source may be reversed and focused into a point with point-like precision, not limited by diffraction." However, for this, the entire emission process must be reversed, including the source: A point drain must sit at the focal position, in place of the point source, otherwise, without getting absorbed at the detector, the focused wave will rebound and the superposition of the focusing and the rebounding wave will produce a diffraction-limited spot. The time-reversed source, the drain, is the detector which takes the image of the source. Experiments with microwaves [1, 2] have confirmed the role of detection in perfect focusing. The emitted radiation was actively time-reversed and focused back at the point of emission, where, the time-reversed source sits. Absorption in the drain localizes the radiation with a precision much better than the diffraction limit. Absolute optical

instruments may perform the time reversal of the field with perfectly passive materials and send the reversed wave to a different spatial position than the source. Perfect imaging with absolute optical instruments is defected by a restriction: so far it has only worked for a single-source single-drain configuration and near the resonance frequencies of the device. In chapters 6 and 7, we have investigated the imaging properties of mutually interacting detectors [3, 4]. We found that an array of detectors can image a point source with arbitrary precision. However, for this, the radiation has to be at resonance. Our analysis has become possible thanks to a theoretical model for mutually interacting sources and drains we developed after considerable work and several failed attempts. Modelling such sources and drains analytically had been a major unsolved problem, full numerical simulations have been difficult due to the large difference in the scales involved (the field localization near the sources and drains versus the wave propagation in the device). In our opinion, nobody was able to reproduce reliably the experiments [5], because of the numerical complexity involved. Our analytic theory draws from a simple, 1-dimensional model [3] we developed in collaboration with Tomas Tyc (Masaryk University) and Alex Kogan (Weizmann Institute). This model was the first to explain the data of experiment [1], characteristic dips of the transmission of displaced drains, which establishes the grounds for the realistic superresolution of absolute optical instruments. As the next step in Chapter 7 we developed a Lagrangian theory that agrees with the simple and successful model [4] in 1-dimension. Inspired by the Lagrangian of the electromagnetic field interacting with a current, we have constructed a Lagrangian that has the advantage of being extendable to higher dimensions in our case two where imaging takes place. Our Lagrangian theory represents a device-independent, idealized model independent of numerical simulations. To conclude, Feynman [6] objected to Abbe's diffraction limit [7], arguing that as Maxwell's electromagnetism is time-reversal invariant, the radiation from a point source may very well become focused in a point drain. Absolute optical instruments [7] such as the Maxwell Fisheye can perform the time reversal and may image with a perfect resolution. However, the sources and drains in previous experiments [5, 8] were interacting with each other as if Feynman's drain would act back to the source in the past. Different ways of detection might circumvent this feature. The mutual interaction of sources and drains does ruin some of the promising features of perfect imaging. Arrays of sources are not necessarily resolved with arrays of detectors [4], but it also opens interesting new prospects [4] in scanning near fields from far-field distances. To summarise the novel idea of the thesis:

- We have discovered and understood the problems with the initial experimental demonstration of the Maxwell Fisheye [2].

- We have solved a long-standing challenge of modelling the theory for mutually interacting sources and drains [3, 4].
- We understand the imaging properties of the Maxwell Fisheye in the wave regime.

Let us add one final thought. It has taken the scientific community a long time of investigation and discussion to understand the different ingredients of the diffraction limit. Abbe's limit was initially attributed to the optical device only. But, rather all three processes of imaging, namely illumination, transfer and detection, make an equal contribution to the total diffraction limit. Therefore, we think that for violating the diffraction limit one needs to consider all three factors together. Of course, one might circumvent the limit and achieve a better resolution by focusing on one factor, but that does not necessarily imply the violation of a fundamental limit. One example is STED microscopy that focuses on the illumination, another near-field scanning microscopy that circumvents the diffraction limit by focusing on detection. Other methods and strategies in sub-wavelength imaging –negative refraction, time reversal imaging and on the case and absolute optical instruments –are concentrating on the faithful transfer of the optical information. In our opinion, the most significant, and naturally the most controversial, part of our findings in the course of this study was elucidating the role of detection. Maxwell's Fisheye transmits the optical information faithfully, but this is not enough. To have a faithful image, it is also necessary to extract the information at the destination. In our last two papers [3, 4], we report our new findings of the contribution of detection. We find out in the absolute optical instruments, such as the Maxwell Fisheye, embedded sources and detectors are not independent. They are mutually interacting, and this interaction influences the imaging property of the system.

## *Preface*

The purpose of the present research was to investigate an alternative method to circumventing the diffraction limit. The inspiration came from an old proposal of J. C. Maxwell on an unusual lens, called the Maxwell Fisheye, having an aberration-free image. Aberration-free imaging is considered as perfect imaging in geometrical optics approximation, where neglecting the wave nature of light results in the absence of diffraction effects. But, as soon as acknowledging light as an electromagnetic wave, the diffraction phenomena affect the outcome of the optical device. The problem that we aimed to solve was: under which circumstances an imaging device, which is aberration free in geometrical optics would also be diffraction-free in wave regime. The structure of the thesis is as following: **Chapter 1** is dedicated to introducing the classical concepts involved in the process of imaging. Different resolution criteria used in the literature have been introduced. Imaging in geometrical optics approximation has been compared with imaging in wave optics regime and various terms like the optical absolute instrument, the perfect imaging device, the point spread function, the Airy disc, etc., have been introduced. A historical review on the pioneering methods in super-resolved imaging follows, with a short discussion on each approach and method. The chapter ends with an argument about the diffraction limit: whether super-resolution is equal to breaking the diffraction limit and if any of the current super-resolved strategies overcome this fundamental limit.

**Chapter 2** includes some theoretical concepts that the candidate believes are necessary to mention, although they do not directly affect our arguments and calculations but lie underneath the methods that we are using. For example, inverse scattering methods are the core of our approach, even though we do not address them directly. The same applies to transformation optics and the optico-mechanical analogy.

In **Chapter 3** we introduce the Maxwell Fisheye (MFE). We provide a method to derive its index profile, study its geometrical symmetries and discuss practical options how to fabricate it. We end the chapter by giving a timeline on the study of Maxwell's Fisheye. In **Chapter 4**, we study the wave propagation in the Maxwell Fisheye medium. In this chapter, we implicitly use transformation optics and the optico-mechanical analogy to treat the MFE in two different ways: first, as an inhomogeneous medium and second, as the spherically curved vacuum. We provide an overview over the methods of electromagnetic calculations in stratified media and curved spaces.

**Chapter 5** is about the controversial experiments (we call them Singapore experiments), their demonstration, and the papers published in NJP in 2011 and 2012. We clearly express our critical opinion on the methods used in the experiment. The last section of

Chapter 5 discusses another experiment on the Maxwell Fisheye, Minaño *et al.*'s experiment. Both the Singapore experiment and the Minaño experiment focus on the detection of super-resolution in the Maxwell Fisheye. We discuss the different consequences and critical points. The latter experiment results in an unexplained observation, the so-called Minaño dips, which is a crucial phenomenon in interpreting the experimental results and provides a conclusion about the sub-wavelength focusing power of the MFE.

In **Chapter 6** we introduce a new model of interacting sources and drains which explains the above mentioned Minaño dips. We explain the role of the drain and the resolution. The implementation of a drain in the MFE — as a time-reversed source — plays a crucial role in our argument on the Fisheye imaging. A real (non-perfect) drain also plays a crucial role in understanding the Minaño dips. A comprehensive matrix model is developed to perform the calculations based on the Lagrangian model in the 1-dimensional Fisheye.

In **Chapter 7**, we extend our new model into two dimensions and numerically study different configurations of sources and drains. Our study clearly shows that the Maxwell Fisheye resolves a single source with precision much better than the diffraction limit, even if an array of detectors are detecting the image. However, for double sources or more, the internal interaction suppresses the sub-wavelength features.

Our **Final Word** discusses the concept of the Maxwell Fisheye as such and whether it is a perfect focusing device. By introducing a condition to overcome the refraction limit, we conclude that the Maxwell Fisheye, equipped with a drain, is a perfect focusing device for a single source which breaks the fundamental limit. However, it is not a perfect imaging device, because any perfect imaging device must be able to resolve two separate parts of the source located arbitrary close together, while the Fisheye fails to do this under the current circumstances.



# Contents

<b>Abstract</b>	<b>vi</b>
<b>Preface</b>	<b>ix</b>
<b>Contents</b>	<b>xi</b>
<b>List of Figures</b>	<b>xv</b>
<b>1 Introductory Chapter to the Problem</b>	<b>1</b>
1.1 An Introduction to Perfect Imaging . . . . .	1
1.2 General Features of an Optical Instrument . . . . .	3
1.3 Elements of Imaging . . . . .	3
1.3.1 Illumination . . . . .	4
1.3.2 Collection . . . . .	4
1.3.3 Detection . . . . .	5
1.4 Geometrical Optics vs Wave Optics . . . . .	5
1.4.1 Geometrical Optics Approximation . . . . .	5
1.5 Imaging in the Geometrical Optics regime . . . . .	6
1.5.1 Perfect Imaging in Geometrical Optics; Absolute Optical Instruments . . . . .	7
1.6 Imaging in the Wave regime . . . . .	8
1.6.1 Optical Resolution; Abbe Limit . . . . .	8
1.6.2 Resolution Criteria; Rayleigh, Sparrow, and other Formulas . . . . .	9
1.6.3 Kirchhoff Formula for Diffraction . . . . .	11
1.6.4 Point Spread Function and the Airy Disc . . . . .	13
1.6.5 Point Spread Function and the Extended Object . . . . .	14
1.6.6 Diffraction Limit and The Contribution of Higher Frequencies . . . . .	15
1.7 Eyes on Super-Resolution . . . . .	15
1.7.1 Functional Sub-wavelength Imaging . . . . .	17
1.7.2 True Sub-wavelength Imaging . . . . .	18
1.7.2.1 Near-field Scanning Optical Microscopy (NSOM) . . . . .	18
1.7.2.2 Negative Refractive Index Lenses and Super-Resolution . . . . .	18
1.7.2.3 Perfect Focusing and Time Reversal Imaging . . . . .	21
1.8 Does Super-Resolved Imaging techniques Breaks The Diffraction Limit? . . . . .	22
<b>2 Theoretical Background and Methods</b>	<b>23</b>

---

2.1	The Scattering Problem and the Fermat Principle . . . . .	23
2.1.1	General Introduction to the Inverse Scattering Problem . . . . .	23
2.1.2	The Fermat Principle . . . . .	25
2.1.3	Metrical Structure of the Medium and the Fermat Principle; Flat Space-Time . . . . .	26
2.2	Optico-Mechanical Analogy . . . . .	29
2.3	Brief Introduction to Transformation Optics . . . . .	30
2.3.1	Conventional Formulation . . . . .	31
2.3.2	Geometrical Formula; Special Transformation . . . . .	33
<b>3</b>	<b>The Maxwell Fisheye Medium</b>	<b>37</b>
3.1	The Maxwell Fisheye Medium . . . . .	37
3.2	Geometrical Properties of the Maxwell Fisheye . . . . .	39
3.3	Inverse Scattering Problem and Spherically Symmetric AI . . . . .	40
3.3.1	The Modified MFE . . . . .	44
3.4	Stereographic Map; Real Plane . . . . .	46
3.4.1	Stereographic Map; Complex Plane . . . . .	48
3.4.2	Few Practical Points on the Fabrication of the MFE . . . . .	50
3.4.3	Time Line in the Study of Optical Properties of the MFE . . . . .	51
<b>4</b>	<b>Electrodynamics of The Maxwell Fisheye Medium</b>	<b>53</b>
4.1	Introduction . . . . .	53
4.2	Electrodynamics of Inhomogeneous Media . . . . .	54
4.2.1	Inhomogeneous Media with Radial Symmetry . . . . .	56
4.2.2	Analysing the Debye potential in an N-Dimensional MFE . . . . .	60
4.2.2.1	The TE Mode in the Non-Magnetic Medium . . . . .	60
4.2.2.2	TM Mode in Non-Magnetic Medium . . . . .	62
4.2.2.3	Impedance-Matched MFE . . . . .	63
4.3	The MFE as a Curved Space . . . . .	64
4.4	An Alternative way to Derive EM Equation for MFE . . . . .	69
4.5	Geometrical Optics Exactness of MFE . . . . .	72
<b>5</b>	<b>Experimental Evidences: Imaging properties of absolute optical instruments</b>	<b>75</b>
5.1	About The Chapter . . . . .	75
5.2	Experimental Demonstrations . . . . .	75
5.3	Experimental Evidence I; Mirrored MFE, Ma <i>et al.</i> 's Setup . . . . .	76
5.3.1	Experimental Results; The Focusing of the Field With and Without Drain . . . . .	79
5.3.2	Resolution . . . . .	80
5.4	Experimental Evidences II; Modified Mirrored MFE, Ma <i>et al.</i> 's Setup . . . . .	83
5.4.1	Background . . . . .	83
5.4.2	Setup; Modified Mirrored MFE . . . . .	83
5.5	Experimental Evidence III; Imaging at Resonance Frequencies, Miñano <i>et al.</i> 's Experiment . . . . .	85
5.5.1	Comparison Between Two Experiments; MFE in Singapore vs. SWG in Madrid . . . . .	86
5.5.2	SWG, The Spherically Geodesic Waveguide . . . . .	86

5.5.3	Sub-wavelength Localization of The Field at Resonance Frequencies	87
5.5.4	Interpretation of the Dip in the Intensity Graphs . . . . .	89
5.5.5	Miñano's Model of Detection and Breaking the Diffraction Limit .	90
<b>6</b>	<b>The Spectrum of The Maxwell Fisheye Medium; One Dimensional Model</b>	<b>91</b>
6.1	Introduction . . . . .	91
6.2	Some Characteristic Features of MFE . . . . .	92
6.2.1	Resonance Frequencies . . . . .	92
6.2.2	1-Dimensional MFE; Differential Model . . . . .	95
6.2.3	Imperfect drain . . . . .	96
6.2.4	Mutual Relation Between Source and the Drain . . . . .	97
6.2.5	Field Solutions . . . . .	98
6.3	1-Dimensional MFE; Matrix Model . . . . .	100
6.3.1	Source and Drain as Coupling Vertices . . . . .	102
6.3.2	Sub-wavelength Focusing of The Field . . . . .	105
<b>7</b>	<b>The Interacting Sources and Directors; A Lagrangian Model</b>	<b>111</b>
7.1	Model . . . . .	111
7.1.1	Lagrangian . . . . .	111
7.1.2	Field Equations . . . . .	113
7.1.3	Consistency with Our One-Dimensional Model . . . . .	114
7.1.4	Green's Function . . . . .	114
7.2	Analysis . . . . .	116
7.2.1	Scattering Matrix . . . . .	116
7.2.2	Single Source, Single Drain . . . . .	118
7.2.3	Single Source, Multiple Drains . . . . .	120
7.2.4	Multiple Sources . . . . .	121
7.2.5	Antipodal Fields . . . . .	123
7.3	Final Words: Does the Maxwell Fisheye Break the Diffraction Limit? . .	124
<b>8</b>	<b>Conclusion Chapter</b>	<b>127</b>
8.1	Prospect and Conclusion . . . . .	127
<b>Bibliography</b>		<b>129</b>



# List of Figures

1.1	Resolution limit . . . . .	9
1.2	Diffraction patterns . . . . .	12
1.4	Pendry's Lens . . . . .	19
1.5	Negative refraction and folding of space . . . . .	19
1.6	The perfect lens . . . . .	20
2.1	Hebe Greek goddess of youth in a curved space . . . . .	30
3.1	Circular Trajectory Light on The Sphere . . . . .	40
3.2	Stereographic projection of circles . . . . .	40
3.3	Firsov inversion formula . . . . .	42
3.4	Luneburg's design problem . . . . .	43
3.5	Modified MFE mirror . . . . .	45
3.6	Index Profiles for Modified MFE mirror . . . . .	46
3.7	Stereographic map . . . . .	47
3.8	Stereographic map preserves the circles . . . . .	48
5.1	Focusing in curved space . . . . .	77
5.2	The Maxwell Fisheye device . . . . .	78
5.3	Field pattern . . . . .	79
5.4	Comparison with the theory for radiation without outlet I . . . . .	80
5.5	Comparison with the theory for radiation without outlet II . . . . .	81
5.6	Intensity distribution diagram for mirrored MFE . . . . .	82
5.7	Microwave image device for modified MFE . . . . .	84
5.8	Microwave image device for modified MFE . . . . .	85
5.9	Spherically geodesic waveguide experimental setup . . . . .	87
5.10	Spectrum of the intensity in SWG at antipodal point . . . . .	88
5.11	Spectrum of the Intensity in SWG at off position point . . . . .	89
6.1	Cross section of a $S^2$ with waves propagating on the surface . . . . .	93
6.2	Running fields on the surface of $S^2$ . . . . .	94
6.3	Running fields on the surface of a 1-D MFE . . . . .	94
6.4	A cross section of the MFE . . . . .	100
6.5	One-dimensional model of a perfect-imaging device . . . . .	101
6.6	Coupling vertex in one-dimensional Fisheye . . . . .	102
6.7	Transmission of EM fields through the lens . . . . .	107
7.1	Stereographic projection in one-dimension . . . . .	112
7.2	Absolute optical instrument with mutually interacting sources and drains	116

7.3	Single source, single drain; schematic picture of Miñano's experiment . . . . .	118
7.4	Transmission of a single source through the MFE to a single drain . . . . .	119
7.5	Transmission of a single source to two drains . . . . .	122
7.6	Multiple sources, array of drains . . . . .	123
7.7	Two sources and two drains . . . . .	124

# Chapter 1

## Introductory Chapter to the Problem

### 1.1 An Introduction to Perfect Imaging

Perfect imaging is a broad term in optical science for the challenge of making the ultimate imaging device[9–11]. However, the concept of “ultimate image” is subject to interpretation and depend on context. For example, though it has a well-defined meaning in geometrical optics, the definition of perfect imaging is more ambiguous in the wave regime because, given the wave nature of light, the quality of the image is limited by the diffractive nature of light. Perfect optical imaging system, in addition to providing the aberration-free final image, must provide unlimited resolution. Ever-increasing attempts in the last few decades have resulted in the development of many methods and strategies for super-resolution. A super-resolution device is not necessarily a perfect imaging system but rather one that resolves the image beyond the resolution limit. The resolution limit first formulated by Ernst Abbe in the study of the theory of microscopes [9, 10, 12].

$$\text{Abbe's Resolution} = \frac{\lambda}{2\mathcal{N}A}. \quad (1.1)$$

Here,  $\lambda$  is the wavelength of the light and  $\mathcal{N}A$ , the numerical aperture, is the characteristic number of the lens and depends on  $n$  the refractive index of the medium. Abbe’s formula later generalized for all types of optical instruments, became known as the fundamental limit, as it is independent of manufacturing defects or the precision of the device. Since the nineteenth century, up to the year of this dissertation, achieving an optical resolution higher than Abbe’s classical bound ( 200nm in the mid-visual range) was in high demand in both science and industry. In recent decades, super-resolved imaging has become even more crucial because the scale of human control over

the construction and manipulation of materials has been approaching the nano regime in science and technology. In bioscience, developments in medicine strongly depend on nanoscopic techniques. To have a quantitative picture, the maximum resolution for modern optical lenses with the high numerical aperture  $NA$  is limited to 150-200 nm in mid-range of visible light. Such a limit sharply restricts access to sub-nano structures smaller than 150 nm. Therefore, fields like biology, nano-science and nano-engineering, where working with nano-sized objects in the range of visible light is crucial, suffer from this restriction. Today, many advanced devices like electron microscopes or near field imaging microscopy techniques are available, but this fact did not reduce the needs for the hight resolution optical microscopy. The revolutionary influence of access to super-resolution in these areas resulted in awarding of the Nobel Prize in chemistry for the development of the illuminated fluorescent nanoscopy [13, 14].

The resolution problem might be reduced to the fact that optical instruments with coherent illumination cannot resolve the object better than 150-200 nm (Abbe's limit): then the phenomenological solution would simply be challenge to push the limit below the 150-200 nm. Despite this practical achievement to reach the sub-wavelength image (around 40 nm) by fluorescent microscope, the hard core of the problem to achieving the optimal perfect imaging or beating the diffraction limit yet remains in front. One can argue whether the fact of having resolution better than 200-150 nm is necessarily breaking the diffraction limit. The situation resembles the quantum uncertainty relation among conjugate variables: achieving the quantum squeezed state with high resolution in only a single variable does not violate the uncertainty principle. The enormous amount of literature on the topic gives the sense of a lack of comprehensive, fundamental approach to the core problem. Varying interpretations of super-resolution or diffraction limit and varying interpretations of superseding the Abbe's limit, make it hard to categorise and evaluate the efficiency of the different approaches. From the theoretical point of view, there is sufficient evidence to consider the resolution limit as a fundamental restriction of nature (similar to the uncertainty principle of quantum theory). Therefore, any study regarding the violation of this fundamental limit, should discuss the set of conditions that would define a meaningful resolution limit in a rigorous framework and any possible loopholes in the suggested method of exceeding it.

In recent studies, the term “super-resolution” is more often used as a phenomenological attribute rather than a theoretical prediction. Consequently, the lack of rigorous theoretical background relevant to resolution limit in classical terms results in controversy when experimental and phenomenological evidence are the only means of supporting the claims: without a theoretical framework, one might not be able adequately criticise efficiently one method or to describe the failure of another approach. In this chapter, we give a brief, historical overview of the optical resolution problem. First, we are reviewing the elements and parameters of classical optics which are essential for formation

of an image. We will argue why a diffraction limit might be a fundamental feature of optics, and if so, which techniques were successful in circumventing that limit. Later, we describe the relation between overcoming the diffraction limit and super resolution.

## 1.2 General Features of an Optical Instrument

In the context of this thesis, an optical instruments, is a device for enhancing or registering an image of an object to aid vision. The register of the image involves processing light waves. We can describe this processing by the behaviour of electromagnetic waves, or when possible, simply in the geometrical optics approximation. Image quality literally means the faithfulness of the device in transmitting the details of the object through the enhancement process. The instruments in an imaging device include a combination of lenses, apertures, light collectors, reflectors, and detectors. However, in this chapter we do not deal with the complicated details of these elements but rather abstractly reducing them to aperture. The imaging process has three main stages: illuminating the object; collecting the light; and detecting the light. The quality of the image depends on all of the above. Enormous amount of studies in the nineteen century on the construction of microscopes and telescopes revealed that all defects in the formation of a faithful image could, in principle, be remedied by honing the lenses to perfection except one: the resolution. Optical defects like coma, defocus, distortion, astigmatism etc. in instruments are due to optical aberration (the departure from the paraxial approximation), which requires correction to the wave front of light. Aberration theory provides methods for visualising the effects of aberration and correcting them. However, Ernst Abbe showed that there is maximum spatial resolution which is independent of the perfection of the instrument because it is due to the intrinsic nature of light.

## 1.3 Elements of Imaging

The image of an object can be defined as a graphic representation of the spatial distribution of one or more of the object's properties. The object might be a luminal emitter like an antenna, or a scatterer. The image of an object is formed when the emitted/scattered light from the object, which carries the information, comes together. The interaction of light (with proper frequency in the spectrum of the electromagnetic field) with the object is a necessary condition. In ray optics, there is no restriction on the probing/emitting light. The plane which includes the position of the object calls the "object plane" or the "object space" and the location of the image place at the "image plane" or the "image space". Any effort toward super-resolution imaging can apply to any of main imaging stages: illumination; collection of the scattered/emitted light; procession of light inside the optical device; and detection at the detector. Resolution

criteria only reflect the sum impact of all of these stages on the final output. However, it is crucial to distinguish the independent contribution of each of these steps in resolution of the image when comparing different strategies for achieving super-resolution.

### 1.3.1 Illumination

In image processing, the wave nature of light requires that the target object interacts with the light of a wavelength comparable to, or smaller than the object itself [7]. According to the Abbe's theory, the fidelity of the image is determined by the proper ratio between the size of the object and the wavelength. This definition is compatible with the theory of diffraction. The final diffraction pattern of the scattered light from an obstacle or a slit projects the properties of the slit or obstacle. The wavelength of the illuminating light must be of the order of the size of the object or the field will miss the object. In the case of the slit, the light cannot pass through if its wavelength is too large. Illumination becomes more important when the object is nonluminous or has an extended area. For an extended object the image is a complicated (practically infinite) overlapping of single diffracted patterns with slightly different frequencies and strengths from different points of a specimen. Manipulating the illumination process might have a significant effect on the resolution. For example, illuminating the object by evanescent waves leads into a situation that high spatial Fourier components of the object can appear in the image, and therefore increases the resolution of the system, even if those components were hight to pass through the device. Beside the key role of wavelength in the resolution of the image, the coherency of illuminating light and the method of illumination can also affect imaging quality. The effect of light coherency on resolution has not considered in this research project. However, it might be an interesting parameter for future study.

### 1.3.2 Collection

Collection of the scattered light has a direct relation to the quality and the resolution of the image. The more information from an object, the better the image an optical device can construct from it. This fact expressed in Abbe's formula: A larger aperture or higher numerical aperture  $\mathcal{N}A$  results in higher resolution. There is a limit to the scattered or emitted light from an object that is gathered by a conventional lens. According to Abbe's formula, even an infinitely large aperture can collect only half of the radiation comes from an object. However, the new  $4\pi$  microscope utilizes advanced collecting construction to gather significantly more scattered light. Later we will use this parameter to argue for spherically symmetric lenses.

### 1.3.3 Detection

Detection is probably the most sophisticated part of imaging. In classical optical devices, we speak of the image plane, the real or virtual surface upon which rays of light intersect and form the image. Reflection from the image plane is transmitted into the eyes of the observer. So in conventional optical devices like microscopes, or telescopes, or cameras the detector is simply the human eye or a photographic plate. Modern optical science utilizes photons in detectors like CCD cameras in which, image formation does not require the direct reflection from a surface into our eyes, but rather goes through a more complicated process. Within this context one can argue about the quality or resolution of the detectors and their influence on the diffraction limit. Thus, in some modern imaging devices the resolution limit depends on the resolution of the detector as well as wavelength and numerical aperture.

## 1.4 Geometrical Optics vs Wave Optics

In this section, we compare imaging in geometrical optics regime with imaging in wave optics. In particular, the definition of perfection in the two regimes is very different. In geometrical optics, the “perfect” image is one perfectly focused and free from aberration: diffraction is not taken into account. But in wave optics resolution is the key feature of perfect imaging. The subject of present study is the relations between the two phenomena and the conditions under which they coincide: when a perfect imaging in geometrical optics means a perfect imaging in wave regime. First, we see the definition of the geometrical optics approximation.

### 1.4.1 Geometrical Optics Approximation

In the high frequency approximation, Maxwell’s theory of electrodynamics reduces to geometrical optics in the zeroth-order approximation, while certain features of wave phenomena, like polarisation and wavefront solutions, remain as the first-order approximation.

Diffraction limit is the consequence of the wave nature of light: it therefore vanishes naturally in the geometrical optics, GO, approximation. GO theory divides the propagation into two independent parameters: trajectories or rays, which mathematically are equivalent to geodesics of space and wave fronts which specify in space by Eikonal equations. However, in the full wave regime, exact wave fronts can differ dramatically from their zeroth-order GO approximations. Therefore, it is critical to know the conditions which lead to the exact wavefront solution and to clarify which optical properties of the solutions are shared between exact solutions and GO approximations (zeroth-order) and

which characteristics vanish at the GO's breakdown. First consider a monochromatic scalar Helmholtz equation in an inhomogeneous medium:

$$\nabla^2 \psi_\omega(\mathbf{r}) + \frac{\omega^2}{c} n^2(\mathbf{r}, \omega) \psi_\omega(\mathbf{r}) = 0 \quad (1.2)$$

At the high frequencies, the Helmholtz equation can be interpreted as time-independent Schrödinger equation. In such a limit, a quantum de Borghlie particle with particle-wave features and a classical EM wave with wave-particle (photon) duality are on the same footing. The wave properties of a quantum point particle and the particle features of classical wave optics here coincide. However, geometric optical trajectories are not the paths that photons follow; similarly, classical trajectories are not the paths followed by quantum particles. So, the difference between wave optics and GO geodesic paths is the same as the difference between the quantum and classical motions of a single particle. It is easy to see these features in the Helmholtz equation if we separate it properly. As the solutions are complex, we can separate the amplitude from the phase in the familiar form of:

$$\psi_\omega(\mathbf{r}) = R(\mathbf{r}) e^{iS(\mathbf{r})} \quad (1.3)$$

By substituting Equation 1.3 into Equation 1.2, we can separate the later into:

$$\nabla^2 S(\mathbf{r}) + \frac{\nabla^2 R(\mathbf{r})}{R(\mathbf{r})} + \frac{\omega^2}{c} n^2(\mathbf{r}, \omega) = 0 \quad (1.4)$$

$$\nabla \cdot (R^2(\mathbf{r}) \nabla S(\mathbf{r})) = 0 \quad (1.5)$$

Geometrical optics is valid if and only if the second term in Equation 1.4—called the quantum potential—vanishes from the Helmholtz-Schrödinger equations [15]. If the term,

$$\frac{\nabla^2 R(\mathbf{r})}{R(\mathbf{r})},$$

becomes negligible, we have the GO approximation. If under particular circumstances  $\nabla^2 R(\mathbf{r})$  becomes exactly zero, the GO solutions are exact.

## 1.5 Imaging in the Geometrical Optics regime

In the geometrical optics approximation, scattered light rays from an object diverge spatially. By collecting the rays and reversing their divergence to convergence (or sometimes vice versa), we may visually reconstruct the object. This process is called imaging.

Gathering and appropriately reversing the rays, divergence is done by an optical device. If an optical device is sufficiently good to collect all possible rays emitted or scattered from a point object  $P$  in manner that all of those rays converge at another point  $P'$ , then the corresponding constructed image would be termed a strongly sharp image [7]. In geometry such points are called perfect conjugate points.

**Definition 1.1.** Two points  $P$  and  $P'$  on the Riemannian manifold  $\mathcal{M}$  are a conjugate pair if they are connected by a 1-parameter family of geodesics. The prolate ellipsoidal reflector <sup>1</sup> is an example of an optical device with one pair of perfect conjugate points that coincide with its focal points. Apart from the ellipsoid reflector and the flat mirror (the latter is a very exceptional case), it is not trivial to obtain a sharp image. A theorem of differential geometry states that in the Euclidian space, there are no conjugate points. Therefore, obtaining a sharp image in Euclidian space using conventional optical devices geometrically is not likely. However, certain designs result in optical devices that confine light rays in a medium which implements a non-Euclidian manifold with conjugate pairs. Absolute optical instruments are examples of these [16, 17].

### 1.5.1 Perfect Imaging in Geometrical Optics; Absolute Optical Instruments

The concept of perfect imaging first appeared in geometrical optics where the limitations of optical instruments are less than in the wave regime. In GO, the diffraction limit of resolution is not a factor, but instead one needs only eliminate the optical aberrations of the device. Remarkably, there exist devices in which optical aberration can be totally eliminated: they are called absolute instruments [7, 17]. In geometrical optics there is a set of established conditions under which an optical device can minimize or even eliminate optical aberrations. Within geometrical optics, the resultant images of such a device are called perfect [7]. As stated in [17] “the meaning of ‘perfect imaging’ is different in geometrical and in wave optics. In particular, an imaging device that is perfect from the point of view of geometrical optics may or may not be perfect from the point of view of wave optics and vice versa .” This is simply due to the difference between the nature of geometrical optics and wave optics. Absolute Instruments are optical devices which make strongly sharp, full image from any point of object domain. An object domain needs to be a non-zero volume in 3-dimensional space to fit the criteria for the device. Tyc. et.al defined the strongly sharp image as following [17]:

**Definition 1.2.** A strong, sharp image of a point  $x_1$  is the point  $x_2$  if an infinity of rays emerging from  $x_1$  meet again at  $x_2$  through a nonzero solid angle.

---

<sup>1</sup>A prolate spheroid is a surface of revolution obtained by rotating an ellipse about its major axis (Hilbert and Cohn-Vossen 1999, p. 10). A symmetrical egg (i.e., with the same shape at both ends) would be a good approximation of a prolate spheroid

If an infinity of rays emerge from  $x_1$  meet at  $x_2$  through a zero solid angle, the image is said to be weakly sharp.

**Definition 1.3.** If an infinity of all the rays emerging from  $x_1$  meet at  $x_2$ , the image at  $x_2$  is full, otherwise it is partial image.

If an optical device produces a strongly sharp image, it is called an optical absolute instrument (AI). If an optical device produces a sharp image not just for a single point but for all points in an object domain, it is called an optical absolute instrument of the first kind.

## 1.6 Imaging in the Wave regime

In wave optics, perfect imaging is connected to resolution. Super-resolution is obtaining an image of higher resolution than Abbe's limit. While, perfect imaging is an ultimate case: the unlimited resolution, which is not restricted by the wavelength of light. Before attempting to construct a perfect imaging device, one must clarify the definition of the perfect image in wave optics and the parameters involved in the process.

### 1.6.1 Optical Resolution; Abbe Limit

In the broadest sense spatial resolution might be defined as the smallest feature that can be identified from an optical system's output. One of the earliest works that formed our perception of optical resolution emerged from intensive research on the development of microscopes in 1870ies [9, 10, 12, 18]. Ernst Abbe's famous discovery in 1873 turned into a paradigm in optics, wherein the resolution and fidelity of an optical image produced by an optical instrument is determined by two parameters: the properties of the optical device and the natural characteristic (wavelength) of the illuminating or detected light [7]. Remember from the introduction:

$$\text{Abbe's Resolution} = \frac{\lambda}{2\mathcal{N}A} = \frac{\lambda}{2n \sin \theta}. \quad (1.6)$$

where  $\mathcal{N}A = n \sin \theta$ , the numerical aperture, is the characteristic number of the lens and depends on  $n$  the refractive index of the medium, and an  $\theta$ , the maximum angle that the lens can collect the light from the object. Ignoring optical aberrations due to the manufacturing quality of the device, the formula indicates that even given the largest aperture number  $\mathcal{N}A$  available [19], the ultimate limitation bound to the wavelength of light, prevent us from unlimited resolution. No detailed structures smaller than about half the wavelength appears in the image. Though, Abbe derived the formula for a particular type of microscope with multiple complicated lenses the maximum resolution applies to all types of optical instruments.

### 1.6.2 Resolution Criteria; Rayleigh, Sparrow, and other Formulas

In 1896 Lord J. Rayleigh [20] refined Abbe's formula and introduced a physical picture based on diffraction, today called the Rayleigh criterion. It probably is the most widely used measure of resolution.

$$\text{Rayleigh Resolution} = \frac{0.61\lambda}{NA}. \quad (1.7)$$

According to the Rayleigh criterion, the optical resolution of a device is defined as the distance between the closest neighbouring points where the image of principal diffraction maximum of one point overlaps the first minimum of the others, as shown in Figure 1.1. Rayleigh's model explained the physics beneath the fundamental limit of the resolution, which is the universal law of diffraction intrinsic to periodical fields, including electromagnetic. Rayleigh's description of resolution leads to the definition of the point spread function (PSF) of the optical system as a measure of imaging resolution.

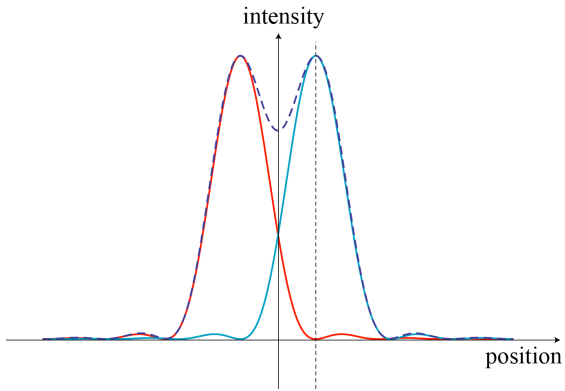


FIGURE 1.1: Maximum resolution is defined by the overlap of the two picks, when the first maximum of one point is located on the first minimum of the other.

Radiation from any single point source that passes through an aperture onto an imaging surface, experiences diffraction process and interference, recombining to form a pattern on the imaging surface. The result is an array of constructive (bright) and destructive (dark) regions with a bright intensive maximum in the centre. The width of this maximum, is a measure of the deterioration from the original point source. In the case of circular lenses, the width of this area is called the diameter of the Airy disc and, without losing generality, we will use it in what follows.

Any image from an extended object is composed of a collection of overlapping diffraction-limited spots.[7]. Any two arbitrary points of an extended object can be readily distinguished if their separation is larger than the resolution of the lens.

As we will see, the Rayleigh criterion is not an adequate measure of resolution because it does not take in to account the role of evanescent fields in image formation. Accordingly, one can argue if the Rayleigh's resolution truly indicates a fundamental limit. For

example in experimental astronomy it is possible to resolve the two stars even when they are closer than Rayleigh's limit.

After Rayleigh, other people refined the resolution limit even more. C. M. Sparrow, in 1916 during the course of photographic experiments with simulated spectroscopic lines, recognized a different upper bound on the resolution which is about 20% smaller than the Rayleigh limit. Sparrow's resolution limit is met when the combined light from two overlapping and equally bright Airy disks is constant along a line between the central peak brightnesses. During the twentieth century, various physical origins were proposed to describe resolution limit, resulting in diverse sorts of technology to solve the resolution problem. For example, the discovery of the role of the near-field components in the image as a source of diffraction limit resulted in near-field microscopy and negative refractive index lenses. Rayleigh's criteria for resolution, based on Fraunhofer diffraction is not able to describe the near-field contribution to a detailed sub-wavelength image. Another strategy recently used to exceeding the Abbe limit is based on the techniques to localised the light waves beyond the limit that Rayleigh criteria is allowed. Another approach argues that the diffraction limit has its roots in the lower bound on the size of the illuminated object. There is a limitation on the focusing of light, which is also proportional to the scale of the wavelength. Time reversal imaging, absolute optical instruments and tied focused light method, all attempt to overcome the imperfect focusing problem. As we can see a different interpretations of resolution limits and its underlying causes, results in various techniques for overcome the limit.

Moreover, recently it has been found that the Rayleigh limit has a meaningful relation to other estimates of signal resolution, including the Shannon sampling rate, which is fundamental for representing band-limited signals. Perhaps this is the root for the assumption that the Rayleigh limit is a fundamental concept of physics, though this question is beyond the scope of the present thesis [21]. In short, the parameters which affect the image resolution of an optical device are:

- The fraction of the field that enters the device from the luminal or scatterer source, which depends on the numerical aperture.
- The wavelength of the emitted light.
- The focusing factor of the device. Appears partially in the aperture number.
- The phase relation of the focusing fields which construct the image. Appears partially in the aperture number
- Near field components. Does not appear in Abbe-type formula

### 1.6.3 Kirchhoff Formula for Diffraction

According to Rayleigh's interpretation, the resolution limit is a consequence of diffraction in the optical system. Before discussing the more quantitative measure called the two point spread function, we will briefly examine the definition of the diffraction which caused the fundamental defect in the performance of an optical instrument. Diffraction is a phenomena observable in all physical systems which possess wave behaviour, including sound waves, electromagnetic fields and matter waves. The Huygens model of wave propagation provided for the first time a qualitative understanding of diffraction based on the concepts of secondary sources and the envelope of secondary wavelets <sup>2</sup>.

Diffraction is created when the path of light bend at any sharp obstacle. In the Huygens picture of wave propagation, a wave front in a particular locus of space is an envelope over infinite secondary wavelets. The mechanism of wave bending or diffraction is due to the partial elimination of secondary sources. Figure 1.2 shows the diffraction pattern of a plane wave from a simple aperture. An aperture passes only the finite part of the wavefront, eliminating the rest. Elimination of the in-phase secondary sources distorts the shape of the plane wave, bending the direction of wave propagation, and changing the phase relation between the secondary sources on the particular locus. Consequently, after passing through the aperture plane wave decomposes into several new enveloped wavefronts which interfere with each other and form the dark and bright patterns. All of the above-mentioned processes are most pronounced when the size of the aperture is comparable to the wavelength of the light. That is why diffraction has been assumed to be a wave phenomenon. In the geometrical optics regime, the effects are negligible. In the context of our discussion, perfect imaging has a clear meaning and even is achievable in the GO approximation but not in the wave regime.

So far we have presented only the most simple qualitative description of what happens when light enters the aperture of an optical device. In reality, the process is much more complicated, though even in this basic picture you can see how the original field distribution might be deformed through the most unsophisticated optical process. And the diffraction pattern calculations are complicated, requiring computers and numerical methods, based on the Kirchhoff diffraction theory. The simplest form of the theory is shown in Figure 1.3, where we are illustrate the Helmholtz-Kirchhoff scalar theory for a monochromatic point source. We do not aim to go into detail of diffraction theory. However, just the schematic form of the theory can reveal the parameters which have influence on the final outcome of an optical aperture including an imaging system. The point source  $P_0$  emits the monochromatic light Figure 1.3. The space is assumed to be isotropic, homogenous, nonmagnetic, and linear.  $S_1$  is an finite aperture, with a normal

---

<sup>2</sup> Each point on the wavefront of disturbance is considered a new source of a secondary spherical disturbance. The wavefront at later instants can be found by constructing the envelope of the secondary wavelet. For more details of Huygens theory see [7]

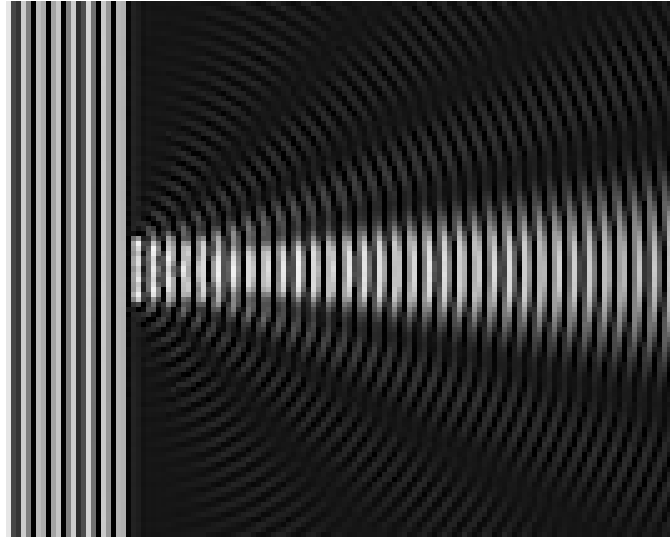


FIGURE 1.2: In the figure we can see the formation of constructive and destructive wave components results in diffraction pattern for waves. Before the aperture plane waves propagate parallel and in phase. Aperture just collects fraction of the waves which reforms the phase relation of the wave fronts.(Source: Internet)

vector  $\mathbf{n}$  dividing the space into two regions  $R_s$  the source space in front of aperture, and  $R_i$ , the image space behind the aperture.

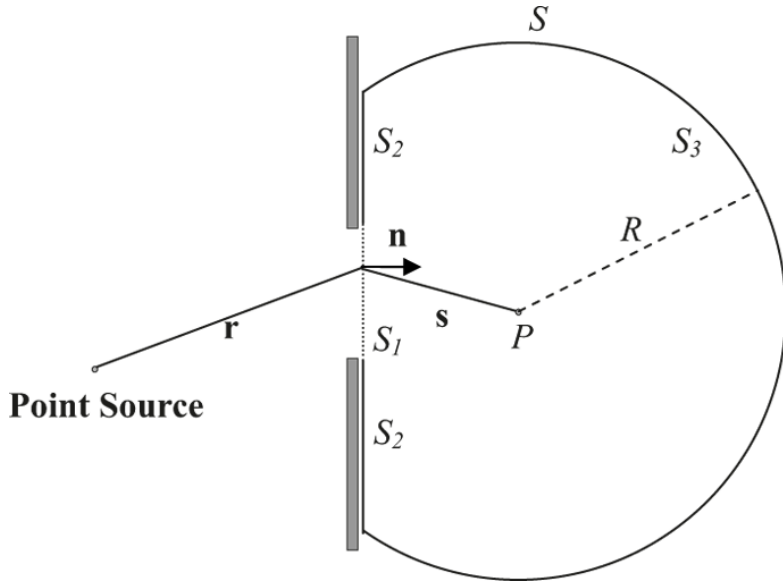


FIGURE 1.3

Our aim is to calculate the field distribution at point  $P$  in the image space where the distance of  $P$  from the aperture  $S_1$  is much larger than the wavelength: that is  $s \gg \lambda$  (the Kirchhoff condition).  $S = S_1 + S_2 + S_3$  is an arbitrary closed boundary which includes the aperture. Based on Green's theorem, Kirchhoff derived the following integral, which gives the field at the point  $P$ :

$$U(P) = \frac{1}{4\pi} \iint_S (G \frac{\partial U}{\partial n} - U \frac{\partial G}{\partial n}) ds \quad S = S_1 + S_2 + S_3 \quad (1.8)$$

In formula 1.8,  $G$  is the propagation or Green's function for the system and  $U$  inside the integral is the solution for the field at the boundaries.  $U(P)$ , the field at point  $P$  is expressed in terms of the boundary values of the wave on any closed surface surrounding that point. It is obvious that the integral would have a meaningful value only if we put reasonable conditions on the boundary values. The Kirchhoff conditions are a set of boundary conditions which assume that the field goes to the zero on all the boundaries except the aperture  $\{U(x) = 0 \forall x | x \in S_2 + S_3\}$ . The function  $U(P)$  is the field distribution in the image space. We can see the direct dependency of the final field distribution on the Green's function. By changing the Green's function, we can control the diffraction. For the same initial fields (source) and initial boundary conditions, a different propagating function results in the different degrees of diffraction. So parameters which influence Green's function –boundary conditions and geometry of the propagating space – control the diffraction process. Later, when we discuss a specific optical device, called the Maxwell Fisheye, we will see that a particular forms of Green's function can change the diffraction limit for a single point source.

#### 1.6.4 Point Spread Function and the Airy Disc

What we have seen in the previous part was the mechanism for calculating the diffraction pattern of a single point source under Kirchhoff boundary conditions. We can extend this mechanism to the much more complicated optical systems with multiple lenses, apertures, etc., and an extended object, though the computation is not trivial and in most cases not even analytic, often requiring computer softwares. The result of Equation 1.8 for a single point source is called the point spread function (PSF) of the optical system. PSF is the image that an optical system gives from an ideal luminous point object. Some literature calls the ideal luminous point object the “impulse function” and denotes the PSF as the “impulse response” of the system. Mathematically, the impulse function is a delta function  $\delta(x_0, y_0)$ . The PSF expresses the degree of spreading (blurring) of the point object and traditionally is the characteristic of an optical system’s quality of the image. In conventional optics, diffraction limit implies that no optical system can image a point source (delta function) into a point source (delta function). The PSF of an optical system is never a delta function. An aberration-free imaging device with the best-focused spot (called perfect imaging in ray optics) has the minimum PSF. George Biddell Airy in 1835 calculated the most compact PSF, which is called after him the Airy disc. He used a uniformly-illuminated pinhole with a circular aperture as an aberration-free optical model. The resulting diffraction pattern has a bright region in the centre with the surrounding series of concentric bright rings. Similar to the Abbe’s

limit, the radius of the Airy disc is proportion to wavelength and the inverse of the diameter of aperture. The approximated form of the Airy formula when the aperture is far from the image becomes:

$$\theta = 1.22 \frac{\lambda}{d} \quad (1.9)$$

where  $\theta$  is the angle at which the first minimum occurs. In this point, we define a criterion for a perfect focusing system in the electromagnetic regime as follows:

*An optical device violates the diffraction limit if and only if its point spread function (PSF) is smaller than its own Airy disc.*

### 1.6.5 Point Spread Function and the Extended Object

As we have mentioned, the Kirchhoff diffraction theory assumes the linearity of the optical system. Therefore imaging by a microscope or telescope follows the superposition principle:

$$\text{Image}(\text{Object}_1 + \text{Object}_2) = \text{Image}(\text{Object}_1) + \text{Image}(\text{Object}_2)$$

Any object can be thought of as consisting of many points (in the limit, infinitely many), each with its strength in linear optical systems (called linear shift invariant), such that by using non-coherent illumination, the image can be described as a sum of corresponding individual PSFs. Mathematically speaking, a linear system can be idealised as utilising the position-independency of SPF. Therefore, the final image can be considered as a convolution of a perfect image with the point spread function. Mathematically, an extended object might be represented as following:

$$U(x_0, y_0) = \iint U(m, n) \delta(m - x_0, n - y_0) dm dn \quad (1.10)$$

i.e., a sum over weighted impulse functions.  $U(m, n)$  is a weight function describing the geometrical features of the specimen. Rewriting the object transmittance function in the form above allows us to calculate the image field as the superposition of the images of each of the individual impulse functions, i.e., as a superposition over weighted point spread functions in the image plane using the same weighting function as in the object plane,  $U(x_0, y_0)$ . Mathematically, the image is expressed as:

$$I(x_i, y_i) = \iint U(m, n) K(m - x_i/M, n - y_i/M) du dv \quad (1.11)$$

in which  $K(m - x_i/M, n - y_i/M)$  is the image of the impulse function  $\delta(m - x_0, n - y_0)$  or PSF of the system.

However, there is no ideal luminous point source. Any form of the source has some extended structure. Therefore, the above picture is not entirely exact when we are dealing with precise measurements.

### 1.6.6 Diffraction Limit and The Contribution of Higher Frequencies

As we discussed earlier in this chapter, it is believed that the Rayleigh criteria for resolution are not completely describing the resolution of an optical device. Thus, resolution flaw is not only the results of interferences of the waves in different phases but also partly due to the lack of information carried out by the decay of near field of the emitter. To see it clearer, consider a field emitting from an object, written as a superposition of plane waves: The direction of propagation is the  $z$ -axis:

$$E(x, y, z, t) = \sum_{k_x, k_y} A(k_x, k_y) e^{i(k_z z + k_y y + k_x x - \omega t)} \quad (1.12)$$

where  $k_z$  is a function of  $k_x$  and  $k_y$  as:

$$k_z = \sqrt{\frac{\omega^2}{c^2} - (k_x^2 + k_y^2)} \quad (1.13)$$

Only the positive square root is taken because the energy is in the  $+z$  direction. All of the components of the angular spectrum of the image for which  $k_z$  is real are transmitted and re-focused by an ordinary lens. However, if

$$k_x^2 + k_y^2 > \frac{\omega^2}{c^2}, \quad (1.14)$$

then  $k_z$  becomes imaginary and the wave is an evanescent wave the amplitude of which decays as the wave propagates along the  $z$ -axis. This results in the loss of the high angular frequency components of the wave, which contain information about the high frequency (small scale) feature of the object being imaged. The highest resolution that can be obtained can be expressed in terms of the wavelength:

$$k_{max} \approx \frac{\omega}{c} = \frac{2\pi}{\lambda} \cdot \Delta x_{min} \approx \lambda \quad (1.15)$$

## 1.7 Eyes on Super-Resolution

<sup>3</sup> We have already introduced the relevant features of imaging in the wave regime such as diffraction, resolution, and the parameters influencing the quality of the image. In this section we briefly review some of the approaches and techniques used to achieve super-resolution. Our list of such approaches and techniques is not complete, and scientific efforts toward super-resolution is much beyond that. In the nineteenth and early twentieth centuries, when diffraction phenomena were at the peak of optics studies, the visible range of the spectrum was the only available technique for imaging thus, resolution criteria were established regardfully. However, today we are facing the diverse

---

<sup>3</sup>The title is taken from an interview with W. E. Moerner on the topic, which appeared in Nature Photonics 3, 368 - 369 (2009)

fields of imaging systems ranging from MRI to electron microscopy. In this review, we consider only optical or EM imaging. During the past few decades, many new techniques have been invented and theoretical works developed to push imaging resolution beyond the diffraction limit. Today, the methods used in modern microscopes already give resolutions better than Abbe's limit (that is, better than 200 nm in the optical range); but of course there are some trade-offs and under costly circumstances. Each of the methods has its own set of advantages and disadvantages, and in most cases the advantages demand significant compromises. For example, the near field method is restricted to surface objects and short distances (roughly about 10 nm) due to the collection of evanescent signals from the object. Another example are far-field techniques like STED and SIM, which do not restrict the user to short scales, but impose a lot of requirements on the optical properties of the specimen. All methods based on fluorescent microscopy need to attach the fluorescent substances to the specimen. Moreover, from a fundamental point of view, it is not trivial to assume that any super-resolution method is actually violating the diffraction limit. For example, in fluorescence microscopy, spatial Fourier components of the fluorescence intensity with a period less than  $\lambda/2$  cannot be imaged, even if it is possible to resolve much finer Fourier components in the object itself. [19, 22].

To categorize different strategies, A. Neice in his review article [23] used the terms “*true subwavelength imaging*” and “*functional sub-wavelength imaging*”. Here, we would like to adopt his definitions. “True sub-wavelength imaging” means the sub-wavelength system should be able to:

“(1) Image an unrestricted variety of images. (2) Use transmitted, reflected, or emitted radiation.”

and,

“If arbitrary restrictions must be added to the sub-wavelength system to accurately reconstruct images, then it would be more accurately described as a functional system.”

Accordingly, Neice suggested the following rules for a true sub-wavelength system [23]:

1. “The image is created based on waves or fields, EM or otherwise, that are produced, reflected, refracted, absorbed, or otherwise transmitted by the plane being imaged, and the detection and imaging system is agnostic as to the specific interaction with the radiation. In particular, it is not reliant on any particular nonlinear optical effects.
2. The distribution of matter within the imaged plane can be any arbitrary distribution and still allow imaging.
3. The fields or waves described in rule (1) are the only means of interaction between the imaging device and the sample. . .

Imaging that is otherwise sub-wavelength but violates one of these rules is considered functional sub-wavelength imaging.”

The majority of super-resolved imaging techniques, according to these conditions, are functional. These include: MRI, photoactivated localization microscopy, stimulated emission depletion microscopy, structured illumination microscopy, and reversible saturable optical fluorescence transitions (RESOLFT) microscopy. Also strategies that involve nonlinearities in the behaviour of the fluorescent proteins, such as photo-bleaching and saturation, violate rule (1) can not fit into the definition of true sub-wavelength imaging[23].

Therefore, very few imaging techniques can be regarded as true sub-wavelength imaging according to Niece rules: these includes Pendry-type super-lens (negative refractive index lens), optical AI (the subject of our research), near-field microscopy, and time-reversal imaging. This shows the importance of the current thesis.

In early 2000, interest in the topic resurged with the proposal of negative refractive index lenses by John Pendry [24, 25]. The new wave was about the theoretical possibility of the perfect imaging rather than only phenomenological achievements. Pendry’s proposal was based on earlier theoretical papers by Veselago [26], which followed by other interesting candidates like time-reversal imaging methods [27], polarisation perfect focusing [28], superscillation lenses [29], etc. However, theoretical proposals also encounter sort of limitations or practical barriers. In short, despite the theoretical and practical advances in true sub-wavelength imaging, the fundamental limit of nature does not wholly go away, but rather reappears in different expressions. In the philosophy of science, such a situation is called loophole in the theory. We can practically get better resolution than diffraction limit but only through loopholes. The main aim of our research is to study and analyse a proposal for the direct true sub-wavelength imaging with unlimited resolution and consider possible loopholes. Referring to all methods in nanoscopy needs a separate document and it is beyond the scope of this thesis, but before going further we will mention few methods that we already named in this introduction.

### 1.7.1 Functional Sub-wavelength Imaging

Sub-diffraction imaging methods like STED, SMI, and SIM employed modification of illuminating stage. The main trick of the strategy is to restrict the illumination only to the sub-wavelength portion of the specimen. Manipulating the illumination process alters the classical condition of the diffraction limit and opens a loophole for reaching resolution of down to a few ten nanometer.

Stimulated emission depletion microscopy (STED), developed by Stefan W. Hell and Jan Wichmann in 1994, (experimentally demonstrated in 1999) perhaps is the most sophisticated method. It creates super-resolution images by the selective deactivation of

fluorophores, minimising the area of illumination at the focal point, and thus enhancing the achievable resolution for a given system. S. Hell and his colleagues shared the Nobel Prize in 2014 for STED methods.

Structured illumination microscopy (SIM) enhances the spatial resolution by collecting information from frequency space outside the observable region. Several shifted frames of illumination are required to compute the final image from the Fourier transformed map.

Spatially modulated illumination (SMI) modifies the Point Spread Function (PSF) of an optical microscope. SMI is a form of SIM in which the structured illumination is used to increase the precision of distance measurements of fluorescent objects. The result is resolution down to the molecular dimension of a few ten nanometer.

## 1.7.2 True Sub-wavelength Imaging

### 1.7.2.1 Near-field Scanning Optical Microscopy (NSOM)

After Veselago introduced the theory of resolution based on evanescent fields [26], attempts to develop super-resolved technology beyond conventional lenses focused on involving near-field features in the image formation. Many indirect super-resolution mechanisms such as near-field scanning microscopy and fluorescent microscopy are developed based on the capturing of evanescent waves. Most of these methods are strongly limited to surface objects. A small pin works as a detector and collects near-field emission at sub-wavelength distances from the specimen.

### 1.7.2.2 Negative Refractive Index Lenses and Super-Resolution

The first development of a true super-resolving optical imaging lens is credited to Sir John Pendry a decade ago [24]. Its design was based on Veselago's original work, which theoretically predicted the existence of negative refractive index materials. The lens is called negative refractive index lens or Pendry-type super-lens. The super-lens is a slab of material with negative values of both permittivity and permeability, ( $\epsilon = -1$ ,  $\mu = -1$ ), resulting in a negative index of refraction  $n = -1$ . Negative refractive index materials have many unusual and interesting optical properties which have never been observed in natural substances. Therefore, it took decades for Veselago's predictions of material with a negative index to turn into actual fabricated materials. However, it was Pendry who recognised that Veselago's lens have the power of evanescent fields enhancement: therefore, sub-wavelength imaging is possible due to the reversal of the exponential decay of evanescent waves.

The mathematical picture of above process can be understood as follows: Transport of energy in the  $+z$  direction requires the z-component of the wave vector to have the opposite sign:

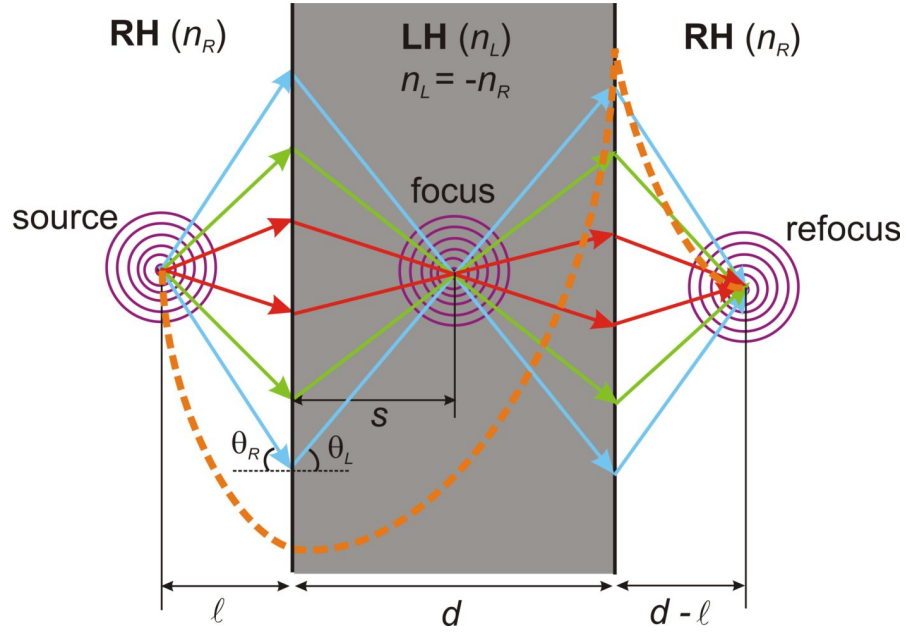


FIGURE 1.4: Negative refractive index lens enhances evanescent waves, resulting in sub-wavelength resolution (Source: Internet)

$$k'_z = -\sqrt{\frac{\omega^2}{c^2} - (k_x^2 + k_y^2)} \quad (1.16)$$

From Equation 1.16 it is clear that for large angular frequencies, the evanescent wave grows; so with proper lens thickness, all components of the angular spectrum can be transmitted through the lens undistorted. It seems that there are no problems with conservation of energy, as evanescent waves carry none in the direction of growth: the Poynting vector is oriented perpendicularly to the direction of growth. For travelling waves inside a perfect lens, the Poynting vector points in a direction opposite to the phase velocity. Detailed discussions of super-lenses and properties can be found in [23, 30].

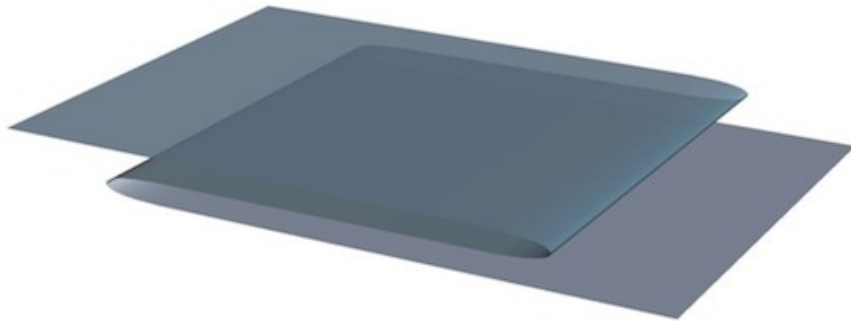


FIGURE 1.5: Physical space seems to run backward inside a negatively-refracting medium (Credit: Ulf Leonhardt).

However, further studies show that super-lenses are not flawless. When it comes to the practical and experimental realisation, some serious fundamental restrictions limit the performance of the super-lens [31–33]. One elegant way to visualise image formation in

negative refractive index lens is to interpret it in the transformation optics terminology [34] [35]. In this picture, negative refractive index lens resembles the topology of folded space. Thus in Figure 1.4 light emitted from the object is propagating through the

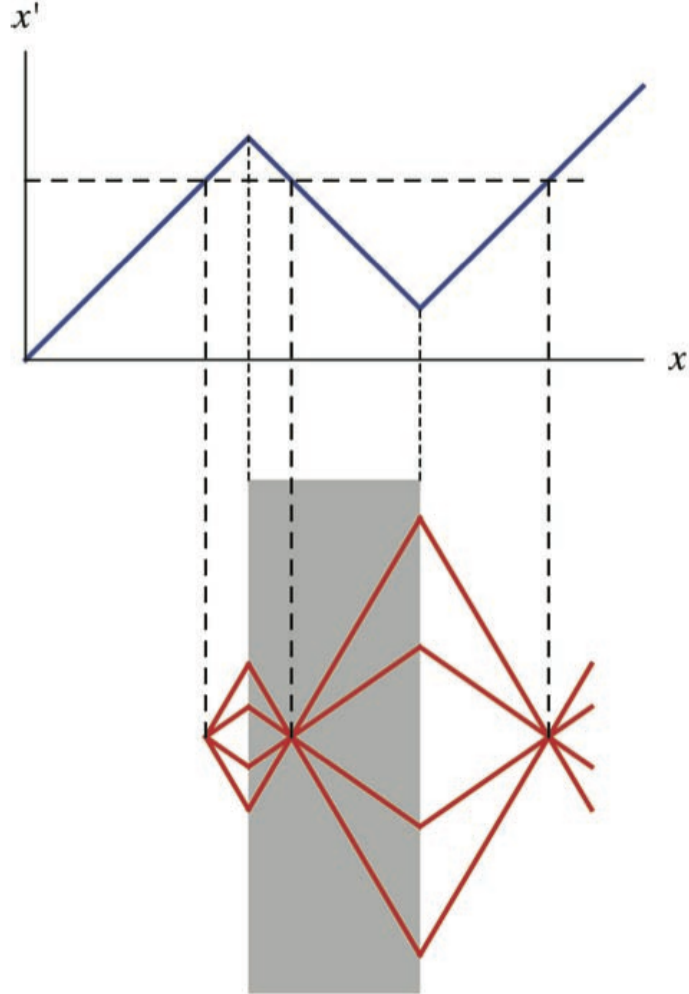


FIGURE 1.6: The top figure shows a suitable coordinate transformation from the physical  $x$ -axis to the  $x'$ -axis in vital space; the lower figure illustrates the corresponding device. The triple value segment on the  $x$ -axis corresponds to the focal region of the lens (Credit: Ulf Leonhardt).

media with positive-negative-positive refractive indices respectively and finally forms the image outside the lens in the medium with positive refractive index. According to [34] the geometrical picture of such a positive-negative-positive index medium corresponds to empty but folded space . Perfect imaging, which in this case means identical image and object, is a result of the fact that the field becomes multi-valued in folded space (Figure 1.6). If we accept the geometrical picture of folded space, Figure 1.5, for super-lens image formation, then, as Leonhardt and Philbin [34] showed, imaging power of super-lens in the broadband of frequencies might no longer be physical. As shown in

[35], analysing a flash of radiation propagating in the folded space, reveals restrictions on materials with negative  $\epsilon$  and  $\mu$ . In particular, it must be impossible for any medium to have  $\epsilon = \mu = -1$  for a narrow wave packet of radiation, and this restriction arises from the requirement that sources radiate forward in time with signal speed equal to  $c$ . This is indeed what a detailed analysis of electromagnetism in media shows [33]. It is only possible for material to have negative  $\epsilon$  and  $\mu$  for a very narrow range of frequencies, whereas a flash of radiation necessarily contains a very broad range of frequencies and  $\epsilon$  and  $\mu$  will be positive for much of that range. The perfect lens will in reality only operate for approximately monochromatic waves at a frequency where  $\epsilon$  and  $\mu$  are negative. Moreover, the same considerations lead to a conclusion that is not apparent from the transformation picture: negative  $\epsilon$  and  $\mu$  are unavoidably accompanied by significant absorption of the radiation by the material and this will degrade the image formation of the perfect lens [33, 35].

### 1.7.2.3 Perfect Focusing and Time Reversal Imaging

Three phenomena in physics schematically resemble each other: first, focusing of light beams into a spot smaller than a half wavelength; second localizing a quantum particle in a region smaller than its de Broglie wavelength; and third, imaging features smaller than a half wavelength through an optical device. Despite the scale differences, there seems to be a common resemble behind three: their intrinsic wave behaviour. Therefore, it is interesting to search for possible relations: for example, if better light focusing has a significant influence on changing the resolution limits. Obviously, though, the relation between sub-wavelength imaging and perfect focusing is quite subtle. Much work have been done to check if perfect focusing is possible in the wave regime[36, 37].

Let's consider an extreme case, an atom emitting radiation in  $\mathbf{R}^3$ . Due to the time reversal symmetry of Maxwell's equations, we can change the direction of time  $t \rightarrow -t$ . The question is if the emitted wave focuses back into the delta function or performs a finite extension. A time-reversed wave back-propagates and refocused exactly at its initial source. However, because of diffraction, even if the source is a perfect point, the time-reversed wave refocuses on a spot at least half a wavelength size. By using a time-reversal interpretation of this limit, De Rosny and Fink showed that the latter can be overcome if the source is replaced by its time-reversed image [27]. There are other methods based on time-reversal imaging which result in a super-resolution imaging. For further information see [27, 36].

## 1.8 Does Super-Resolved Imaging techniques Breaks The Diffraction Limit?

Does super-resolved imaging techniques break the diffraction limit? From the content of this chapter chapter, very probably the answer is not. The functional super-resolution techniques provide resolution extremely better than the conventional devices limits but only through the loopholes, so they do not break the “diffraction limit”. The true super-resolution devices on the other hand facing some practical barriers to overcome the limit. Explaining any individual case and arguing whether each method failed is far from the purpose of this thesis, we refer the interested reader, for example to [21, 22, 102]. However, the goal of this section is to raise the point that arguing over the violation of diffraction limit needs a rigorous definition of the “diffraction limit”. That is unavoidable unfortunate not to have a solid definition of a problem which takes the ample efforts of scholars to solve it. Among others, these two definitions might be the most accepted or as Maznev and Wright say “...defined in a reasonable way.”

**Definition 1.4.** “The period of the largest in-plane spatial Fourier component of the intensity profile at the image plane cannot be less than  $\lambda/2$ , where  $\lambda$  is the wavelength in the medium (or effective medium for a metamaterial).

**Definition 1.5.** More than 50% of the total energy cannot be focused into a spot smaller than  $\lambda/2$  in diameter.”[22].

where  $\lambda$  is the wavelength in the medium. Nevertheless, the equivalence of these two definitions never proved or argued in the literature. Accordingly, diffraction limit remains unbroken. Another ambiguity that seems never argued in the community is the relation between the perfect imaging in wave regime and diffraction limit. This diversity in the definitions is due to the heterogeneity of the properties of the systems under study. Any definition of diffraction limit tailored to describe the limitations of a particular system. For example, the near-field microscopy providing super-resolution based on the higher Fourier component of the source field and does not rely on the focusing feature. While the far-field time reversal, and far-field perfect focusing methods, hardly explain any mechanism to describe why the lack of evanescent component might lead to spreading the focusing light spot.

## Chapter 2

# Theoretical Background and Methods

### 2.1 The Scattering Problem and the Fermat Principle

Before going further to tackle the problem of diffraction limit we briefly introduce some theoretical background which is in the heart of methods we are using. Inverse problem, Fermat principle, and optico-mechanical analogy are theoretical bases behind the Maxwell Fisheye problem.

#### 2.1.1 General Introduction to the Inverse Scattering Problem

Inverse scattering problems have a central role in shaping our perception of the surrounding world. The simplest example is the human brain's ability to analyse the photons which scattered from the environment. Brain reconstruct the objects from the datas of the scattered photons. Most scientific observations are outcomes of inverse scattering analysis of detected parameters. Transformation optics which is a method used in this research is a form of inverse scattering problem, therefore in this chapter we briefly review the basic concepts in direct and inverse scattering theory.

In general, the scattering theory is the study of the long-time behaviour of a solution of evolution equations. Although it is quite common to apply the time-independent formulation of scattering by the Fourier transformation to momentum space, the relation between Fourier transformed problem and the actual experiments evolving in time is not always straightforward.

Any scattering problem includes the incident and scattered fields  $\mathcal{F}_i$  and  $\mathcal{F}_s$  evolving in space. Space can be a Euclidian geometry  $\mathbb{R}^N/\mathcal{D}$  or a general Riemannian manifold  $\mathcal{R}^N/\mathcal{D}$ . An incident field  $\mathcal{F}_i$  scatters off the target  $\mathcal{D}$  to produce  $\mathcal{F}_s$  :

$$\mathcal{F}_i \rightarrow \mathcal{F}_s \tag{2.1}$$

In fact, direct detection of  $\mathcal{F}_s$  is practically impossible and can only be achieved by subtracting the initial field from experimental results. In time-independent formulation, or for a stationary state, the experimental results  $\mathcal{F}$  would be given by:

$$\mathcal{F} = \mathcal{F}_i + \mathcal{F}_s \quad (2.2)$$

**The direct scattering problem** is to find the scattered field  $\mathcal{F}_s$  based on information about the scatterer in the closed bounded  $\mathcal{D}$ , with Dirichlet or Neumann boundary conditions on  $\partial\mathcal{D}$ . Mathematical formulation of the problem starts by finding the solution of the appropriate Helmholtz equation governing the total field in the region  $\mathcal{R}^N/\mathcal{D}$ . As we will see in further chapters, finding the proper Helmholtz equation for non-trivial geometries, is an elaborate task. But for wave propagation in flat Euclidian space we simply have:

$$\Delta\mathcal{F} + k^2\mathcal{F} = 0 \quad \text{in } \mathcal{R}^N/\mathcal{D} \quad \text{and} \quad \mathcal{F} = 0 \quad \text{on } \partial\mathcal{D} \quad (2.3)$$

Both parts of the field need to satisfy the equation while the following asymptotic condition is posed on the scattered field only:

$$\frac{\partial\mathcal{F}_s}{\partial r} - ik\mathcal{F}_s = \mathcal{O}(r^{-(N-1)/2}), \quad r \rightarrow \infty. \quad (2.4)$$

Hence, the family of solutions should be of the following form:

$$\mathcal{F}(r, k) = \mathcal{O}(r^{(N-1)/2})e^{ikx} + (r^{-(N-1)/2})e^{ikr}\mathcal{A}(r, k). \quad (2.5)$$

$\mathcal{A}(r, k)$  denotes the scattering amplitude and is the primary goal in a direct problem.

The above solution can be written in the familiar form:

$$\mathcal{F}(r, k) = (r^{(N-1)/2})e^{ikx}a(r) + (r^{(N-1)/2})e^{-ikr}b(r). \quad (2.6)$$

The coefficients of solutions  $a(r)$  and  $b(r)$  are apparently not independent. The map which connects the coefficients is a unitary operator called the scattering matrix or the S-matrix and is denoted by  $S(k)$ . It includes all the information about the scattering process:

$$b(r) = S(k)a(r). \quad (2.7)$$

The mathematical characteristic of the S-matrix manifests the physical nature of phenomena. For example, the poles of the S-matrix resemble the resonance points of the system or determine its causality and stability.

**The inverse scattering problem**, on the other hand, is solved by reconstructing the

properties of the scatterer localised in  $\mathcal{D}$  based on outgoing data from the scattered field or S-matrix. Again for wave propagation in flat Euclidian space  $\mathbb{R}^N$  with spherical symmetry, the asymptotic behaviour of the scattered field is given by:

$$\mathcal{F}_s(r) = \frac{e^{ikr}}{r^{(N-1)/2}} \mathcal{F}(\infty) + \mathcal{O}(r^{-(N-1)/2}), \quad r \rightarrow \infty. \quad (2.8)$$

However, the inverse problem, unlike direct scattering, is not always a well-posed problem. Precisely speaking, the existence, uniqueness, and stability of solutions are not guaranteed. Therefore, finding novel methods to solve inverse problems for elaborate systems is the subject of intensive research in physics and mathematics. In the following we will see that newly developed technique called transformation optics actually can be used as the inverse scattering method to design the optical instruments with unusual properties, especially when the geometry is not trivial. For this, we need, to begin with, the Fermat principle and see how an optical inverse problem can be formulated and solved by Fermat's fundamental law of nature.

### 2.1.2 The Fermat Principle

In classical and quantum mechanics the “*principle of least action*,” or “principle of stationary action” is considered as the most fundamental law of nature. In fact, this law was inspired by the prior version, called after Pierre de Fermat; ”*Principle of least time*”, describing the propagation of light in a medium.

Light travels between two points  $P_1$  and  $P_2$  in a way that minimises the duration of travel  $T$ :

$$T = \int_{P_1}^{P_2} dt \quad (2.9)$$

The principle of least time results in the concept of optical length in (spatial) 3-dimension:

$$S = c \int_{P_1}^{P_2} dt = \int_{P_1}^{P_2} \frac{c ds}{v dt} dt = \int_{P_1}^{P_2} n ds, \quad (2.10)$$

where  $n$  is interpreted as the response of space to the propagation of electromagnetic perturbations and  $s$  is the length parameter. In geometrical optics, light rays are trajectories orthogonal to the wave front which defines as the surface of constant phases  $\mathcal{S}(x, y, z) = Const$ . Along a particular ray of light, the relation between the point  $\mathbf{r}$  and the length parameter  $s$  is:

$$n \frac{d\mathbf{r}}{ds} = \text{grad } \mathcal{S}, \quad (2.11)$$

where  $n$  is the response of space to the propagation of light. Differentiation with respects to  $s$  gives:

$$\frac{d}{ds} \left( n \frac{dr}{ds} \right) = \text{grad } n. \quad (2.12)$$

when  $n$  is constant we have:

$$\frac{d^2r}{ds^2} = 0 \quad (2.13)$$

And the light path is a straight line. Light travels along the straight lines when space is homogenous. The homogeneity of space (or space-time) results in straight paths of light rays. Therefore, it is natural to expect that any non-homogeneity in space will deviate the light from a straight-line trajectory. An example is the optical illusion of mirage, which is the result of the non-homogeneity of air density. Another example is when light is bending in an inhomogeneous gravitational field due to the inhomogeneity of space-time [35]. However, in reality, both of above phenomenon follow the same principle:

$$\frac{d}{ds} \left( n \frac{dr}{ds} \right) = \text{grad } n \neq 0. \quad (2.14)$$

Therefore, it is possible to apply the same mathematical structure for describing both phenomenon. In the next part we will associate a metric to a medium to describe the behaviour of light when it is passing through.

### 2.1.3 Metrical Structure of the Medium and the Fermat Principle; Flat Space-Time

To find the metrical structure for the medium, let us consider a flat space-time with the metric:

$$ds^2 = c^2 dt^2 - d\ell^2, \quad (2.15)$$

where  $d\ell$  is the spatial distance element of the Euclidian space

$$d\ell^2 = dx^2 + dy^2 + dz^2. \quad (2.16)$$

According to special relativity, a light path in the vacuum is defined by the causal relation:

$$ds^2 = 0. \quad (2.17)$$

Consequently:

$$c^2 dt^2 = d\ell^2. \quad (2.18)$$

Here  $c dt$  is the infinitesimal spatial distance that light travels with a speed of  $c$  in the vacuum in the time interval  $dt$ .

The second axiom of special relativity says in an inertial framework, clocks and rulers (devices for measuring time and space) are correlated with each other such that for any frame in which  $dt$  is measured would have proper measuring results for the spatial counterpart  $d\ell^2$  to assure that causality  $ds^2 = 0$  remained invariant. Now assume a finite region of space which is filled with some medium:

$$\mu \neq \mu_0, \quad (2.19)$$

$$\epsilon \neq \epsilon_0,$$

Inside the medium, where the speed of light reduces to  $v < c$ , an infinitesimal spatial distance element along the light ray is defined by  $dl$ . However, if we accept the causal relation, then 2.17, is invariant inside the medium, so we require:

$$c dt = c dt \times 1 = c dt \times \frac{1}{v} \frac{dl}{dt} = \frac{c}{v} dl \quad (2.20)$$

the above expression can be written as:

$$ds^2 = c^2 dt^2 - n^2 dl^2 = 0 \quad (2.21)$$

Comparing equations 2.20 and 2.21 shows that substituting medium with vacuum does not effect  $ds^2 = 0$ . But, rather save the causal relation, the apparent form of spatial distance elements should chance

$$d\ell \longrightarrow dl \quad (2.22)$$

To preserve the causal relation, the apparent spatial paths inside the medium is changing to  $dl$ .

The Equation 2.20 is only valid if the observer who do the measurement in the vacuum ( $d\ell$ ) and the medium ( $dl$ ), stays in a single inertial frame.

The change of trajectories is strongly framework dependent when the temporal measurement of a phenomena is firmly constant, while the spacial measurement of the same phenomena is varying in a finite region of space due to the influence of medium. This is a situation that normally happens in the low speed  $u \ll c$  labs or daily experiences on earth. However, it is not easy to analytically determines  $dl$ . For some particular

coordinate system the relation:

$$dl^2 = \frac{1}{n^2} d\ell^2 \quad (2.23)$$

would determine the geometry of light inside the medium, but that is not a general statement. Modern version Fermat principle implies that the propagation of light between two points  $A$  and  $B$  is always determined by minimal time:

$$T = \int_A^B dt, \quad (2.24)$$

or, equivalently, that the optical path has to be an extremum (usually a minimum):

$$S = c T = \int_A^B c dt = \int_A^B c dt \times 1 = \int_A^B c dt \times \frac{1}{v} \frac{dl}{dt} = \int_A^B n dl \quad (2.25)$$

$S = cT$  is the “optical path” which is:

*The distance which light would cover in a vacuum during the time it takes the light to travel from one point in space (medium) to the other [26].*

We can read the relation 2.25 in a different way:

$$S = c T = \int_A^B c dt = \int_A^B c dt \times 1 = \int_A^B c dt \times \frac{1}{v} \frac{dl}{dt} = \int_A^B v ndt, \quad (2.26)$$

thus defining a new time  $\tau$  as:

$$ndt = d\tau. \quad (2.27)$$

we end in the equality:

$$\int_A^B c dt = \int_A^B v d\tau. \quad (2.28)$$

This can be interpreted as a specific time delay inside a medium: the speed of light reduces inside the medium while the measure of time for light changes. The light would not ‘recognise’ the change of speed as the time scale is changed to cover that. However, this time delation is different from the relativistic time delation which is a result of a Lorentz transform of the observer’s reference frame. Here the observer is at rest relative to the observed system.

In conclusion:

*Clocks not only work at different rates when they move with high speeds or are close to the black holes: they work differently when they are immersed in water.*

Applying the causal relation 2.17 to the interval  $A$  to  $B$  in the medium, we obtain:

$$\text{In the vacuum : } c^2 dt^2 - dl^2 = 0$$

$$\text{In the medium : } \left\{ \begin{array}{l} c^2 dt^2 - n^2 dl^2 = 0 \quad \text{or} \\ v^2 d\tau^2 - n^2 dl^2 = 0 \quad \text{or} \\ v^2 dt^2 - dl^2 = 0 \end{array} \right. \quad (2.29)$$

## 2.2 Optico-Mechanical Analogy

The kinematical analogy that holds locally between a point massive object in a gravitation field and a point massive objects under the corresponding non-gravity force is known as the strong equivalent principle.

This analogy is the fundamental de facto in classical physics that leads to the formulation of a geometrical theory of gravity by Albert Einstein <sup>1</sup>.

On the other hand, there is another possible analogy between a gravitational potential and an optical system.

For many of space-time metrics of interest, as the propagation of light is concerned, one can substitute the gravitational fields by a particular profile of optical refractive index.

<sup>2</sup> If this later analogy is a consequence of the equivalence principle or an independent one, is a matter of profound theoretical physics question and maybe out of the context of this theses. We call the later analogy optical-mechanical analogy. The terminology is coming from the more general situation. The analogy between the refractive index profile and force field is going beyond gravity and space-time metric. The analogy is valid, in principle, for any potential field. For example, one can find the equivalent refractive index profile for a Coulomb potential or the Kepler potential or even Yukawa potential.

There is two independent method to consider the optical-mechanical analogy, first in the framework of general relativity for the propagation of light, and the second consider it in the non-relativistic context for an object in a potential field. Calculating the properties of the optical medium with the equivalent refractive index for a particular potential is an inverse problem. Therefore, finding a solution for a particular potential is strongly bonded to our mathematical possibility for solving an inverse problem. If we like to work in the general relativistic picture, for a particular potential we might be able to correspond a particular geometry to a particular potential. Then we can speak of the

---

<sup>1</sup>General relativity is a geometrical theory of space-time. By geometrical, we mean interpreting gravity as geometry instead of force, or in more rigorous words, the covariant formulation of the theory which it is a direct consequence of equivalent principle

<sup>2</sup>The question whether other massless or massive fields rather than electromagnetic fields are following optical-mechanical analogy or not is another issue that needs further investigation that is out of scope of this thesis.



FIGURE 2.1: Curved lines in curved space-times, would act as straight lines in our world. They are geodesics of light paths, but observation of those residents in the non-Euclidean world would be a little bit different. This picture shows Hebe, Greek goddess of youth, looking at herself in curved space. (Credit: Aaron Danner [35])

geometry of light. The only restriction is then just for very particular metrics with the symmetrical character one can find known geometric features and solvable equivalent refractive index. In general cases, a potential (both in GR or non-GR picture) might correspond to an inhomogeneous anisotropic optical medium. For simplicity, here we first analysis the optical-mechanical analogy for cases with isotropic symmetry. We would see the analogy in both metric examples and non-relativistic potential examples.

### 2.3 Brief Introduction to Transformation Optics

In the mid-seventies, Plebanski formulated the analogy between the empty curved space-time and the magneto-electric media [38]. But, just in the recent years [34, 35, 43] the complete analysis, in term of transformation optics, reveals the essential conditions and fundamental restrictions for such an analogy in practice.

The underlying principle of such a geometrical analogy is the conformal invariance of electromagnetic fields which allows a diffeomorphism between an arbitrary curved vacuum (called virtual space-time or electromagnetic space) and the designed medium that serves as the real space-time. One of the crucial conditions which allow this analogy is the impedance-matched feature of the medium. An impedance-matched material is a magneto-electric medium that satisfies the condition:  $\mu = \epsilon$ . The term "impedance-match" refers to impedance invariant property of the medium  $\mathbf{z} = \sqrt{\epsilon/\mu} = \sqrt{\epsilon_0/\mu_0}$  compare to vacuum. An impedance-matched medium resembles some of the electromagnetic responses of the vacuum. However, as the impedance-matched anisotropic

materials are very rare in nature, applying this analogy had been restricted to some theoretical studying.

“Transformation Optics” as a new branch of applied optics, was introduced to the community [34, 35, 39–41]. While, due to its concrete practicality, attracts the attentions and developed into a multidisciplinary research field of theoretical and numerical physics and engineering. Coincidentally, technological developments in artificially structuring materials namely metamaterial science demanded the solid theoretical framework for the systematic design and innovations.

Transformation optics provides theoretical means to exploit new emerging technology to control electric and magnetic fields [40]. These developments were opening new possibilities to apply the science of classical electrodynamics in the larger domain. Moreover, these sort of techniques can be used to solve a particular family of inverse scattering problems in electrodynamic systems.

John Pendry and Ulf Leonhardt among the pioneers widely established transformation optics as an independent field includes methods of geometry to manipulate electromagnetic files in innovative ways. The field introduced with dramatic illustrations such as optical Invisibility devices [40, 41], perfect imaging lenses [16, 24] and optical analogue of event horizon [35, 42]. In the following, we will briefly review both approaches of Leonhardt and Pendry and their subtle distinction.

### 2.3.1 Conventional Formulation

Transformation optics, as a computational technique, developed by Ward and Pendry in 1996 while working on computing wave fields in photonics crystals [39]. Photonics crystals are some dielectric structures with periodical permeability and permittivity. Interesting fact about Photonics crystals is that they response to photons the same way as semiconductors behave in the presence of electrons. This resemblance is due to the analogy between Schrödinger equation in semiconductors with Helmholtz equation for the field in photonics crystals. More accurately, a periodic refractive index in Helmholtz equation is an analogue to periodic electrical potential in Schrödinger equation. This analogy between the electromagnetic property of dielectrics with the mechanical motion of particles in a potential was an old well-known fact dated back to Newton’s time. However, using this resemblance and accordingly developing a new technique was an elegant way to ease the computation of Maxwell’s equations in an inhomogeneous region of space which both  $\mu$  and  $\epsilon$  are sharply changing over the space. Sharp changes in  $\mu$  and  $\epsilon$  over space corresponds to continuously rescaling some parameters like wavelength, thus, resulting in the severe difficulties in computing the Fourier decomposition of wave field over the non-uniform mesh of coordinates. In Ward-Pendry method this problem reduces to two step:

- 1) Solving Maxwell's equations over the uniform mesh of coordinate.
- 2) By proper coordinate transformation locally transform the solution/equation from uniform to non-uniform coordinate mesh.

Coordinate invariance of electromagnetic theory would guarantee the identity of the form of Maxwell's equations.

$$\begin{aligned} \nabla \times \vec{E} &= -j\omega[\epsilon]\vec{H} \\ \nabla \times \vec{H} &= j\omega[\mu]\vec{E} \end{aligned} \Rightarrow \text{Coordinate Transform} \quad \begin{aligned} \nabla' \times \vec{E}' &= -j\omega[\epsilon']\vec{H}' \\ \nabla' \times \vec{H}' &= j\omega[\mu']\vec{E}' \end{aligned} \quad (2.30)$$

The consequence of coordinate transform appears as a new dispersion relation. The coordinate transformation would be completely absorbed into the materials property so if now look at the field from primary coordinate we may see the different medium.

$$\begin{aligned} \nabla' \times \vec{E}' &= -j\omega[\epsilon']\vec{H}' \\ \nabla' \times \vec{H}' &= j\omega[\mu']\vec{E}' \end{aligned} \Rightarrow \text{Pull Back} \quad \begin{aligned} \nabla \times \vec{E} &= -j\omega[\epsilon'']\vec{H} \\ \nabla \times \vec{H} &= j\omega[\mu'']\vec{E} \end{aligned} \quad (2.31)$$

Then the computation process will reduce to solving one set of the Maxwell equation on the appropriate uniform mesh of coordinate which locally changing the refractive index respectively.

We can use this strategy for the different set of problems. Designing media in which we can control the flow of Electromagnetic fields.

Assume a desirable pattern for the EM field, chose a manifold with a similar topology but confined either to free space or a simple configuration of permittivity and permeability then continuously reshape the coordinate mesh to reach your assumed field pattern. In vast useful cases such continuous field pattern reshaping might be described by a coordinate transformation like the following:

$$\vec{r}(x, y, z) \Rightarrow \vec{r}'(x', y', z') \quad (2.32)$$

If we began from Cartesian coordinate in free space, then we are sure that always a coordinate transformation exists for any elastic reshaping of the system.

Functions and operators transform between the coordinates by aid of Jacobian tensor:

$$[\Lambda] = (\nabla \vec{r}')^T = \begin{bmatrix} \frac{\partial x'}{\partial x} & \frac{\partial x'}{\partial y} & \frac{\partial x'}{\partial z} \\ \frac{\partial y'}{\partial x} & \frac{\partial y'}{\partial y} & \frac{\partial y'}{\partial z} \\ \frac{\partial z'}{\partial x} & \frac{\partial z'}{\partial y} & \frac{\partial z'}{\partial z} \end{bmatrix} \quad (2.33)$$

We can Maxwell's equations in the new coordinate system, knowing that how vectors and operators may change under coordinate transformations. Vectors are transforming by the Jacobian tensor as the following:

$$\vec{E}'(\vec{r}') = ([\Lambda]^T)^{-1} \vec{E}(\vec{r}) \quad (2.34)$$

$$\vec{E}(\vec{r}) = ([\Lambda]^T) \vec{E}'(\vec{r}') \quad (2.35)$$

And material's property tensors as transform as:

$$[\mu'] = \frac{([\Lambda])\mu([\Lambda]^T)}{\det[\Lambda]} \quad [\epsilon'] = \frac{([\Lambda])\epsilon([\Lambda]^T)}{\det[\Lambda]} \quad (2.36)$$

These new values of permittivity and permeability are the ones we need to give to our designed materials if we want the fields to take up the desired paths.

### 2.3.2 Geometrical Formula; Special Transformation

Described method of transformation optics as came in the previous subsection, is mainly applicable when the final desired pattern of EM fields, in the medium, is an elastic local distortion from the free space geodesics. The advantage of this method is the simplicity of the algorithm. However, from the theoretical point of view, there is a significant subtlety in the mathematical structure of transformation optics, beyond the calculational purposes. Leonhardt-Philbin's reformulation of transformation optics [34, 35] represents this mathematical beauty and technically brought the realm of general relativity into the field of applied optics and vice versa. In this perspective grids of coordinate are not only chosen the network of mesh to simplifies the calculations but rather geodesics of space or space-time which reflect the geometry of the physical region of space. Accordingly, transformation takes place between metrics of different spaces. This formula is more potent when one is interested in manipulating the light in the global geometry rather than local distortions or when the metric of desired space is in hand. A good example is confining the light to propagate in a particular non-Euclidian geometry, or gravity analogy studies [43, 44].

Real space or physical space is the vacuum space of observer. It might be a flat space, as we are on the earth, or a curved vacuum if the lab located near a large celestial mass. In each case, we need to choose a proper coordinate fit to our particular problem.

Maxwell's equations connect the electric fields with corresponding magnetic fields through the curl operator  $\nabla \times$  operator and imply the relation between those fields with the

sources (charges and currents) by the divergence operator  $\nabla \cdot$ .

$$\nabla \cdot E = \frac{\rho}{\epsilon_0} \quad \text{GAUSS'S LAW} \quad (2.37a)$$

$$\nabla \times B = \frac{1}{c^2} \frac{\partial E}{\partial t} + \mu_0 j \quad \text{AMPERE'S LAW} \quad (2.37b)$$

$$\nabla \times E = - \frac{\partial B}{\partial t} \quad \text{WITH MAXWELL'S DISPLACEMENT CURRENT} \quad (2.37c)$$

$$\nabla \cdot B = 0 \quad \text{ABSENCE OF MAGNETIC MONOPOLE} \quad (2.37d)$$

Mathematical operators of curl and divergence have the general forms in arbitrary curvilinear coordinates. Therefore, covariant Maxwell equations in an arbitrary curvilinear vacuum would turn to:

$$\frac{1}{\sqrt{g}} (\sqrt{g} E^i)_{,i} = \frac{\rho}{\epsilon_0} \quad (2.38a)$$

$$\epsilon^{ijk} E_{k,j} = - \frac{\partial B}{\partial t} \quad (2.38b)$$

$$\epsilon^{ijk} B_{k,j} = \frac{1}{c^2} \frac{\partial E^i}{\partial t} + \mu_0 j^i \quad (2.38c)$$

$$\frac{1}{\sqrt{g}} (\sqrt{g} B^i)_{,i} = 0. \quad (2.38d)$$

$$(2.38e)$$

From differential geometry, we know that the relation between covariant and contravariant tensors (tangential and congenital spaces), expresses the geometry of the underlying manifold in the form of the metric tensor  $\mathbf{g} = g_{ij}$ .

For any arbitrary vector/tensor  $A_i$  the relation between covariant and controvariant elements is:

$$A_i = g_{ij} A^j \quad \text{and} \quad A^i = g^{ij} A_j \quad (2.39)$$

By the contravariant components into covariant ones then we can see that the Maxwell equations possess a remarkable property [45]

$$(\sqrt{g}g^{ij}E_i)_{,i} = \frac{\sqrt{g}\rho}{\varepsilon_0} \quad (2.40a)$$

$$[ijk]E_{k,j} = -\frac{\partial(\pm\sqrt{g}g^{ij}B_j)}{\partial t} \quad (2.40b)$$

$$[ijk]B_{k,j} = \frac{1}{c^2} \frac{\partial(\pm\sqrt{g}g^{ij}E_j)}{\partial t} + \sqrt{g}j^i \quad (2.40c)$$

$$(\sqrt{g}g^{ij}B_j)_{,i} = 0 \quad (2.40d)$$

If one observe/interpret the field equations in right-handed Cartesian coordinates, instead of arbitrary curveilinier ones, then might read some of the terms as below:

$$\varrho = \sqrt{g}\rho \quad , J^i = \sqrt{g}j^i \quad (2.41a)$$

$$\varepsilon_0\varepsilon^{ij}E_j = D^i, \mu_0\mu^{ij}H_j = B^i \quad (2.41b)$$

$$\varepsilon^{ij} = \mu^{ij} = \pm\sqrt{g}g^{ij} \quad (2.41c)$$

They looks like ordinary macroscopic Maxwell's equation for electromagnetic waves in dielectric media:

$$D_{,i}^i = \varrho \quad \text{or} \quad \nabla \cdot D = \varrho \quad (2.42a)$$

$$B_{,i}^i = 0 \quad \text{or} \quad \nabla \cdot B = 0 \quad (2.42b)$$

$$[ijk]E_{k,j} = -\frac{\partial B}{\partial t} \quad \text{or} \quad \nabla \times E = -\frac{\partial B}{\partial t} \quad (2.42c)$$

$$[ijk]H_{k,j} = -\frac{\partial D}{\partial t} + J^i \quad \text{or} \quad \nabla \times E = -\frac{\partial D}{\partial t} + J^i \quad (2.42d)$$

However, the above derivation was carried out under the particular assumption that,  $\varepsilon = \mu$ . Such materials are called impedance-matched media.

In electrical engineering, the ratio of  $\sqrt{\frac{\mu}{\varepsilon}}$  known as impedance, and it usually denotes by  $Z$ ; Constant values of  $Z$  implies some geometrical features of the material. For impedance-matched media  $Z$  is clearly equal to unity  $Z = 1$  as in the free vacuum. Constant values for  $Z$  in an anisotropic material give rise to nontrivial (effective) geometries. Impedance-matched materials preserve some geometrical properties of vacuum.

$$\varepsilon^{ij} = \mu^{ij} = \pm\sqrt{g}g^{ij} \quad \text{Therefore} \quad \sqrt{\frac{\mu}{\varepsilon}} = 1 \quad (2.43)$$

This geometry is described below:

$$g^{ij} = \frac{\varepsilon^{ij}}{\det \varepsilon} \quad (2.44)$$

Or in matrix notation:

$$\mathbf{g} = (\det \varepsilon) \varepsilon^{-1} \quad (2.45)$$

We, therefore, obtain the particular category of materials which induce geometry to the electromagnetic fields. In some sense, a dielectric material is behaving in a way that is similar to the gravitational properties of matter.

In the other word, geometry appears as a refractive index profile for the material, which is given by:

$$\mathbf{n}^2 = (\det \varepsilon) \varepsilon^{-1} = \mathbf{g} \quad (2.46)$$

The induced effective geometry of the medium, topologically, can be curved or flat. In 3-dimension, non-zero Ricci tensor,  $R_{ij}$ , implies the intrinsic curvature. On the other hand, zero value for Ricci tensors  $R_{ij} = 0$  denotes the intrinsic flatness. However, it does not refute the local curvature in the metric or accordingly in the derived geodesics for light in the medium.

The later case,  $R_{ij} = 0$  has an interesting property: there exists a coordinate transformation that turns the Maxwell equations from arbitrary coordinates into those of flat space, with a right-handed Cartesian system. So the electromagnetic fields in real space appear as coordinate-transformed fields from flat, empty space. Such media are called transformation media. These have been used in a variety of promising applications, including perfect lenses and invisibility devices.

## Chapter 3

# The Maxwell Fisheye Medium

### 3.1 The Maxwell Fisheye Medium

Imagine an optical point source, located at point  $P$  in  $\mathbb{R}^3$ , is emitting the light rays into space. The infinite number of rays diverge from point  $P$  to the infinity. In the primary education, we had learned that light rays are travelling on the straight lines. In the terminology of differential geometry, each ray of light is a geodesy of the Euclidian manifold  $\mathbb{R}^3$ . As  $\mathbb{R}^3$  is an unbounded geometrical space, it is possible to proof <sup>1</sup> that there is no point like  $P'$ , in the entire  $\mathbb{R}^3$ , that all the light rays/geodesics initiated from  $P_0$  converge into that.

In the simple words, this statement says a conventional single aperture or slit like those tackled by the Rayleigh's resolution formula is not able to collect all of the rays emitted from a point source. Even an infinitely large aperture, ideally, would receive only half of the rays emitted from a single source. The ray collection factor is a parameter that appears in the Abbe limit as the optical power of the device. This restriction is known as one of the underlying reason for limited resolution of an optical device which it demonstrates self as the finite value of the aperture number.

However, if light, instead of straight paths goes along the closed elliptical orbits, as in the AI, the rays that emit from a point can converge again into another point <sup>2</sup>.

Based on the theory of General Relativity, we know in a curved space-time, i.e. in a strong gravitational field, the light will travel in the closed orbits. In the previous chapter, we have seen that, in theory, for any mechanical potential there is an optical analogue. A consequence of Snell laws that light can go through a transparent medium on the non-straight lines. Whether any particularly designed lens (later called Fisheye) can gather the entire rays, initiated from a point source, or not was a subject of paper that the young J. C. Maxwell addressed in 1854.

---

<sup>1</sup> Based on an axiom which states that straight lines cross once or never in the Euclidian spaces.

<sup>2</sup> A mathematical theorem called "Singularity Theorem" in differential equation proves it

The properties of the Maxwell Fisheye are described in one of a number of set problems or puzzles in the 1853 Cambridge and Dublin Mathematical Journal. The challenge is to find the refractive index as a function of radius, given that a ray describes a circular path, and further to prove the focusing properties of the lens. The solution is given in the 1854 edition of the same journal.

**Problem:** [Assume] a transparent medium is such that the path of a ray of light within it is a given circle, the index of refraction being a function of the distance from a given point in the plane of the circle. Find the form of this function and show that for light of the same refrangibility:

1. The path of every ray within the medium is a circle,
2. All the rays proceeding from any point in the medium will meet accurately in another point.
3. If rays diverge from a point without the medium and enter it through a spherical surface having that point for its centre, they will be made to converge accurately to a point within the medium.

This problem was the puzzle that J. C. Maxwell addressed in his paper [46]. To solve the challenge he used trigonometry and Newtonian mechanics to proved two following Lemmas:

**Lemma 3.1.** *Let a transparent medium be so constituted, that the refractive index is the same at the same distance from a fixed point, then the path of any ray of light within the medium will be in one plane, and the perpendicular from the fixed point on the tangent to the path of the ray at any point will vary inversely as the refractive index of the medium at that point.*

**Lemma 3.2.** *If from any fixed point in the plane of a circle, a perpendicular is drawn to the tangent at any point on the circumference, and then the rectangle contained by this perpendicular. moreover, the diameter of the circle is equal to the square of the line joining the point of contact with the fixed point, together with the rectangle contained by the segments of any chord through the fixed point.*

Through these two lemmas, J. C. Maxwell calculates the refractive index profile of the supposed medium as:

$$n(r) = \frac{2n_0}{1 + (\frac{r}{a_0})^2}. \quad (3.1)$$

He adds “the existence of the medium was suggested by the contemplation of the structure of the crystalline lens in fish”... [46]. Therefore, the lens called after him Maxwell Fisheye or as we call it Maxwell Fisheye Medium (MFE). In the formula,  $r$  is the distance from the centre of the lens and  $n(r)$  is the refractive index, while  $n_0$  denotes the

refractive index of the environment that the lens is embedded, which usually would be the air. Therefore  $n_0 = 1$ . Constant  $a_0$  is the characteristic scale which is used to renormalize the units in term of wavelength. In practice, the characteristic scale will be the radius of the lens. The advantage of the MFE is the ability to collect, the total rays from an emitting source and recombine them in-phase at another point of the lens. However, the MFE suffers from an impractical fact: as the formula shows the lens covers the entire space, i.e.,  $r$  can reach the infinity.

### 3.2 Geometrical Properties of the Maxwell Fisheye

Almost a century later in 1964, in his book, “Mathematical Theory of Optics”, R. K. Luneburg gave an illustrative description of the Maxwell Fisheye medium[47]. According to Luneburg, Maxwell Fisheye medium can be interpreted as a conformal map of a sphere  $S^n$  into the  $R^n$ .

In the Luneburg picture, the MFE is demonstrated as light rays propagating on the surface of the  $n$ -sphere along the geodesics, namely, the great circles. Consider a bundle of light rays emitted at one point. All the great circles crossing at this point must meet again at the antipodal point on the sphere, see figure 1(B). This interpretation brings up significant advantages. Instead of working with the inhomogeneous medium we can work with spherical geometry and vice versa. So, we can refer to MFE as an inhomogeneous optical medium in  $R^n$  or equally surface of a  $n$ -sphere where, in practice,  $n$  can be  $n = 1, 2, 3$ .

The stereographic projection maps any circle on the sphere to circles on the plane. Consequently, in an optical implementation of the stereographic projection, in MFE, all light rays are circles and all rays from one point meet at the projection of the antipodal point, creating a perfect image.

A characteristic feature of the stereographic map between the sphere and the plane is that straight lines in the Euclidean plane correspond to great circles on the sphere, therefore, if one can constrain the light to travel in the two-dimensional world of the sphere, then they will propagate on the great circles. Moreover, what is here remarkable for us is that those circles on the sphere which do not pass through the point of projection are projected to circles on the plane and circles on the sphere that does pass through the point of projection are mapped to straight lines on the plane. These lines are sometimes thought of as circles through the point at infinity, or circles of infinite radius. Therefor, stereographic map preserves the circle.

The stereographic projection is a conformal map, i.e.; it preserves the angles through the transformation. The Luneburg interpretation of MFE is held because the electromagnetic theory is conformal invariant.

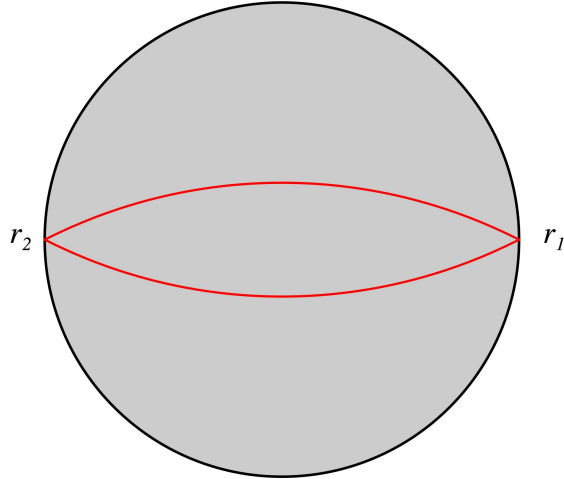


FIGURE 3.1: A light ray emitted from a point source propagates along the geodesics of the sphere and converge back at the antipodal point.

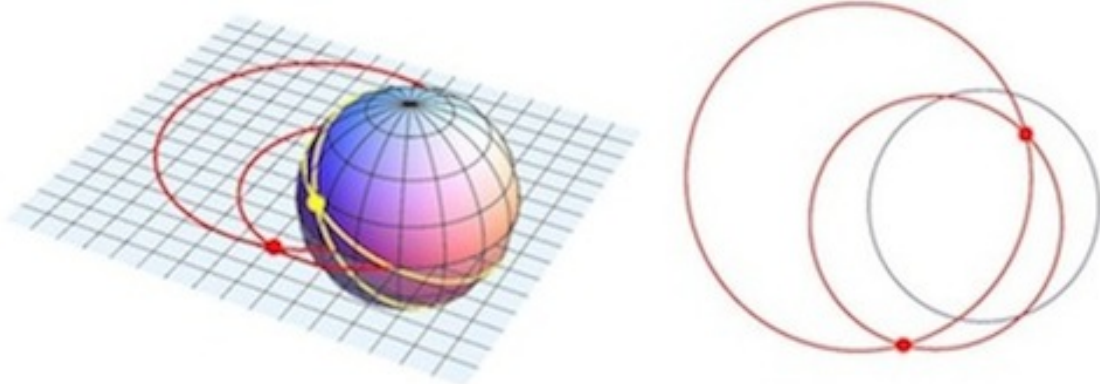


FIGURE 3.2: Circles on the sphere which do not pass through the point of projection are projected to circles on the plane

### 3.3 Inverse Scattering Problem and Spherically Symmetric AI

In Chapter 2 we have seen that optico-mechanical analogy state a formal equivalence between the trajectory of a mechanical particle moving in a force field and paths of light rays in an inhomogeneous medium [35, 48]. As a problem to solve, one can think of finding the optical analogous of a particular mechanical system: for example, celestial force. This is the strategy that brought the young Maxwell to the idea of Fisheye medium; A lens with the maximum focusing power [49]. MFE is a geodesic lens, guiding waves over the geodesics of the medium which is generated by the gradient refractive index profile. MFE is an optical Absolute Instrument (AI) (see Chapter 1). By definition, AI is any optical imaging device that performs a sharp, strong image in the geometrical optics regime. The key feature that makes an instrument absolute is perfectly focusing capability. The Maxwell Fisheye is the archetype of the AI, and a very remarkable one,

in the term that it is an optical AI *of the first kind*. That means MFE makes a strong, stigmatic, full image of a point source located anywhere inside the medium.

MFE is a member of a larger family of optical AI: the family of lenses with isotropic spherically symmetric refractive index profiles  $n(\mathbf{r}) = n(r)$ . This family is an optical analogous of a particular mechanical system: central force or mechanical focusing potential. In both case the is radial symmetry in the system. The radial symmetry of the focusing potential allows the MFE to be an aberration-free device, because it collects the light rays entirely and focuses them perfectly, along with the equal length trajectories. Designing perfect lenses with radial symmetry is an inverse scattering problem. This problem was probably solved first by Luneburg in his lectures on optics at Brown University in 1944. In 1953, Firsov independently developed the same procedure for the equivalent problem in classical mechanics. With the inverse formula and given parameters one can derive the optical medium as a counterpart of potential field [48]. We derive the refractive index profile of the MFE using the Luneburg-Firsov inverse scattering formula.

The trajectory of a particle which scattered from a central potential can be calculated by a pair of parameters, which can be either; the velocity at infinity and the impact parameter  $b$ , or the total energy and the angular momentum.

The deflection angle (the angle of which the particle is scattered from its initial direction) can be a function of each pair of parameters. Given the deflection angle  $\varkappa$  and particular values of this parameter we can determine the potential  $U(r)$ . Here, we assume to have particles with different energies, and, therefore, the different velocities. They are scattering from an arbitrary central force  $U(r)$ . According to Luneburg-Firsov inversion algorithm, we can calculate the potential  $U(r)$  only knowing the angle of deflection  $\varkappa$  for a particular particle  $a$ , which has the total energy  $E_a = E(b)$ . Energy is a function of the impact parameter  $b$ . In Firsov's original formula, another quantity appears, which is a function of potential:

$$n(r) = \sqrt{1 - \frac{U(r)}{E_a}} = \frac{v(r)}{v(\infty)} \quad (3.2)$$

where, the  $v(r)$  is the velocity of the particle at the given point  $r$ , and the  $v(\infty)$  is an asymptotic velocity of the particle at infinity. If one Interpret the function  $n(r)$ , in Equation 3.2, as an optical refractive index, there would be an analogy between a mechanical scattering with an optical system.

Equation 3.3 shows the complete form of Luneberg-Firsov equation. Here,  $n(r)$ , refractive index, can be written in terms of angle of deflection  $\varkappa$  and the impact parameter  $b$  (Figure 3.3).

$$n(\rho) = \exp\left[\frac{1}{\pi} \int_{\rho}^{\infty} \frac{\varkappa(b)db}{[b^2 - \rho^2]^{1/2}}\right]. \quad (3.3)$$

where

$$\rho = rn(r) \quad (3.4)$$

and

$$\varkappa = \sin \alpha_1 - \sin \alpha_2 \quad (3.5)$$

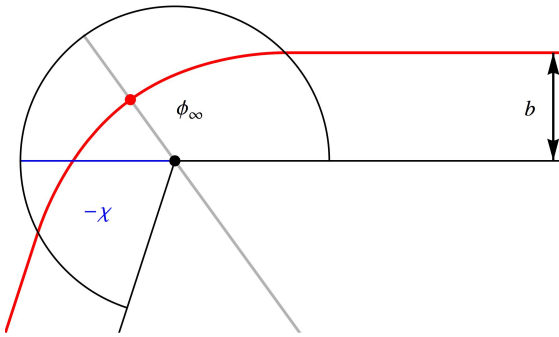


FIGURE 3.3: Scattering from a central force field

The turning parameter  $\rho$  is the impact parameter  $b$  for which the trajectory has a radial turning point at  $r$ . The reconstruction formula 3.3 is implicit because  $n$  is not directly expressed as a function of the radius but rather expressed in terms of the turning parameter. Not all scattering data are physically allowed because the function  $n(r)$  might be multi-valued (it may have several values of  $n$  for the same radius  $r$ ). If  $n(r)$  is single-valued, Firsov inversion formulae, 3.3 and 3.4 establish a refractive-index profile that implements the scattering data  $\varkappa(b)$ . To guarantee the uniqueness of the solution,  $\rho$  as a function of  $r$  must increase monotonically by rising of  $r$  [48].

To derive the refractive index profile for MFE from the Luneburg-Firsov algorithm, one should indicate the characteristic features of MFE:

- All rays follow the circular orbits lie in a plane which passing the centre of symmetry.
- For any chosen point  $P$  there is an antipodal  $P'$  that any ray passes through  $P$ , must go through  $P'$  too.
- The resulting image is an inversion.

To satisfy the above conditions the medium extends to the radius  $R$ . Light emitted at the point  $P$  should be focused on the opposite side of the equator. Thus we require:

$$r_1 = r_2 \quad r_2 = R \quad (3.6)$$

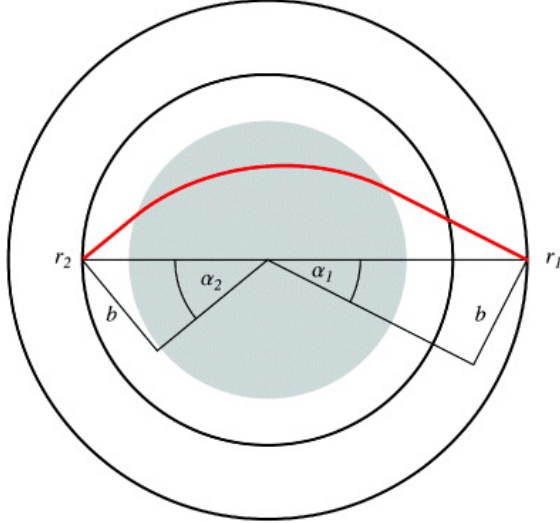


FIGURE 3.4: Consider light rays (red) that may pass through a spherically symmetric medium (darker region). We require that all rays that do pass through the medium from radius  $r_1$  arrive at radius  $r_2$  exactly opposite to their starting point (meaning that the starting point and the end point lie on a straight line through  $r = 0$ ). We characterise the rays by their impact parameters  $b$ . The impact parameter is proportional to the angular momentum and is, therefore, a conserved quantity, as the figure indicates. The initial and final segments of the trajectories are inclined by the angles  $\alpha_1$  and  $\alpha_2$ . The drawing shows that  $b = r_1 \sin \alpha_1 = r_2 \sin \alpha_2$ , which is all we need to know for solving Luneburg's design problem.

$$\sin \alpha_i = \frac{b}{r_i} = \frac{b}{R} \quad (3.7)$$

Therefore:

$$\varkappa = \sin \alpha_1 = \sin \alpha_2 = \arcsin b/R \quad (3.8)$$

Luneburg's Integral becomes:

$$n(\rho) = \exp \left[ \frac{1}{\pi} \int_{\rho}^R \frac{(\arcsin b/R) db}{[b^2 - \rho^2]^{1/2}} \right] = \frac{\pi}{2} \ln (1 + \sqrt{1 - (\rho/R)^2}) \quad (3.9)$$

from the reconstruction formula 3.9, we obtain the index profile in terms of the turning parameter:

$$n(\rho) = 1 + \sqrt{1 - (\rho/R)^2} \quad (3.10)$$

By substituting this result in definition 3.4 of the turning parameter and solve the resulting equation for  $\rho$ , we get the Maxwell's profile for Fisheye:

$$n(r) = \frac{2}{1 + (r/R)^2} \quad (3.11)$$

The MFE may act as a perfect imaging device in ray optics if we take  $r$  from 0 to infinity, but also it will keep the functionality if we terminate the refractive index profile at  $R$  and surround it by a mirror [16]. In this case, the refractive index ranges from 1 at  $R$

to 2 at the centre. By assuming different condition on Equation 3.3 one can reconstruct different media.

However, as we mentioned, to guarantee the uniqueness of solutions, there are subtle conditions that one needs to concern while applying this algorithm which can alter base of the complexity of the potential.

In the central force problems, such as Kepler problem or the hydrogen atom, conservation of the angular momentum results in a planar motion, similarly, in optical analogues with the spherical symmetry media, the propagation of light is restricted into a plane passing through the centre. The reason is constancy of the impact parameter, which is proportional to the angular momentum and therefore imposes a sort of conservation on the light trajectories.<sup>3</sup> This feature has a great advantage, for example, to reduce the dimension of the problem under study. In the radially symmetric optical media, the pathway of propagating light can be a closed loop, similar to the trajectory of a particle, with the non-positive energy, moving in the central force. Maxwell Fisheye lens or the Miñano lens have closed light orbits. In such cases, usually, the object and image are both confined inside the medium.

### 3.3.1 The Modified MFE

We will apply the same algorithm to derive another member of the AI family. In original mirrored MFE refractive index changes from 2 at the centre to 1 at the edges. In practice, fabricating a material with refractive index 2 is a cumbersome engineering problem. Our aim is to ease the fabricating requirements compare to MFE. Whether this relaxing of requirements would influence the focusing quality of the new device compare to original MFE is the subject of section 3, Chapter 5. We would call the resulting medium the modified Maxwell Fisheye. The goal of the modification is to reduce the range of the refractive index. Suppose that the two radii  $r_1$  and  $r_2$  in Luneburg's design problem Figure 3.4 are the same,

$$r_1 = r_2 \quad (3.12)$$

but  $R < r_1$ , and we surround the device by a mirror at the radius  $r_1$ . The light coming from a point  $P$  on the mirror is focused on the other side and reflected, whereupon it goes through the focusing medium once more and returns to  $P$ . Consequently, light rays form close loops, provided they strike the focusing index profile. Suppose that we pick the point  $r$  inside the medium that lies on a ray trajectory. As all light rays that strike the medium form closed loops, so must all rays going through  $r$ . The radial symmetry of the device implies that all these rays must also go through  $-r$ . Therefore, a source at  $r$  is perfectly imaged at  $-r$  Figure 3.5. However, if the source is outside of the focusing

---

<sup>3</sup>For proof look at [35], chapter 2.

profile,  $r > R$ , not all ray trajectories are closed, and the image is not perfect (Figure 3.5). In the case of the original MFE mirror [16], all ray paths are closed, because  $r_1 = R$ , no rays lie outside the focusing medium. What does it take to make a modified MFE mirror? We obtain from the reconstruction formula 3.3 and relation 3.4 with the angles 3.5, 3.7 and condition 3.12:

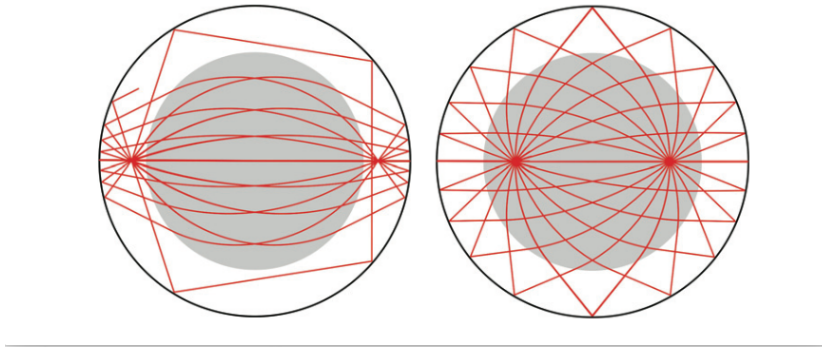


FIGURE 3.5: Modified MFE mirror. Left: light emitted from a point outside the focusing index profile. Not all rays are focused at the image point. Right: perfect imaging within ray optics if the light is emitted inside the index profile.

$$r(\rho) = (\rho) \exp \left[ \frac{1}{\pi} \int_{\rho}^R \frac{(\arcsin b/r_1) db}{[b^2 - \rho^2]^{1/2}} \right] \quad (3.13)$$

The radius is a monotonically increasing function of the turning parameter  $\rho$  (seen by differentiation) and  $r < \rho$ . Consequently,  $\rho$  is a single-valued function of  $r$ : the index profile is physically allowed. The function  $\rho(r)$  must be monotonically increasing as well. Furthermore, the function  $n(\rho)$  is monotonically decreasing in  $\rho$  (seen by differentiation again) and, consequently,  $n$  is monotonically decreasing in  $r$ : the highest index value is the value at the origin with:

$$n_{max} = \exp \left[ \frac{2}{\pi} \int_{\rho}^R (\arcsin b/r_1) \frac{db}{b} \right] = \exp \left[ \frac{2}{\pi} \int_{\rho}^{R/r_1} (\arcsin \xi) \frac{d\xi}{x_i} \right] \quad (3.14)$$

With the help of this formula, one can compute by a simple numerical integration the required index range for the modified MFE mirror. We see that  $n_{max}$  may be arbitrarily close to 1 for sufficiently small radii  $R$ . Given the radii  $R$  and  $r_1$ , the index profile itself is easily computed by storing a table of  $(r, \rho)$  values. Here  $\rho$  ranges from 0 to  $R$  and  $r$

is numerically calculated according to formula 3.13. Then an interpolating function  $\rho$  is constructed from the calculated data and the index profile is computed as

$$\begin{cases} n = \frac{\rho(r)}{r} & 0 \leq r \leq R \\ n = 1 & r > R \end{cases} \quad (3.15)$$

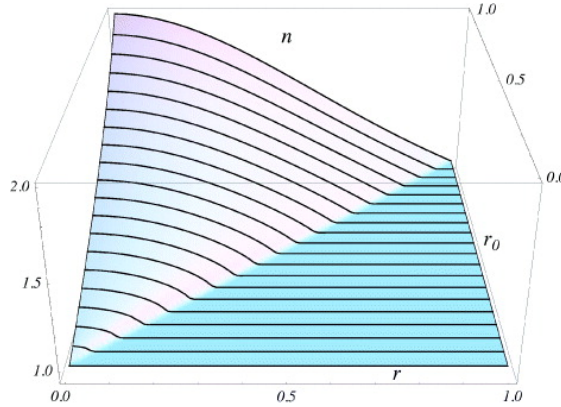


FIGURE 3.6: Index profiles  $n(r)$  for focusing media with radii  $R$  and  $r$  in units of  $r_1$ .

Figure 3.6 shows the profiles of the modified MFE mirrors depending on the ratio between the mirror radius  $r_1$  and the radius  $r_1$  of the material. They are modifications of Maxwell's profile 3.11 with  $n$  arbitrarily close to 1. We could multiply the profile by a constant  $n_1$  and still have the same functionality because the ray trajectories are unchanged. We thus find that the index contrast, the relative difference between  $n$  at the centre and  $n_1$  at the rim of the material, may be arbitrarily small.

### 3.4 Stereographic Map; Real Plane

Assume a unit 2-sphere described by the equation:

$$X^2 + Y^2 + Z^2 = 1 \quad (3.16)$$

Suppose the  $N$  – determines the north pole of the sphere – as the point of projection Figure 3.7. Then its antipodal point <sup>4</sup>,  $S$ , represents the south pole.

The stereographic projection defines as a map which project the 2-sphere into the 2-plane:

$$\mathfrak{s} : \mathbb{S}^2 \rightarrow \mathbb{R}^2 \quad (3.17)$$

---

<sup>4</sup>Antipodal of a point  $P$  on the sphere is the point which is diametrically opposite to it, which is determined by the crossing point of at least two great circles which passing through  $P$

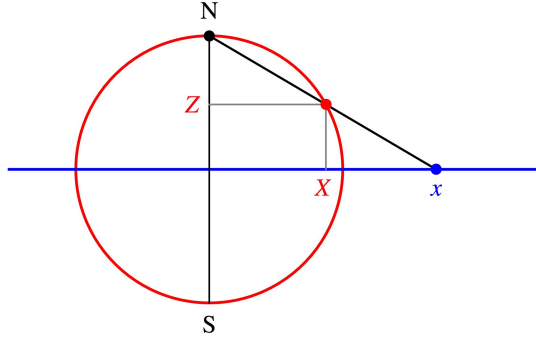


FIGURE 3.7: the point  $N$  determines the north pole of the sphere as the point of projection,  $S$  would be the south pole. The projection plane is the equator plane of the sphere.

We take the equatorial plane of the sphere as a projection plane. Each points  $P$  on the surface of the 2-sphere can be expressed as  $P[X, Y, Z]$ . The projected point  $P'$  on the plane, is result of intersecting line  $NP$  with the equatorial plane:

$$[x, y] = \left[ \frac{X}{1 - Y}, \frac{Y}{1 - Z} \right], \quad (3.18)$$

consequently, the inverse map reads as:

$$\mathfrak{s}^{-1} : \mathbb{R}^2 \rightarrow \mathbb{S}^2 \quad (3.19)$$

and

$$[X, Y, Z] = \left[ \frac{2x}{1 + x^2 + y^2}, \frac{2y}{1 + x^2 + y^2}, \frac{-1 + x^2 + y^2}{1 + x^2 + y^2} \right]. \quad (3.20)$$

There is a point on the sphere which has no well-defined image, and that is the projection point itself. Mathematically, one might say that the image of the projection point locates at infinity. Therefore we need at least two patches of maps to project the whole sphere onto the plane; once take  $N$  as the projection point and once  $S$  as the projection point. This fact has an impressing feature when expressed in the complex plane. In the real plane, we can use different formula rather than Equation 3.16 to parametrize the sphere. If we use trigonometric functions ( $\sin \theta$ ) and ( $\cos \theta$ ), by tangent half-angle substitution we ends up with an interesting results: the stereographic projection gives the following relation between the differential distance on the the sphere and on the plane:

$$\sin \theta = \frac{2t}{t^2 + 1} \quad \cos \theta = \frac{t^2 - 1}{t^2 + 1} \quad (3.21)$$

$$dx = \frac{2}{t^2 + 1} dt \quad (3.22)$$

To prove the Luneberg's interpretation it is enough to remember the formula of the optical path in the medium:

$$S = \int_{P_1}^{P_2} dl = \int_{P_1}^{P_2} n ds. \quad (3.23)$$

Stereographic projection is a conformal map, meaning that it preserves the angles at which curves cross each other. Electromagnetic equations are conformal invariant [35] it means that under Stereographic projection all properties of the light propagation will be invariant . Therefore, the optical path length should stay invariant. Comparing Equation 3.22 and Equation 3.23 we conclude:

$$n = \frac{2}{t^2 + 1} = \frac{2}{1 + r^2} \quad (3.24)$$

Which only differs up to a constant from the refractive index profile for the MFE in Equation 3.1.

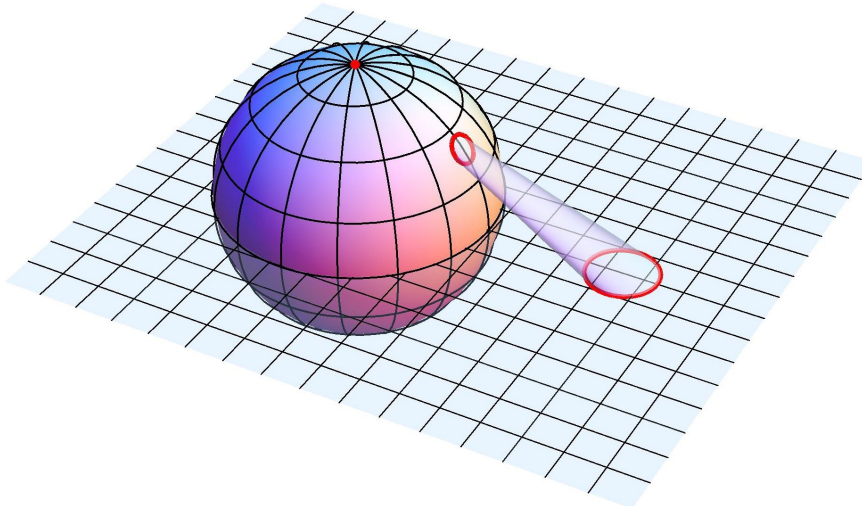


FIGURE 3.8: Stereographic map preserves the circles. Stereographic map is a conformal map it means it preserve the angles but not the area.(Credit: Ulf Leonhardt)

### 3.4.1 Stereographic Map; Complex Plane

To understand how the MFE is a stereographic projection of sphere, we need to know the properties of this map. For simplicity, we are restricting our argument to 2-dimension.<sup>5</sup> We will see that the properties of stereographic projection in complex plane help us to calculate point spread function (PSF) of the Maxwell Fisheye. In complex analysis, inversion is a map, over a field of real numbers which is defined as following:

---

<sup>5</sup> The extension to the higher dimension is possible. For a very detailed discussion and visualisation of 3-sphere stereographic map, see [35].

$$\mathcal{I}nv : \mathbb{R} \rightarrow \{\mathbb{R} - 0\} \quad \mathcal{I}nv(a) = a^{-1} = \frac{1}{a} \quad \text{for all } a \in \mathbb{R} \quad (3.25)$$

The function  $\mathcal{I}nv$  is not well-defined at point  $x = 0$ , because:

$$\mathcal{I}nv(x)|_{x=0} = \frac{1}{0} \quad (3.26)$$

The same argument is valid in the complex plane, where:

$$z = x + iy \quad x, y \in \mathbb{R} \quad (3.27)$$

As  $z$  reaches 0,  $\mathcal{I}nv_i m$  is not well define, but we know that in the limit, when  $z \rightarrow 0$ , the inversion becomes  $\mathcal{I}nv_i m = \infty$ . Therefore, if we extend the complex plane to involve the  $\infty$ , the map  $\mathcal{I}nv_i mg$  will projects the complex plan into itself and defines a homomorphism. This explanation was quite abstract, but it became interesting when Riemann finds a geometrical interpretation to it. The inversion function maps the zero point of a complex plane into infinity. The stereographic projection also maps the reference point (the projection point of the sphere) into infinity. Riemann showed that the stereographic map of the extended complex plane (complex plane +  $\infty$ ) is a sphere, later was called Riemann sphere after him. There is a one-to-one relation between all the points of a sphere and extended complex plane. The relation between the points 0 and  $\infty$  is projected to the North and South points on the Riemann sphere. But, how this argument relates to MFE: We said that Maxwell Fisheye is conformally equivalent to a sphere. On the other hand, MFE is an unbounded medium. Substituting the corresponding variables in the stereographic map equations, one finds that the inversion of the centre of MFE will locate at infinity. This resemblance suggests that we can present the MFE with the extended complex plane. The advantage of this adoption is that we know how to project the complex functions (for example wave equations) from the extended complex plane onto the Riemann sphere, which gives us a brilliant tool to waveize the MFE. In this picture, the antipodal points on the surface of the Riemann sphere resemble the source and image points in MFE medium. Meanwhile, this is equivalent to the inversion of point “zero” in an extended complex plane. The advantage of this strategy is using the symmetry group of the sphere. The relation between a pair of a source/image point on the sphere is described by rotation. This pair on the extended complex plane is represented by a Möbius transformation which is equal to an invention. In [60] we used this method to find the PSF of the MFE. We find a particular solution of the wave equation in the complex plane when the source is in the centre and the image asymptotically at infinity. This resembles a pair of source/image on the north/south poles of the sphere. Because physics is invariant under rotation of

the sphere, we can assume the solution is valid for any pair of source/image at any antipodal point. On the other hand, the stereographic map of a symmetry group of a sphere is the Möbius transformation in the complex plane. Therefore, physics must be invariant under the Möbius transformation. Therefore, to have the solution for any arbitrary points in MFE medium we just need to apply a proper Möbius transformation on our initial solution. This description was the essence of our paper [60] The Maxwell Fisheye medium is a very unique optical device which has a point spread function PSF equal to its Green's function at image locus.

### 3.4.2 Few Practical Points on the Fabrication of the MFE

The realisation of a medium with an arbitrary varying refractive index profile became possible by the advent of metamaterials, utilising subtle methods to fabricate composite media. An inhomogeneous medium like the Fisheye is approximated by finely structured layers of dielectrics. The medium is smooth enough if the dimensions of the layers are much smaller than the wavelength of the electromagnetic waves. In the MFE, the refractive index decreases from the constant value  $n_0$  in the centre of symmetry to zero at infinity. In practice, falling the refractive index much below 1 results in confinement of waves in the closed trajectories. However, as it is unphysical to extend the medium to infinity, and practically far from trivial to bring the refractive index to zero. Therefore, Leonhardt suggested cutting the medium by a mirror where the refractive index of medium matches the refractive index of the vacuum/air [16].

As the structures of the metamaterial need to be much smaller than the wavelength, fabricating the medium is much easier in the microwave range of the spectrum. For fabricating the MFE in the visible range of light, it is better to use other strategies, for example, in two-dimensions, by using planar waveguides with variable height. As the height determines the effective refractive index of light in the waveguide, the height profile generates an index profile. This method has been used at the Weizmann Institute with silicon dioxide  $SiO_2$ ,  $n = 1.4$  and silicon ( $n = 3.4$ ) to fabricate the MFE in the optical range. The relative refractive index can go from 2 in the centre down to 1 in the border where the medium is cut by a Bragg mirror made of silicon rings. The mirror turns the “half-MFE” into a full Maxwell Fish Eye suitable for perfect imaging. Gold quantum nanoparticles play the role of the sources and detectors there. However, fitting at the edge does not need to be ideal for the particular case of the MFE, because the focusing behaviour of the medium does not suffer dramatically by the lower index contrast.

### 3.4.3 Time Line in the Study of Optical Properties of the MFE

1854: The Maxwell Fisheye is described in, Cambridge and Dublin Mathematical Journal, in one number of set puzzles, in 1853. The challenge is to find the refractive index as a function of radius, given that a ray describes a circular path, and further to prove the focusing properties of the lens. The solution is given in the 1854 edition of the same journal. The problems and solutions were originally published anonymously, but the solution to this puzzle (and one other) was included in Niven's The Scientific Papers of James Clerk Maxwell, which was released eleven years after Maxwell's death<sup>6</sup>. Maxwell concludes:

“ It would require a more accurate investigation into the law of the refractive index of the different coats of the lens to test its agreement with the supposed medium. On the other hand, we find that the law of the index of refraction which would give a minimum of the aberration for a sphere of this kind placed in water, gives results not discordant with facts, so far as they can be readily ascertained.”

1944: In his book *Mathematical Theory of Optics* R. K. Luneberg gives a complete analyse of the lens including the forms of the wavefront, trajectories, optical line elements, etc. The new geometrical interpretation is introduced, and relation with a complex plane is described.

1958: Chen. T. Tai derives the Maxwell equations for MFE. In his paper on electrodynamics of Fisheye medium, Tai mentioned the lack of sufficient numerical studies, which would result in detailed analyse on wave behaviour in focusing point in the Fisheye medium [50, 51]

1971: Yu. N. Demkov et al. Consider the resemblance of the Maxwell Fisheye Medium with a potential problem as "...the hydrogen atom of optics..." They conclude that MFE is a perfect imaging device in the full wave regime.

1990: David Shafer suggested a modification on the original MFE, to make it practically realisable.

2009: Ulf Leonhard brought it back again to the community's attention by re-deriving the full Green's function solution and suggested to place a drain in the image position to completing the time-reversal symmetry.

From 2009 to 2015 vast amount of work dedicated to verifying whether Fisheye is capable of making a perfect imagine beyond the geometrical optics or not.

2015: We published a model theory which describes a crucial effect which never considered before: the internal interaction between sources and detectors. These interactions have a significant influence on the resolution of the image in the MFE.

The imaging properties of MFE in the geometrical optics are well studied and understood [7, 47, 52], however, introducing the Fisheye as a diffraction-free imaging device in full

---

<sup>6</sup>Wikipedia page: [www.wikipedia.org/wiki/Luneburg-lens](http://www.wikipedia.org/wiki/Luneburg-lens)

electromagnetic regime [16] needs a careful deliberation while there is a subtle difference between geometrical optics and wave regime when it comes to image quality. In this research, we assume to see whether MFE, which makes the perfect imaging in geometrical optics, holds its significance in the full electromagnetic regime or not.

## Chapter 4

# Electrodynamics of The Maxwell Fisheye Medium

### 4.1 Introduction

In Chapter 3 we studied the geometrical optics of the MFE. The MFE is a perfect imaging device in that regime. In this chapter, we study the MFE in wave regime to determine if its perfect imaging feature remains invariant under the transition to the wave regime. The standard Helmholtz equation, as the wave equation, is associated with the homogeneous medium, and therefore is not the full descriptive equation of wave propagation through an inhomogeneous medium like the MFE. There are two standard methods for deriving the proper form of wave equations in the MFE. First, we can consider the Fisheye as an inhomogeneous stratified dielectric in  $\mathbb{R}^N$ , through which waves travel with varying speed. Second, we can use the transformation optics interpretation for gradient refractive index profile interpreted as the curved vacuum.

Under specific conditions [35, 53], the corresponding metric of the curved vacuum can be derived from the refractive index profile. Then the wave propagation in the induced geometry can be analysed. The equivalency of the two models is discussed in various studies [34, 53, 54]. Nevertheless, recognising the equivalent geometry in a general case is far from trivial. Fortunately, for a few highly symmetrical gradient lenses including MFE, the geometry is known from geometrical optics. n-dimensional MFE medium performs a geometry of n-dimensional hypersphere [47]. The connecting map between manifolds is a stereographic projection which projects the  $\mathbb{R}^n$  to  $\mathbb{S}_a^n$ , the equivalency being a valid base on electrodynamics conformal invariance.

To solve any electrodynamic problem, we need to decouple the field equations and boundary conditions into independent scalar functions. The methods used for any particular problem depends on physical the symmetries of the medium and the geometrical symmetries of the boundary conditions. In the following, we study both approaches for

deriving the decoupled scalar functions in the Maxwell Fisheye problem. Our first approach is based on Debye's potentials while for the second approach we need to develop modified Debye potentials. In a medium such as the MFE, wave propagation has its most compact and comprehensive expression in the forms of dyadic Green's functions. Dyadic Green's functions are bitensorial functions rather than conventional vector functions. The additional information that they carry is the source's spatial orientation. We will see that the polarisation of the source has effect on the formation of the image. In this chapter we deriving the Green's function of the Maxwell Fisheye medium.

Remember that the Fisheye is an inhomogeneous medium with a radially symmetric refractive index profile as:

$$n(\mathbf{r}) = \frac{2n_0 a^2}{a^2 + r^2} \quad (4.1)$$

where  $a$  is the characteristic length associated with the stereographic projection and  $n_0$  is a constant denotes the refractive index in the centre of the MFE: as  $r$  increases the refractive index decreases.

## 4.2 Electrodynamics of Inhomogeneous Media

Optical inhomogeneity of the medium presents itself as a position dependency of the elements of the electric and magnetic response functions  $\mu(r)$  and  $\epsilon(r)$ . In the most general expression, electric permittivity  $\bar{\epsilon}(r)$  and magnetic permeability  $\bar{\mu}(r)$  are tensorial quantities. Maxwell's equations in their general form in  $\mathbb{R}^3$  are written:

$$\begin{aligned} \nabla \times \mathbf{E}(\mathbf{r}, t) &= -\frac{\partial}{\partial t} \bar{\mu}(r) H(\mathbf{r}, t) - \mathbf{M}(\mathbf{r}, t) \\ \nabla \times \mathbf{H}(\mathbf{r}, t) &= \frac{\partial}{\partial t} \bar{\epsilon}(r) E(\mathbf{r}, t) + \mathbf{J}(\mathbf{r}, t) \end{aligned} \quad (4.2)$$

For an isotropic inhomogeneous medium like the MFE,  $\bar{\epsilon}(r)$  and  $\bar{\mu}(r)$  reduce to functions of position, though not commutative with the  $\nabla$  operator. Thus, for time harmonic fields the wave equations become:

$$\begin{aligned} \nabla \times \mu^{-1} \nabla \times \mathbf{E}(\mathbf{r}) - \omega^2 \epsilon \mathbf{E}(\mathbf{r}) &= \imath \omega \mathbf{J}(\mathbf{r}) - \nabla \times \mu^{-1} \mathbf{M}(\mathbf{r}) \\ \nabla \times \epsilon^{-1} \nabla \times \mathbf{H}(\mathbf{r}) - \omega^2 \mu \mathbf{H}(\mathbf{r}) &= \imath \omega \mathbf{M}(\mathbf{r}) + \nabla \times \epsilon^{-1} \mathbf{J}(\mathbf{r}) \end{aligned} \quad (4.3)$$

Each of these two vector wave equations is self-contained: therefore, either is sufficient

to describe the complete behaviour of the system. Most natural material, are non-magnetic; their  $\mu$  hardly deviates from the vacuum permeability, which results in an insignificant magnetic response in the dielectric. Therefore, they are usually of only theoretical interest. Because of inhomogeneity of the medium,  $\epsilon^{-1}$  and  $\mu^{-1}$  are not commutative with the operator  $\nabla$ . Therefore, applying the Lagrange formula for  $\nabla$  is not trivial. Later we will see that the non-commutability of  $\epsilon$  and  $\mu$  with derivative operators has a crucial impact on the general forms of the equations.

On the other hand, the dependence of the electric and magnetic fields  $\mathbf{E}(\mathbf{r})$  and  $\mathbf{H}(\mathbf{r})$  on the source function and especially its curl derivative is apparent. For instance, in [51] the advantage of polarisation dependency is used to ease the complexities. In analysing image quality, the significance of the dyadic Green's functions come to the place with the utility to connect the field's property with the source features in its most complete details, including all possible dipole polarisations for sources. The dyadic Green's function of the optical system permits the electric or magnetic field to be derived in its most complete form:

$$\mathbf{E}(\mathbf{r}) = \int_V \bar{\mathcal{G}} \cdot (\mathbf{r}, \mathbf{r}') \mathbf{J}(\mathbf{r}') d\mathbf{r}' \quad (4.4)$$

where  $\mathbf{J}(\mathbf{r})$  denotes the source distribution and  $\bar{\mathcal{G}}$  the dyadic Green's function. The main purpose of this study is to analyse the behaviour of the MFE dyadic Green's functions at their singularities, the source and drain ports. Before that, we derive and analyse these functions in detail. To find the general solutions of Equation 4.3, we need to find the Green's function that satisfies Equation 4.4.

According to [51], the Green's function for harmonic fields needs to follow the vector wave equation:

$$\begin{aligned} \nabla \times \frac{1}{\mu} \nabla \times \mathcal{G}(\mathbf{r}) - \omega^2 \epsilon \mathcal{G}(\mathbf{r}) &= i\omega \delta(\mathbf{r}) \mathbb{I} \\ \nabla \times \frac{1}{\epsilon} \nabla \times \mathcal{H}(\mathbf{r}) - \omega^2 \mu \mathcal{H}(\mathbf{r}) &= \nabla \times \frac{1}{\epsilon} \delta(\mathbf{r}) \mathbb{I} \end{aligned} \quad (4.5)$$

To find the bitensors  $\mathcal{G}(\mathbf{r})$  and  $\mathcal{H}(\mathbf{r})$ , we need the solutions for the homogeneous equation.

$$\nabla \times \frac{1}{\mu(\mathbf{r})} \nabla \times \mathcal{G}(\mathbf{r}) - \epsilon(\mathbf{r}) \omega^2 \mathcal{G}(\mathbf{r}) = 0 \quad (4.6)$$

$$\nabla \times \frac{1}{\epsilon(\mathbf{r})} \nabla \times \mathcal{H}(\mathbf{r}) - \mu(\mathbf{r}) \omega^2 \mathcal{H}(\mathbf{r}) = 0 \quad (4.7)$$

There is no known method to solve Equations 4.6 and 4.7 for the general inhomogeneous refractive index profile with three altering spatial variables, but fortunately for radially

symmetric inhomogeneity,  $n = n(\mathbf{r}) = \sqrt{\mu(\mathbf{r})\epsilon(\mathbf{r})}$ , we can systematically solve equations for various boundary conditions. In other words, we may find the eigenfunction expansion pertaining to the geometrical symmetry of the lens.

#### 4.2.1 Inhomogeneous Media with Radial Symmetry

For a radially symmetric inhomogeneous medium, it is the most convenient to decompose the EM field into transverse components TE to  $r$  and TM to  $r$  modes. Solutions of equation 4.6 have their representation in terms of the Debye potentials  $\pi_e$  and  $\pi_m$  [51]:

$$\begin{aligned}\mathcal{G}^{te} &= \nabla \times (\mathbf{r}\pi_m) \\ \mathcal{G}^{tm} &= \frac{1}{\omega\epsilon(\mathbf{r})}\nabla \times \nabla \times (\mathbf{r}\pi_e).\end{aligned}\tag{4.8}$$

Thus we have one solution for transverse electrical modes and one solution for transverse magnetic modes. Similarly for equation Equation 4.7 we have:

$$\begin{aligned}\mathcal{H}^{tm} &= \nabla \times (\pi_e \mathbf{r}) \\ \mathcal{H}^{te} &= \frac{1}{\omega\mu(\mathbf{r})}\nabla \times \nabla \times (\pi_m \mathbf{r})\end{aligned}\tag{4.9}$$

As usual, any general solution might be written as a linear combination of the two modes.

$$\mathcal{G} = \nabla \times (\mathbf{r}\pi_m) - \frac{1}{\omega\epsilon(\mathbf{r})}\nabla \times \nabla \times (\mathbf{r}\pi_e).\tag{4.10}$$

$$\mathcal{H} = \nabla \times (\pi_e \mathbf{r}) + \frac{1}{\omega\mu(\mathbf{r})}\nabla \times \nabla \times (\pi_m \mathbf{r})\tag{4.11}$$

$\pi_e$  and  $\pi_m$  generate scalar functions known as the Debye potentials, which are purely radial.

They themselves need to satisfy the following wave equations:

$$\begin{aligned}\left(\nabla^2 - \frac{1}{\mu(\mathbf{r})}\frac{\partial}{\partial r}\mu(\mathbf{r})\frac{\partial}{\partial r} + \omega^2\epsilon(\mathbf{r})\right)\pi_e &= 0 \\ \left(\nabla^2 - \frac{1}{\epsilon(\mathbf{r})}\frac{\partial}{\partial r}\epsilon(\mathbf{r})\frac{\partial}{\partial r} + \omega^2\mu(\mathbf{r})\right)\pi_m &= 0\end{aligned}\tag{4.12}$$

Here one may easily recognise the geometrical feature. The position dependency of  $\epsilon(\mathbf{r})$  and  $\mu(\mathbf{r})$  induce an extra term in the Helmholtz-like equation for each of the transversal modes, the final expression of the equations depending on the spatial permittivity and permeability distributions and their spatial derivative.

Transverse magnetic modes tie to the extra term due to the derivative of  $\mu(\mathbf{r})$ :

$$\begin{aligned}\mathcal{G}^{tm} &= \nabla \times (\pi_e \mathbf{r}) \\ \mathcal{H}^{tm} &= \frac{1}{\omega \mu(\mathbf{r})} \nabla \times \nabla \times (\pi_e \mathbf{r}).\end{aligned}\tag{4.13}$$

And transverse electric modes tie to the extra term due to the derivative of  $\epsilon(\mathbf{r})$ :

$$\begin{aligned}\mathcal{G}^{te} &= \nabla \times (\pi_m \mathbf{r}) \\ \mathcal{H}^{te} &= \frac{1}{\omega \epsilon(\mathbf{r})} \nabla \times \nabla \times (\pi_m \mathbf{r})\end{aligned}\tag{4.14}$$

If either of the medium functions  $\epsilon(\mathbf{r})$  and  $\mu(\mathbf{r})$

$$\eta_i(\mathbf{r}) = \begin{cases} \epsilon(\mathbf{r}) & i = 1 \\ \mu(\mathbf{r}) & i = 2 \end{cases}\tag{4.15}$$

be constant ,  $\eta_i(\mathbf{r}) = \text{const. } i = 1 \vee 2$ , then the corresponding equation 4.12 of the counterpart transverse mode's potential

$$\pi_i = \begin{cases} \pi_e & i = 1 \\ \pi_m & i = 2 \end{cases}\tag{4.16}$$

reduces to the Helmholtz-like equation

$$[\nabla^2 + \omega^2 \eta_j(\mathbf{r})] \pi_j = 0 \quad \eta_i(\mathbf{r}) = \text{const. } i, j = 1, 2, \quad j \neq i\tag{4.17}$$

We refer to Equation 4.17 as Helmholtz-like because designation of Helmholtz equation usually reserves for a homogeneous medium. In an inhomogeneous medium, if either of  $\epsilon(\mathbf{r})$  or  $\mu(\mathbf{r})$  becomes constant, the other is yet position dependent. In such cases, the extra term in 4.17 related to the derivative of  $\eta_i(\mathbf{r})$  vanishes while the non-derivative term related to  $\eta_j(\mathbf{r})$  retains the position dependency.

In conclusion, inhomogeneity has two influences on the wave equation, one appears as an extra term associated with the covariant derivative that changes the Laplace operator,

and the other one associated with the spatial variation of speed. In each equation, these two effects are due to different medium functions. By keeping one of the medium's functions constant and the other variable in space

$$\eta_i(\mathbf{r}) = \begin{cases} \text{Const.} & i = 1 \vee 2 \\ \eta_j(\mathbf{r}) & j = 1, 2, j \neq i \end{cases} \quad (4.18)$$

We would end up with a pair of equations:

$$\begin{aligned} (\nabla^2 + \omega^2 \eta_j(\mathbf{r})) \pi_j &= 0 \\ \left( \nabla^2 - \frac{1}{r \eta_j(\mathbf{r})} \frac{\partial}{\partial r} \eta_j(\mathbf{r}) \frac{\partial}{\partial r} r + \omega^2 \right) \pi_i &= 0 \quad i, j = 1, 2, j \neq i. \end{aligned} \quad (4.19)$$

As previously mentioned, in most practical cases relative permeability is so insignificant that it can be taken as unity,  $\mu = 1$ , and  $\epsilon(\mathbf{r}) = n^2(\mathbf{r})$ ; so Equation 4.19 for the MFE has a explicit form of:

$$\begin{aligned} (\nabla^2 + \omega^2 n^2(\mathbf{r})) \pi_e &= 0 \\ \left( \nabla^2 - \frac{1}{r n^2(\mathbf{r})} \frac{\partial}{\partial r} n^2(\mathbf{r}) \frac{\partial}{\partial r} r + \omega^2 \right) \pi_m &= 0 \end{aligned} \quad n(\mathbf{r}) = \frac{2n_0 a^2}{a^2 + r^2} \quad (4.20)$$

Which is a wave equation for the scalar potential; but each potential ( $\pi_m$  and  $\pi_e$ ) is associated with a particular transversal mode. Unless the source is polarised in one transverse mode, the MFE would have two different scalar potentials from two different equations, which EM fields have to be obtained from.

The choice of appropriate potential is a matter of confusion in the literature devoted to the topic. Scholars usually use only one of Equation 4.20 equations for the MFE. Demkov [48], Benitez [55], Szmytkowski, [56, 57] and Pazynin [58], adopt the following equation:

$$(\nabla^2 + \omega^2 \epsilon(\mathbf{r})) \pi_e = 0. \quad (4.21)$$

But, Leonhardt et. al. [59, 60] adopted:

$$\left( \nabla^2 - \frac{1}{r \epsilon(\mathbf{r})} \frac{\partial}{\partial r} \epsilon(\mathbf{r}) \frac{\partial}{\partial r} r + \omega^2 \right) \pi_m = 0 \quad (4.22)$$

The best results appear if one applies the impedance-match condition [59].

$$\mu^{ij} = \epsilon^{ij} = n = \sqrt{g} g^{ij} \quad (4.23)$$

Thus, the electric and magnetic response of the system would be similar. Impedance-matching is a strong condition that only is only conceivable with meta-materials. Two equations of 4.17 reduce to one for both modes, if the electric and magnetic responses of the medium are equated:

$$\left( \nabla^2 - \frac{1}{rn(\mathbf{r})} \frac{\partial}{\partial r} n(\mathbf{r}) \frac{\partial}{\partial r} r + \omega^2 n(\mathbf{r}) \right) \begin{pmatrix} \pi_e \\ \pi_m \end{pmatrix} = 0 \quad (4.24)$$

Both the TE and TM modes are given by the same scalar Debye potential. Consequently as condition 4.23 is held Equation 4.24 in spherical coordinates becomes:

$$\left( \frac{\partial^2}{\partial r^2} + \frac{2}{r} \frac{\partial}{\partial r} - \frac{1}{n} \frac{\partial n}{\partial r} \frac{\partial}{\partial r} + \frac{1}{r^2} \Delta_{S^2} + \omega^2 n \right) \begin{pmatrix} \pi_e \\ \pi_m \end{pmatrix} = 0 \quad (4.25)$$

This scalar generating function is equivalent to the scalar Green's function  $D$  in [59] and [60]. The advantage of the impedance-matching condition is that it provides a clear geometrical meaning to the equations. Equation 4.25 has a extra term with respect to the Helmholtz equation in spherical coordinates. Impedance-matching allows us to read this equation in curvilinear coordinates.

Assuming

$$g_{ij} = n^2 \text{diag}(1, r^2, r^2 \sin^2 \theta)$$

$$g^{ij} = \frac{1}{n^2} \text{diag} \left( 1, \frac{1}{r^2}, \frac{1}{r^2 \sin^2 \theta} \right) \quad (4.26)$$

$$g = n^6 r^4 \sin^2 \theta$$

Equation 4.25 is in the form:

$$\left( \frac{1}{\sqrt{g}} \partial_j \sqrt{g} g^{ij} \partial_i + \omega^2 \right) \begin{pmatrix} \pi_e \\ \pi_m \end{pmatrix} = 0 \quad (4.27)$$

Resembling the wave equation in a curved vacuum. The Fisheye medium vanishes and the curvilinear remains. In the next section we will come back to this in details. In impedance-matching conditions the TEM waves show the same behaviour. In the non impedance-match conditions with a proper polarisation-tuning, it is possible to avoid the complexities and restrict the propagation only in one of TE to TM modes, as mentioned

for the two 2-D medium in [35]. However, we need to study both cases. For simplicity we are looking in the case when  $\mu(\mathbf{r}) = 1$  because manufacturing the electrical permittivity is more doable for the sake of practical reason. Thus, derivatives of the TE mode will not be affected by the inhomogeneity of  $\epsilon(\mathbf{r}) = n^2(\mathbf{r})$ ,

$$(\nabla^2 + \omega^2 \epsilon(\mathbf{r})) \pi_e = 0 \quad (4.28)$$

while a variation of  $\epsilon(\mathbf{r})$  induces the geometry on the TM modes:

$$\left( \nabla^2 - \frac{1}{\epsilon(\mathbf{r})} \frac{\partial}{\partial r} \epsilon(\mathbf{r}) \frac{\partial}{\partial r} + \omega^2 \right) \pi_m = 0 \quad (4.29)$$

In the following we analyse both Equations 4.28 and 4.29 in the MFE profile.

#### 4.2.2 Analysing the Debye potential in an N-Dimensional MFE

##### 4.2.2.1 The TE Mode in the Non-Magnetic Medium

For the sake of theoretical interests, we representing the equations in  $N$  dimension, as in [57]: it might help us see the dependency of imaging properties with dimension of the device. For the transverse electric mode in  $N$ -dimensions, the MFE requires the solution of Helmholtz-like equation<sup>1</sup>:

$$\left( \nabla^2 + \omega^2 \frac{4n_0^2 a^4}{(a^2 + r^2)^2} \right) \pi_e(\mathbf{r}, \mathbf{r}') = 0 \quad (4.30)$$

The right hand side of equation, vanishes everywhere, except at the points of source  $\mathbf{r} = \mathbf{r}'$  and image  $\mathbf{r} = \infty$ . At singularities we expect the divergence of the Debye potentials to be:

$$\pi_e(\mathbf{r}, \mathbf{r}') \xrightarrow{\mathbf{r} \rightarrow \mathbf{r}'} \frac{C_s}{|\mathbf{r} - \mathbf{r}'|} \quad N \geq 3$$

$$\pi_e(\mathbf{r}, \mathbf{r}') \xrightarrow{\mathbf{r} \rightarrow \infty} \frac{C_d}{|\mathbf{r}|} \quad N \geq 3 \quad (4.31)$$

and

$$\pi_e(\mathbf{r}, \mathbf{r}') \xrightarrow{\mathbf{r} \rightarrow \mathbf{r}'} \frac{1}{2\pi} \ln |\mathbf{r} - \mathbf{r}'| \quad N = 2$$

$$\pi_e(\mathbf{r}, \mathbf{r}') \xrightarrow{\mathbf{r} \rightarrow \infty} C_d \ln |\mathbf{r}| \quad N = 2 \quad (4.32)$$

---

<sup>1</sup>TE mode in  $N$ -dimensional Fisheye means that magnetic field is perpendicular to the  $(N-1)$ -dimensional manifold of propagation.

From normalisation conditions:

$$C_s = \frac{1}{(N-2) \mathbb{S}_{N-1}}, \quad (4.33)$$

where  $\mathbb{S}_{N-1}$  denotes the surface area of unit ( $N-1$ ) dimension Sphere. For the image point, we need to calculate the  $C_d$  under exact boundary conditions. The form of  $C_d$  includes the imaging behavioural of the MFE.

For simplicity we first assume the source is located at the centre of symmetry  $\mathbf{r}' = 0$ . Then Laplace equation has the simplest form in spherical coordinate:

$$\left( \frac{\partial^2}{\partial r^2} + \frac{N-1}{r} \frac{\partial}{\partial r} + \frac{1}{r^2} \Delta_{\mathbb{S}^{n-1}} + \omega^2 \frac{4n_0^2 a^4}{(a^2 + r^2)^2} \right) \pi_e(\mathbf{r}, 0) = 0 \quad (4.34)$$

$\Delta_{\mathbb{S}^{n-1}}$  is the Laplace-Beltrame operator on the unit sphere of  $S^{n-1}$  responsible for the angular part of the Laplacian operator. Separation of variables leads to general forms of the eigenfunctions:

$$\pi_e(\mathbf{r}) = \frac{1}{r} D_l^e(\omega r) Y_l^m \quad (4.35)$$

while the radial part satisfies the differential equation:

$$\left( \frac{\partial^2}{\partial r^2} + \frac{N-1}{r} \frac{\partial}{\partial r} + \omega^2 \frac{4n_0^2 a^4}{(a^2 + r^2)^2} - \frac{l(l+1)}{r^2} \right) D^e(r) = 0 \quad (4.36)$$

In all original works that devoted to the wavization of MFE medium, Equation 4.36 is solved only for  $l = 0$  [16, 56, 57]. However, we believe to have a perspective on the extreme behaviour of fields at singularities we need to keep the last term. As we can see  $l$  is related to the index of spherical harmonics. The final term relates to fractional order Bessel functions. This means that by omitting orders higher than  $l = 0$  we have the solution only for the zeroth order. We believe that the behaviour of waves at the focal point of the system closely relates to these higher order functions.  $l = 0$  only describes an ideal point source, while in reality there is no point source as ideal as delta function. All the physical entities have some internal structure. Therefore for a realistic system it is crucial to consider the higher order solutions in the vicinity of image point.

To simplify equation 4.36 further, we define the variable  $\nu$  as:

$$\nu = \frac{-1 + \sqrt{1 + 4\omega^2 n_0^2 a^2}}{2} \quad (4.37)$$

The equation thus become:

$$\left( \frac{\partial^2}{\partial r^2} + \frac{N-1}{r} \frac{\partial}{\partial r} + \frac{4\nu(\nu+1)a^2}{(a^2+r^2)^2} - \frac{l(l+1)}{r^2} \right) D^e = 0 \quad (4.38)$$

For  $l=0$  as discussed in most studies [16, 48, 51, 56] a simple change of variables results in the associated Legendre function. However, in our case the most general form of the solutions appears in terms of hypergeometric functions.

$$D_{l,\nu}^e = \mathcal{A} \left( \frac{a}{r} \right)^{l+1} {}_2F_1(1/4(-1-2l-\gamma), 1/4(-1-2l+\gamma), \frac{3}{2}+l; -\frac{r^2}{a^2}) + \\ \mathcal{B} \left( \frac{r}{a} \right)^l {}_2F_1(1/4(1+2l-\gamma), 1/4(1+2l+\gamma), \frac{1}{2}-l; -\frac{r^2}{a^2}) \quad (4.39)$$

in which

$$\gamma = \sqrt{1 + 4l(l+1) - 16a^2\nu(\nu+1)} \quad (4.40)$$

For  $l=0$  Equation 4.39 reduces to:

$$\gamma = \sqrt{1 - 16a^2\nu(\nu+1)} \\ D_{0,\nu}^e = \mathcal{A} \left( \frac{a}{r} \right) {}_2F_1(1/4(-1-\gamma), 1/4(-1+\gamma), \frac{3}{2}; -\frac{r^2}{a^2}) + \\ \mathcal{B} {}_2F_1(1/4(1-\gamma), 1/4(1+\gamma), \frac{1}{2}; -\frac{r^2}{a^2}) \quad (4.41)$$

By applying the boundary condition it is easy to find coefficients  $\mathcal{A}$  and  $\mathcal{B}$ .

#### 4.2.2.2 TM Mode in Non-Magnetic Medium

We have seen that the electrical mode denoted as the transverse magnetic TM would be fundamentally influenced by any inhomogeneity in  $\epsilon(\mathbf{r})$ . The equation governing the propagation of this mode is:

$$\left( \nabla^2 - \frac{1}{r \epsilon(\mathbf{r})} \frac{\partial}{\partial r} \epsilon(\mathbf{r}) \frac{\partial}{\partial r} r + \omega^2 \right) \pi_m(\mathbf{r}, 0) = 0 \quad (4.42)$$

As in the previous subsection, we assume the source is located in the centre of radial symmetry. Equation 4.42 in spherical coordinates is:

$$\left( \frac{\epsilon(\mathbf{r})}{r} \frac{\partial}{\partial r} \frac{1}{\epsilon(\mathbf{r})} \frac{\partial}{\partial r} r + \frac{1}{r^2} \Delta_{S^{n-1}} + \omega^2 \right) \pi_m(\mathbf{r}, 0) = 0 \quad (4.43)$$

Consequently the separation of variables gives:

$$\pi_e(\mathbf{r}) = \frac{1}{r} D_l^m(\omega r) Y_l^m \quad (4.44)$$

while the radial part satisfies this further differential equation for the electrical modes:

$$\left( \frac{1}{r} \frac{\partial}{\partial r} \frac{1}{\epsilon(\mathbf{r})} \frac{\partial}{\partial r} r + \omega^2 - \frac{l(l+1)}{r^2} \right) D_l^m = 0 \quad (4.45)$$

#### 4.2.2.3 Impedance-Matched MFE

If we are in an inhomogeneous medium with a constant permeability  $\mu(\mathbf{r}) = 1$ , then Equation 4.43 becomes  $\epsilon(\mathbf{r}) = n^2(\mathbf{r})$ , but not if we are in the impedance matched regime  $\epsilon(\mathbf{r}) = n(\mathbf{r})$ . This results in different equations in the [51, 61] compare to [59] as follows. For the TM mode in  $\mu(\mathbf{r}) = 1$ , equation 4.43 is:

$$\left( \frac{1}{n^2} \frac{\partial^2}{\partial r^2} + \left( \frac{1}{n^2 r} - \frac{2}{n^3} \frac{\partial n}{\partial r} \right) \frac{\partial}{\partial r} + \omega^2 - \frac{2}{n^3 r} \frac{\partial n}{\partial r} - \frac{l(l+1)}{r^2} \right) D^m = 0. \quad (4.46)$$

And for  $\mu(\mathbf{r}) = \epsilon(\mathbf{r}) = n(\mathbf{r})$ :

$$\left( \frac{1}{n} \frac{\partial^2}{\partial r^2} + \left( \frac{2}{nr} - \frac{1}{n^2} \frac{\partial n}{\partial r} \right) \frac{\partial}{\partial r} + \omega^2 - \frac{1}{n r} \frac{\partial n}{\partial r} - \frac{l(l+1)}{r^2} \right) D^m = 0. \quad (4.47)$$

The equations derived for the scalar Green's function in [60] and [59] by Leonhardt et.al. are a specific form of Equation 4.47 with some additional assumptions to simplify the equation. For the Fisheye profile adopted in [59], equation Equation 4.47 is:

$$\left( \frac{1}{n^2 r^2} (\partial_r n r^2 \partial_r) + \omega^2 - 1 - \frac{l(l+1)}{r^2} \right) D^m = 0 \quad (4.48)$$

To summarise, we have found three different forms of equation for the MFE. Numerics confirm that all three Equations 4.46, 4.47, and 4.48 have solutions in terms of hypergeometric functions and for  $l = 0$ . In all literature on the waveization of MFE, the solution reduces to associated Legendre functions. To determine the possibility of perfect imaging by any of equations we need to compare their solutions of this three kind at focusing points. Scholars do not seem to agree regarding whether any of these equations correctly describe the system. Authors in [51] adopted Equation 4.46, and those of [61] Equation 4.47. In papers[59, 60] we used the Equation 4.48, but only for the special case of  $l = 0$ .

### 4.3 The MFE as a Curved Space

A consequence of the optico-mechanical analogy is that curvature in space-time might in theory be nullified by substituting particular media when only electrodynamic fields are considered. Nobel lecturer Igor Tamm<sup>2</sup>. In this picture vacuum as in Maxwell's equations in curved space-time might be interpreted as an effective medium in flat space-time [34, 35]. Metrical structure of space-time appears as "material equations" for electrodynamic fields [62]. This fact can be used for applicational purposes [34]. Targeting the particular property of EM fields (light) in specific curved space-time, the problem will reduce to finding an effective medium that projects the properties of initial space-time. The inverse process might be applicable in practice vice versa - having the material equation building up the metrical structure that EM fields may experience. The theoretical key point in phenomena is electrodynamics' conformal invariant which allows a kind of equivalency between the space-time with the conformal relations.

$$g'_{ij} = \Omega^2(x^i)g_{ij} \quad (4.49)$$

In 2D the equivalent picture on  $\mathbb{S}^2$  is a source implanted on the surface, and waves emerging from a point source are propagating in all directions totally confined on the surface of the sphere. They cross again in the same point or at the antipodal point in the closed loops. In general, if we can let aside some topological concerns regarding the locality of conformal flatness of  $\mathbb{S}^3$ , we may assume the n-dimensional Fisheye medium being a conformal n-sphere geometry [35, 54]. This would let us to attend the waveization of Fisheye problem in the elegant way. The method here is similar to the previous chapter, where we found the proper Debye potentials for inhomogeneous media. In this section we are finding the modified Debye potentials for the equivalent curved vacuum. Spherical potential in physics received a special attention because of their fundamental importance. Specially in gravity spherical symmetric gravitational fields are an important family of problems. Any corresponding curved space-time may represent in spherical coordinate with a metric:

$$ds^2 = g_{00} dt^2 - g_{11} dr^2 - \lambda^2(d\theta^2 + \sin^2\theta d\phi^2)g_{11}, \lambda \quad (4.50)$$

The  $g_{11}$  and  $\lambda$  are positive functions of coordinate. We might be interested to investigate the electrodynamics fields in such a curved space-time. A curved space can be filled with a medium or just be a curved vacuum. Maxwell equations are well studied in such space-times.

Spherical symmetry raises the expectation that decoupling of fields to the transverse modes may result in Debye-like scalar potentials as discussed earlier in this chapter.

---

<sup>2</sup>I Y Tamm 1924, J. Russ. Phys.-Chem. Soc. **56** 248 in Russian

Actually Mo and Papas in [63] showed that apart from a modification this is the case. For a space time filled with medium characterised by  $\epsilon = \epsilon(\mathbf{r})$  and  $\mu = \mu(\mathbf{r})$  Hertz vectors

$$\begin{pmatrix} \lambda r \pi_m \\ \lambda r \pi_e \end{pmatrix} \quad (4.51)$$

can generate the solution of wave equations. Accepting this, we can derive:

$$\begin{aligned} \begin{pmatrix} \epsilon \\ \mu \end{pmatrix} \frac{\partial}{\partial r} \left[ \left( \frac{g_{00}}{g_{11}} \right)^{1/2} \begin{pmatrix} \frac{1}{\epsilon} \\ \frac{1}{\mu} \end{pmatrix} \frac{\partial}{\partial r} \begin{pmatrix} \lambda r \pi_m \\ \lambda r \pi_e \end{pmatrix} \right] + \frac{(g_{00}g_{11})^{1/2}}{\lambda \sin \theta} \left( \frac{\partial}{\partial \theta} \sin \theta \frac{1}{\partial \theta} + \frac{1}{\sin \theta} \frac{\partial^2}{\partial \phi^2} \right) \begin{pmatrix} \pi_m \\ \pi_e \end{pmatrix} \\ - \begin{pmatrix} \epsilon \\ \mu \end{pmatrix} \frac{\partial}{\partial t} \left[ \left( \frac{g_{11}}{g_{00}} \right)^{1/2} \begin{pmatrix} \epsilon \\ \mu \end{pmatrix} \frac{\partial}{\partial t} \begin{pmatrix} \lambda r \pi_m \\ \lambda r \pi_e \end{pmatrix} \right] = 0 \end{aligned} \quad (4.52)$$

Boundary conditions at any radial discontinuity  $r = a$  are decoupling which has to be verified by the particular features of the problem:

$$\begin{aligned} \left[ \frac{1}{\epsilon} \frac{\partial}{\partial r} \lambda \pi_m \right] = 0, \quad [\pi_m] = 0 \\ [\pi_e] = 0, \quad \left[ \frac{1}{\epsilon} \frac{\partial}{\partial r} \lambda \pi_e \right] = 0 \end{aligned} \quad (4.53)$$

In the following we apply above method to Fisheye medium. For that we are adopting the transformation optical statement.

**Corollary:** For any medium with time-independent but arbitrarily space-dependent refractive index given on part of  $\mathbb{R}^3$  there is a regular conformally stationary space-time vacuum and a separable 3-dimensional spatial metric. Light rays of which behave as light rays in the medium according to conventional optics [53]

As we discussed in general case it is not trivial to find the corresponding space-time or equivalently spatial metric but in Fisheye we already know the vacuum. A hypersphere  $\mathbb{S}^3$  for 3-dimensional medium.

Any 3-sphere in  $\mathbb{R}^4$  with radius  $a$  centred at origin has a characteristic equation in Cartesian coordinate:

$$X^2 + Y^2 + Z^2 + W^2 = a^2 \quad (4.54)$$

The stereographic map through the relations

$$x = \frac{X}{1 - W/a}, \quad y = \frac{Y}{1 - W/a}, \quad z = \frac{Z}{1 - W/a}, \quad (4.55)$$

transforms this 3-d curved manifold to a 3-d conformally flat geometrical object called conformal sphere.

$$x^2 + y^2 + z^2 = r^2 \quad (4.56)$$

We may see the best metric expression for them in the hyper-spherical coordinates  $(\varkappa, \theta, \phi)$  that connect to Cartesian coordinate via the following relations:

$$\begin{aligned} X &= a \sin \varkappa \sin \theta \cos \phi, & Y &= a \sin \varkappa \sin \theta \sin \phi & Z &= a \sin \varkappa \cos \theta & W &= a \cos \varkappa \\ 0 \leq \varkappa &\leq \pi, & 0 \leq \theta &\leq \pi, & 0 \leq \phi &\leq 2\pi, \end{aligned} \quad (4.57)$$

The line elements of  $\mathbb{S}^3$  in hyper-spherical coordinates:

$$ds^2 = a^2 [d\varkappa^2 + \sin^2 \varkappa (d\theta^2 + \sin^2 \theta d\phi^2)] \quad (4.58)$$

By the stereographic map would transform to the line elements of conformal sphere counterpart:

$$ds^2 = n^2 [dr^2 + r^2(d\theta^2 + \sin^2 \theta d\phi^2)] \quad (4.59)$$

This is a proper coordinate in which  $\mathbb{S}^3$  has a conformally flat equivalence metric.

$n(r)$  would be equal to:

$$n = \frac{2}{1 + r^2/a^2} \quad (4.60)$$

According to definitions, Equation 4.59 is a conformally flat space as it defer from Euclidian metric by a factor  $n(r)^2$ .

We restrict ourself to the special case:

$$\mu = \epsilon = n(r)$$

Therefore:

$$g_{ij} = n^2 \delta_{ij}, \quad g^{ij} = \frac{1}{n^2} \delta^{ij}, \quad g = n^6 \quad (4.61)$$

Comparing the metric Equation 4.52 and Equation 4.59 we may recognise that by substituting the following paramours both metric will have the same forms<sup>3</sup>.

$$\begin{aligned} \lambda &\longrightarrow rn \\ -g_{11} &\longrightarrow n^2 \\ g_{00} &\longrightarrow -1 \end{aligned}$$

---

<sup>3</sup>Please refer to [53], example A.4.

Helmholtz equation in Fisheye medium becomes equal to curved vacuum with covariant derivatives:

$$\left( \nabla^2 + \frac{\omega^2}{c^2} \right) \psi_\omega(\mathbf{r}) = \left( \frac{1}{\sqrt{g}} \partial_j \sqrt{g} g^{ij} \partial_i + \frac{\omega^2}{c^2} \right) \psi_\omega(\mathbf{r}) = 0 \quad (4.62)$$

Laplace operator  $\nabla$  does not necessary has a standard form, hence it is needed to indicate explicitly according to metric. Respectively in spherical coordinate:

$$g_{ij} = n^2 \text{diag}(1, r^2, r^2 \sin^2 \theta)$$

$$g^{ij} = \frac{1}{n^2} \text{diag} \left( 1, \frac{1}{r^2}, \frac{1}{r^2 \sin^2 \theta} \right) \quad (4.63)$$

$$g = n^6 r^4 \sin^2 \theta$$

$$\nabla^2 = \frac{1}{\sqrt{g}} \partial_j \sqrt{g} g^{ij} \partial_i \quad (4.64)$$

Substituting eq. 4.60 to eq. 4.64 Laplace operator in spherical coordinate for Fisheye medium becomes:

$$\nabla^2 = \frac{1}{n^3 r^2 \sin \theta} (\partial_r n r^2 \sin \theta \partial_r + \partial_\theta n \sin \theta \partial_\theta + \partial_\phi n \sin \theta^{-1} \partial_\phi) \quad (4.65)$$

And consequently Helmholtz equation:

$$\left\{ \frac{1}{n^3(\mathbf{r}) r^2 \sin \theta} (\partial_r n(\mathbf{r}) r^2 \sin \theta \partial_r + \partial_\theta n(\mathbf{r}) \sin \theta \partial_\theta + \partial_\phi n(\mathbf{r}) \sin^{-1} \partial_\phi) + \frac{\omega^2}{c^2} \right\} \psi = 0 \quad (4.66)$$

Separation of variables in this equation is not trivial due to the position dependency of refractive index  $n = n(\mathbf{r})$ . Even in the simple isotropic medium that position dependency is radially symmetric  $n = n(r)$  and a generic solution  $\psi$  is separable in variables

$$\begin{aligned} \psi_\omega(\mathbf{r}) &= R(r)\Theta(\theta)\Phi(\phi) \\ r^2 \frac{1}{R} \frac{\partial^2 R}{\partial^2 r} + r^2 \left( \frac{1}{n} \partial_r n + \frac{2}{r} \right) \frac{1}{R} \frac{\partial R}{\partial r} + \frac{\omega^2}{c^2} n^2 r^2 + \left( \frac{1}{\Theta} \frac{\partial^2 \Theta}{\partial^2 \theta} + \cot \theta \frac{1}{\Theta} \frac{\partial \Theta}{\partial \theta} \right) + \frac{1}{\sin^2 \theta} \frac{1}{\Phi} \frac{\partial^2 \Phi}{\partial^2 \phi} &= 0 \end{aligned} \quad (4.67)$$

By the separation of variables in the standard ways we will obtain independent equations.

$$\left\{ \begin{array}{l} r^2 \frac{1}{R} \frac{\partial^2 R}{\partial^2 r} + \left( r^2 \frac{\partial_r n}{n} + 2r \right) \frac{1}{R} \frac{\partial R}{\partial r} + \frac{\omega^2}{c^2} n^2 r^2 = M \\ \left( \frac{1}{\Theta} \frac{\partial^2 \Theta}{\partial^2 \theta} + \cot \theta \frac{1}{\Theta} \frac{\partial \Theta}{\partial \theta} \right) + \frac{1}{\sin^2 \theta} \frac{1}{\Phi} \frac{\partial^2 \Phi}{\partial^2 \phi} = M \end{array} \right. \quad (4.68)$$

Choosing a proper form for  $M = \nu(\nu + 1)$  and  $\Phi = e^{im\phi}$ :

$$\left\{ \begin{array}{l} \frac{1}{n^3 r^2} \partial_r n r^2 \partial_r R + \left[ k^2 - \frac{\nu(\nu + 1)}{n^2 r^2} \right] R = 0 \\ \left\{ \frac{\partial^2}{\partial^2 \theta} + \cot \theta \frac{\partial}{\partial \theta} + \left[ \nu(\nu + 1) - \frac{m^2}{\sin^2 \theta} \right] \right\} P = 0 \end{array} \right. \quad (4.69)$$

Comparing Equation 4.69 with Helmholtz equation in Spherical coordinate and Euclidian vacuum we can conclude the set of solutions  $R_i(r)$  with  $k_i = (\omega_i/c)n(r)$  are weighted by the refractive index function  $n^2(\mathbf{r})$ . Orthogonality relations express this as:

$$\int_V n^2(\mathbf{r}) \psi_i(\mathbf{r}) \psi_j^*(\mathbf{r}) d\mathbf{r} = \delta_{ij} \quad (4.70)$$

Consequently, amplitude of vector potential in vacuum is connected to the amplitude of the potential in MFE by the relation:

$$A_i^f = 2 \int_V n(\mathbf{r}) \partial_r A_i^v(\mathbf{r}) d\mathbf{r} \quad (4.71)$$

which assumed in [60] and [59] as ansatz. factor 2 is here the renormalisation factor at  $r = 0$  in the centre of MFE medium. To find special solutions of the 4.69 assuming MFE as a medium with radial symmetric refractive index Equation 4.60 and implanted point source in the centre of symmetry. In the best strive, the source can be an ideal antenna - a thin vertical coaxial cable or at the extreme case an atomic dipole, though small enough to approximate a point source. From classical electrodynamic we know a simple antenna with real dimensions and a spatial orientation possess an azimuthal symmetric vector potential [64] (eq. 9.55). Even higher multipole expansions for a dipole antenna will hold the azimuthal symmetry [64] (eq. 9.182).

Vector potential of the explained setup has a orientation indicates by direction of dipole current (which we call it  $\hat{\mathbf{z}}$  with out lose of generality) and the amplitude:

$$\mathbf{A} = A(\mathbf{r}, t)\hat{\mathbf{z}} \quad (4.72)$$

applying temporal Fourier transform on  $A(\mathbf{r}, t)$  then  $A_\omega(\mathbf{r})$  have to satisfy equation 4.71. To simplify even more the conditions, we are looking at only at the planar cross section of device then  $A(\mathbf{r})$  reduces further to  $A(r)$  [64](e.q. 9.54). Substituting  $A(r)$  in 4.69 we derive:

$$\frac{1}{n^3 r^2} \partial_r n r^2 \partial_r A + (k^2 n^2 - \frac{\nu(\nu+1)}{r^2 n^2}) A = -\frac{\delta(r)}{2\pi} \quad (4.73)$$

Equation 4.73 shows the relation between the two approaches.

#### 4.4 An Alternative way to Derive EM Equation for MFE

We have seen that the general refractive index profile that position dependency involve all three spatial variables, there is no known analytic method to solve 4.6 and 4.7 in such a case. But fortunately for radially symmetric inhomogeneity that  $n = n(\mathbf{r}) = \sqrt{\mu(\mathbf{r})\epsilon(\mathbf{r})}$ , we can systematically solve them for various boundary conditions. In inhomogeneous medium with radial symmetry homogenous field equations appeared as:

$$\nabla \times \frac{1}{\mu(\mathbf{r})} \nabla \times \mathcal{G}(\mathbf{r}) - \epsilon(\mathbf{r}) k^2 \mathcal{G}(\mathbf{r}) = 0 \quad (4.74)$$

$$\nabla \times \frac{1}{\epsilon(\mathbf{r})} \nabla \times \mathcal{H}(\mathbf{r}) - \mu(\mathbf{r}) k^2 \mathcal{H}(\mathbf{r}) = 0 \quad (4.75)$$

Assuming:

$$\eta_i(\mathbf{r}) = \begin{cases} \epsilon(\mathbf{r}) & i = 1 \\ \mu(\mathbf{r}) & i = 2 \end{cases} \quad (4.76)$$

We have:

$$\nabla \times \frac{1}{\eta_i(\mathbf{r})} \nabla \times \mathcal{F}(\mathbf{r}) - \eta_j(\mathbf{r}) k^2 \mathcal{F}(\mathbf{r}) = 0 \quad i \neq j \quad (4.77)$$

$$\nabla^2 \mathcal{F}(\mathbf{r}) - \eta_i(\mathbf{r}) \nabla \frac{1}{\eta_i(\mathbf{r})} \times \nabla \times \mathcal{F}(\mathbf{r}) + \eta_i(\mathbf{r}) \eta_j(\mathbf{r}) k^2 \mathcal{F}(\mathbf{r}) = 0 \quad (4.78)$$

Inhomogeneity induces an extra term into the left hand side of wave equation. To solve equation 4.78 we are using a method called vector wave functions. It will result into the extension of spherical harmonics to vectorial version. Assume the following definitions:

$$\mathbf{M} = \nabla \times (\psi \hat{\mathbf{c}}) = -\hat{\mathbf{c}} \times \nabla \psi \quad (4.79)$$

$\psi$  is a scalar function and  $\hat{c}$  is a constant pilot vector. From vector analysis  $M$  satisfies following conditions:

$$\nabla^2 \mathbf{M} = \nabla \times (\hat{c} \nabla^2 \psi) \quad (4.80)$$

$$\eta_i(\mathbf{r})\eta_j(\mathbf{r}) = n^2(\mathbf{r}) \quad k^2 n^2 \mathbf{M} = \nabla \times (\hat{c} k^2 n^2 \psi)$$

(Because of spherical symmetry for  $\hat{c} = \hat{r}$   $\nabla \times \eta_i(\mathbf{r})\psi \hat{c} = \nabla \times \eta_j(\mathbf{r})\psi \hat{c} = 0$ )

$$(4.81)$$

$$\vec{a} \times \nabla \times \mathbf{M} = \nabla \times \mathbf{M} \times \vec{a} = \nabla \times (\nabla \times (\psi \hat{c}) \times \vec{a}) \quad (4.82)$$

Therefore:

$$\nabla^2 \mathbf{M} - \vec{a} \times \nabla \times \mathbf{M} + k^2 n^2 \mathbf{M} = \nabla \times [\hat{c}(\nabla^2 \psi + k^2 n^2 \psi) - (\nabla \times (\psi \hat{c}) \times \vec{a})] \quad (4.83)$$

If  $\psi$  satisfy the scalar vector potential:

$$\hat{c}(\nabla^2 \psi + k^2 n^2 \psi) - (\nabla \times (\psi \hat{c}) \times \vec{a}) = 0 \quad (4.84)$$

then:

$$\nabla^2 \mathbf{M} - \vec{a} \times \nabla \times \mathbf{M} + k^2 n^2 \mathbf{M} = 0 \quad (4.85)$$

The same arguments would be valid if we define another vector:

$$\mathbf{N} = \nabla \times \mathbf{N} = \frac{1}{k^2} \nabla \times \nabla \times (\psi \hat{c}) \quad (4.86)$$

The term

$$\nabla \times (\psi \hat{c}) \times \vec{a} \hat{r} \quad (4.87)$$

has to find out for any particular problem base on the profile and boundary conditions. By choosing pilot vector  $\hat{c} = \hat{r}$  we confine the scalar function  $\psi$  to transverse mode to the radial component:

$$\mathbf{M} \cdot \hat{r} = 0 \quad (4.88)$$

For Fisheye medium:

$$\vec{a} = \eta(\mathbf{r})\nabla \frac{1}{\eta(\mathbf{r})}\hat{r} \xrightarrow{\text{for MFE}} \vec{a} = n(\mathbf{r})\nabla \frac{1}{n(\mathbf{r})}\hat{r} \quad (4.89)$$

We are calculating the extra term:

$$\nabla \times (\hat{r}\psi(r, \theta, \phi)) \times n(\mathbf{r})\nabla \frac{1}{n(\mathbf{r})}\hat{r} \quad (4.90)$$

The transverse-to- $r$  statement of the modes,  $\mathbf{M} \cdot \hat{r} = 0$ , plus the spherical symmetry implies that all angular derivatives would vanish while only the radial derivative of angular component of  $\psi(r, \theta, \phi)$  appear at the curl derivative. Therefore  $\nabla \times \hat{r}\psi(r, \theta, \phi)$  in the spherical coordinate only includes:

$$\frac{1}{r}\partial_r r \quad (4.91)$$

Consequently:

$$\nabla \times (\hat{r}\psi(r, \theta, \phi)) \times n(\mathbf{r})\nabla \frac{1}{n(\mathbf{r})}\hat{r} = (0, -\frac{1}{nr}\frac{\partial n}{\partial r}\frac{\partial}{\partial r}r\psi_\theta \hat{\theta}, \frac{1}{nr}\frac{\partial n}{\partial r}\frac{\partial}{\partial r}r\psi_\phi \hat{\phi}) \quad (4.92)$$

Another symmetry argument may omit the azimuthal component. Fisheye medium is equivalent to the central potential in a Column problem [48]. Similar argument about conversation of angular momentum in mechanics results in azimuthal symmetry in the trajectory of light in optics. In the MFE light would confine into a plane even in 3-dimensional space. Therefore, an angular component naturally vanishes.

Left hand side of Equation 4.92 is zero if the following statement is zero:

$$\nabla \times ([\nabla^2\psi + k^2n^2\psi]\hat{r}, 0, 0) - (0, -\frac{1}{nr}\frac{\partial n}{\partial r}\frac{\partial}{\partial r}r\psi \hat{\theta}, 0) \quad (4.93)$$

To find such a condition remember that if  $\hat{a} \cdot \hat{A} = 0$  for any arbitrary constant nonzero vector  $\hat{a}$  and a nonzero vector  $\hat{A}$ , then  $\hat{A} = 0$ . and accordingly  $\nabla \times \hat{A} = 0$ , then one way to satisfy equation Equation 4.93 is to require:

$$([\nabla^2\psi + k^2n^2\psi]\hat{r}, +\frac{1}{nr}\frac{\partial n}{\partial r}\frac{\partial}{\partial r}r\psi \hat{\theta}, 0) \cdot \hat{b} = \\ (4.94)$$

$$\|b\| \cdot ([\nabla^2\psi + k^2n^2\psi]\hat{r}, +\frac{1}{nr}\frac{\partial n}{\partial r}\frac{\partial}{\partial r}r\psi \hat{\theta}, 0) \cdot \mathbb{I} = 0$$

$\hat{b}$  is any arbitrary non-zero constant vector. Consequently:

$$\nabla^2\psi + \frac{1}{nr}\frac{\partial n}{\partial r}\frac{\partial}{\partial r}r\psi + k^2n^2\psi = 0 \quad (4.95)$$

Separation of variables results in:

$$\frac{1}{r} \frac{\partial^2}{\partial r^2} r \psi + \frac{1}{n} \frac{\partial n}{\partial r} \frac{\partial}{\partial r} \psi + \left( k^2 n^2 - n - \frac{l(l-1)}{r^2} \right) \psi = 0 \quad (4.96)$$

In the above deriving we applied the derivative property of MFE profile. And finally:

$$\frac{1}{r^2 n} \frac{\partial}{\partial r} n r^2 \frac{\partial}{\partial r} \psi + \left( k^2 n^2 - n - \frac{l(l-1)}{r^2} \right) \psi = 0 \quad (4.97)$$

The wave equation in the MFE medium. For  $l = 0$  we obtain similar solutions, linear combinations of associated Legendre Functions of first and second type.

$$\psi(r) = \left\{ \left( r + \frac{1}{r} \right) \right\} P_1^\mu(ir) + Q_1^\mu(ir) \quad \mu = 2\sqrt{k^2 + 1} \quad (4.98)$$

## 4.5 Geometrical Optics Exactness of MFE

We will finish this chapter by studying the limiting case of two regimes: waves and rays in the MFE. We examine the behaviour of light waves in the MFE medium in GO regime. In Chapter 1 we saw that geometrical optics is valid if and only if the second term in Equation 1.4, called the quantum potential, vanishes from the Helmholtz-Schrödinger equations [15]. If the term

$$\frac{\nabla^2 R(\mathbf{r})}{R(\mathbf{r})},$$

becomes small enough to be neglected we are in the good GO approximation. However, if under specific circumstances  $\nabla^2 R(\mathbf{r})$  completely vanishes, the GO solutions are exact. Miñano et.al. and Philbin [15] providing methods to tailor waves and reflective index profiles to match this conditions. However, it is no-trivial to have a medium in which all possible GO solutions are exact. To check this exactness for the MFE, we begin with the Helmholtz equation in the Fisheye medium:

$$\frac{1}{n^3} \nabla \cdot n \nabla \tilde{D} + (\omega^2 - 1) \tilde{D} = -\frac{\delta(\mathbf{r})}{2\pi n^3} \quad (4.99)$$

with the solutions [60]:

$$\tilde{D} = \frac{1}{(4\pi)^2} \left( r + \frac{1}{r} \right) e^{2i\omega \arctan r}. \quad (4.100)$$

If we separate the amplitude and phase of the solution and call them  $R$  and  $S$  respectively

$$R(\mathbf{r}) = \frac{1}{(4\pi)^2} \left( r + \frac{1}{r} \right), \quad (4.101)$$

$$S(\mathbf{r}) = 2\omega \arctan \mathbf{r} \quad (4.102)$$

4.100 became in the form of

$$\tilde{D} = R(\mathbf{r}) e^{\imath S(\mathbf{r})}. \quad (4.103)$$

Substituting 4.103 in the homogenous form of Equation 4.99:

$$\nabla \cdot n \nabla \tilde{D} + n^3(\omega^2 - 1) \tilde{D} = 0, \quad (4.104)$$

we will have

$$\nabla \cdot n \nabla (R e^{\imath S}) + n^3(\omega^2 - 1)(R e^{\imath S}) = 0, \quad (4.105)$$

$$\nabla n \cdot \nabla (R e^{\imath S}) + n \nabla^2 (R e^{\imath S}) + n^3(\omega^2 - 1)(R e^{\imath S}) = 0, \quad (4.106)$$

$$[c] \nabla n \cdot \left( \frac{\nabla R}{R} + \imath \nabla S \right) R e^{\imath S} + n \left( \frac{\nabla^2 R}{R} + \frac{2\imath \nabla S \nabla R}{R} + \imath \nabla^2 S - (\nabla S)^2 \right) R e^{\imath S} \quad (4.107)$$

$$+ n^3(\omega^2 - 1)R e^{\imath S} = 0 \quad (4.108)$$

$$\nabla n \cdot \left( \frac{\nabla R}{R} + \imath \nabla S \right) + n \left( \frac{\nabla^2 R}{R} + \frac{2\imath \nabla S \nabla R}{R} + \imath \nabla^2 S - (\nabla S)^2 \right) + n^3(\omega^2 - 1) = 0 \quad (4.109)$$

Putting the real and imaginary parts to zero independently, we obtain the equation pair:

$$(\nabla S)^2 - \frac{\nabla^2 R}{R} - \frac{\nabla n}{n} \cdot \frac{\nabla R}{R} + n^2(1 - \omega^2) = 0, \quad (4.110)$$

$$\nabla \cdot (n R^2 \nabla S) = 0. \quad (4.111)$$

Now the question is whether the MFE solutions satisfy the Eikonal relations of GO. The difference between Equation 4.110 and the Eikonal Equation 1.4 is the second term:

$$(\nabla S)^2 - \left\{ \frac{\nabla^2 R}{R} + \frac{\nabla n}{n} \cdot \frac{\nabla R}{R} - n^2 \right\} - n^2 \omega^2 = 0, \quad (4.112)$$

As we can see for the MFE medium is not only the quantum potential that needs to be zero, but also some extra terms which relate to inhomogeneity and also especial for

form of wave equation which at  $n \rightarrow 1$  the equation will not asymptotically reach the form Equation 1.4.

If the second term in Equation 4.112 vanishes, then the geometrical optics for the MFE is exact:

$$R = r + \frac{1}{r}, \quad n(r) = \frac{2}{1+r^2}. \quad (4.113)$$

We obtain

$$\frac{\nabla^2 R}{R} + \frac{\nabla n}{n} \cdot \frac{\nabla R}{R} - n^2 = \frac{2}{r^2+1} - \frac{2r}{r^2+1}, \frac{r^2-1}{r(r^2+1)} - \frac{4}{(r^2+1)^2} = 0 \quad (4.114)$$

which shows that the geometrical optics for the the MFE is exact. Because this zero term in Equation 4.112 is frequency independent, we may conclude that the GO is exact in MFE for all frequencies. Thus, the wave fronts must follow the the Eikonal equation and therefore be orthogonal to geodesics.

Nevertheless, the question remain if the exactness of GO can result in diffraction free imaging. To answer this we must clarify two facts first the imaging properties which is shared between GO and full wave optics; and, second, finding a proper energy distribution at the image point.

# Chapter 5

## Experimental Evidences: Imaging properties of absolute optical instruments

### 5.1 About The Chapter

The purpose of this chapter is to give critical review on three important experimental attempts to test the resolving power of Maxwell's Fisheye-type lenses in the microwave spectrum based on our initial theoretical model described in previous chapters.

We have a critical view of some of the methods, implied in data collection, and experimental outcomes which reported in [5, 8]; but, because these results have appeared in scientific publications and were the subject of many debates, we feel we should clearly explain our view on the methods [65]. In the following we report the detailed procedure and model for further investigation.

### 5.2 Experimental Demonstrations

After a series of publications on the ultimate imaging resolution of Maxwell's Fisheye [16, 59, 60, 66, 67], several investigations, both experimental and numerical, were performed in the community to demonstrate the actual imaging capability of the device or its limits <sup>1</sup> [5, 8, 68, 69]. However, different experimental and numerical studies still have not resulted in a consensus about the Fisheye's imaging capacity as a device for practical applications. In our opinion, the reason for this is simply that conventional criteria for image resolution do not apply to unconventional devices like Maxwell's Fisheye. We hope this research, followed by new experiments will facilitate a better understanding of

---

<sup>1</sup>Surveys also include equivalent devices like SGW (spherical geodesic wave guides), the Modified Fisheye, and in general, absolute optical instruments [7].

the physics of imaging. In the early stages of the study [5, 8, 16, 59, 60] our investigation focused on the imaging power of the mirrored Fisheye lens and whether or not it could achieve a perfect imaging. In this chapter we present the experimental evidence for the Fisheye's imaging properties accordingly to current knowledge and recent findings.

In 2010 we made a first experimental run [5] of wave focusing and resolution tests on MFE in collaboration with Y. G. Ma's experimental team at National University of Singapore, reported in [5]. Ma's experiment confirmed the essential role of the drain in the formation of a sharp image at a single detector at fixed frequency. We firmly count the results of that experiment as a proof of the sharp focusing ability of the mirrored Fisheye when equipped with a drain. Ma's group also performed a resolution test with two light sources and an array of detectors to check the Rayleigh resolution criterion. The results, however, showed some deviations from our theoretical arguments and simulations [3, 70]. Later we became aware that serious experimental flaws had occurred [65]. Soon after, Miñano's group in Madrid performed a resolution test for a wide spectrum of frequencies with a single source and a single mobile detector on the spherical geodesic waveguide (SWG)—which optically is an equivalent lens to the MFE [71, 72]. They reported numerical and (later) experimental indications of super-resolution for the SWG when a single mobile detector is in action. However, the super resolution only appeared at specific frequencies known as notch frequencies. Later, Hao's group in Queen Mary College of London confirmed, in simulations, the frequency-dependency of the resolution of the original Fisheye device [68].

In this chapter we first describe the Singapore experiment performed by Y.G. Ma in collaboration with our group [5], then an experiment [8] with a modified Fisheye lens, also performed by Y.G. Ma at Singapore in likewise with our group. Later, we compare Miñano's experiment with Ma's results and discuss the consequences of Miñano's findings.

The design of the two Singapore experiments [5, 8], the configuration of their setups, and the methods of efficient detection were planned and calculated by Leonhardt and Sahebdivan, based on theories developed by Leonhardt, Tyc and Sahebdivan. The implementation of the setups, data detection, data collection, and the reporting of the data was done by Ma's group in Singapore.

### 5.3 Experimental Evidence I; Mirrored MFE, Ma *et al.*'s Setup

Fisheye mirrors were implemented for microwave radiation confined between two parallel metal plates establishing a planar waveguide. The device, with the radius of 5cm,

was inserted between the plates; the varying index profile,  $n(r) = \frac{2}{1+r^2}$ , permits microwaves in the planar waveguide to behave as if they were waves on a virtual half sphere (Figure 5.1).

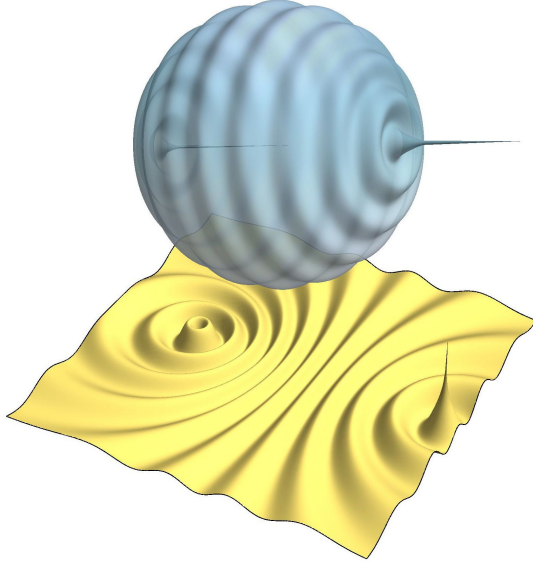


FIGURE 5.1: Focusing in curved space. In Maxwell's Fisheye, electromagnetic waves propagate in a plane in physical space (wave pattern below) as if confined to the surface of a sphere (above). A wave emitted from any point on the virtual sphere is focused at the antipodal point. In physical space, waves are as perfectly focused as in virtual space.

The plate separation, 5mm, was chosen so that only microwaves with an electric field perpendicular to the plates could travel inside because only for electromagnetic waves of this polarisation does a material with electric permittivity  $\epsilon = n^2$  appear to curve space perfectly [60]. Our device (Figure 5.2) resembles a microwave cloaking device [73] or a transmuted Eaton lens [74] made of concentric layers of copper circuit board (Rodgers RT6006) with etched-out structures that shape its electromagnetic properties, except that the Fisheye structures respond to the electric and not the magnetic field [73, 75]. The structures were originally designed for non-resonant operation so that the device could perform perfect imaging over a broad spectral band.<sup>2</sup>

The device has a radius of 5 cm, a thickness of 5 mm, and fits precisely between the metal plates of the waveguide. We used coaxial cables as sources, inserting them through the bottom plate. The cable has an outer diameter of 2.1 mm, a 1.68 mm Teflon isolator, and a 0.5 mm inner conductor; the latter is exposed by 4.5 mm in the device for creating an approximate line source. Through the source cable, we injected microwave radiation of free-space wavelength  $\lambda_0 = 3$  cm generated by a vector network analyser (HP 8722D) that doubles as synthesiser and analyser. The outlets were inserted through the bottom plate as well, but were completely passive and led to absorbers impedance-matched to

<sup>2</sup>Our observations were limited to a single frequency. Further studies question the broadband capacity of the device [1, 68]. However, their findings do not conflict with this experimental demonstration.

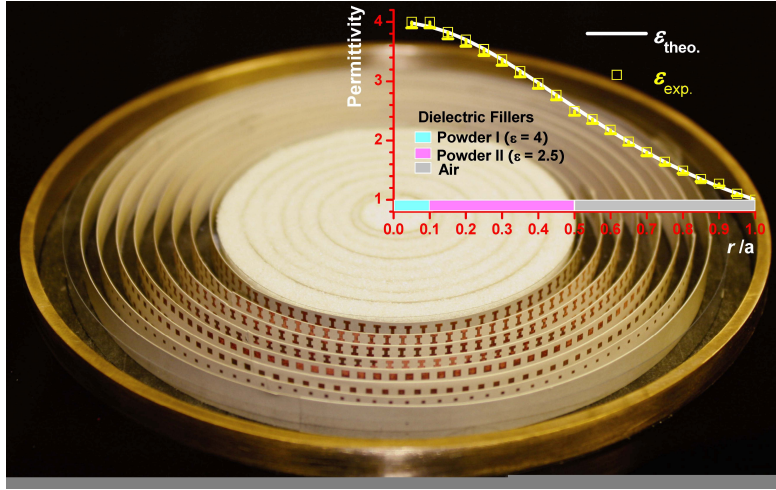


FIGURE 5.2: The device. Copper structures on concentric layers of a circuit board and dielectric fillers surrounded by a circular metal mirror create the geometry of the sphere for microwave radiation with the electric field pointing in the vertical direction. The diagram shows the designed profile of the electric permittivity  $\epsilon = n^2$  at each layer of the device compared with Maxwell's theoretical formula

the cables. They led back to the vector network analyser for detection or terminated in impedance-matched absorbers, depending on their role in our experiments. They acted as passive outlets and did not cause significant reflections. We varied the exposure lengths of the inner conductors in order to vary the electromagnetic cross sections of the cables, trading efficiency for resolution. An outlet with 4.5 mm exposure perfectly matched the source and therefore had maximum extraction efficiency [76]. But it had a cross section of about half the wavelength [77], which is not suitable for sub-wavelength detection. Outlets with 2 mm exposure would have been optimal for resolving sub-wavelength features of the field because their cross section is comparable to the structure size in the device, but their efficiency is lower. An outlet with no exposure does not localise the wave because its cross section is too small, but merely scans the local field with minimal distortion. The bottom plate of the waveguide is movable laterally relative to the top plate with 1 mm step size [78]. To scan the field, we inserted an outlet with no exposure through the top and measure the signal while moving the bottom plate. The scanning cable feeds into the vector network analyser where the signal is measured and decomposed into in-phase and out-of-phase components with respect to the synthesised field. Mathematically, these components correspond to the real and imaginary parts of the complex temporal Fourier amplitude taken at each scanned spatial point in the waveguide.

### 5.3.1 Experimental Results; The Focusing of the Field With and Without Drain

Figure 5.3 illustrates the schemes of two experiments for probing the behaviour of Maxwell's Fisheye and comparing it with theory [16, 60]. In the first experiment, they scanned the field produced by a source without an outlet at the expected image location. In the second experiment, they placed an outlet optimised for power extraction at the image point. To realise the sub-wavelength details of the image, we needed to look for the sub-wavelength features near the image originating from the structure of the materials: in this setup these are the rings of the circuit board used to implement Maxwell's Fisheye. In the first case, without an outlet, the field forms a standing wave (Figure 5.3b), where the outgoing radiation arrive at the image point is reflected back inward to the source. Interference between ingoing and outgoing waves at the image point perform a standard diffraction limited image. No sub-wavelength focus is found. However, the potential of perfect imaging is already there, but only realised if there is an outlet located at the image point (Figure 5.3c). In this case, they obtained a running wave a sub-wavelength spike. The figure shows both the real and the imaginary part of the field amplitude, thus proving that most of the injected microwave radiation establishes a running wave [60] that leaves the device at the outlet.

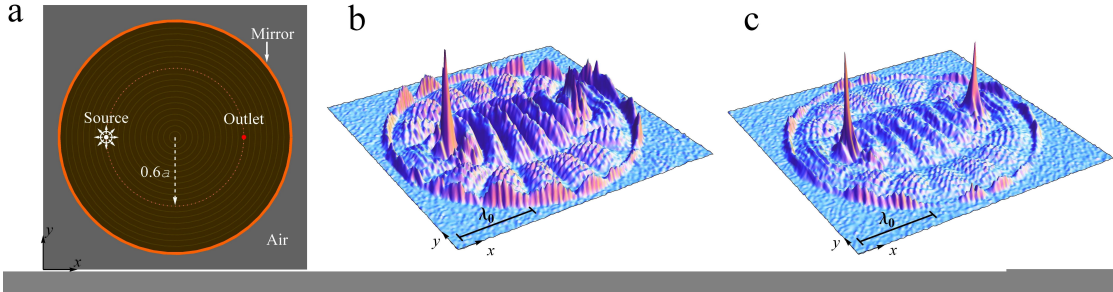


FIGURE 5.3: Field pattern. (a) Scheme of two imaging experiments of a point source without the outlet (b) and with the outlet (c) at the image point.  $\lambda_0$  indicates the free-space wavelength of 3 cm. The field intensity is scanned. Without the outlet, no sub-wavelength focus is formed, whereas with the outlet a sharp spike appears at the image.

The agreement with theory [16] is remarkably good, considering that the device is made of a structured material and that source and outlet are not ideal. The source and outlet have electromagnetic cross sections much larger than their geometrical size. It seems that in this stage the focusing is limited by the source and the detector's resolution, which in principle can be improved.

This experiment resembles the MFE as a time reversal focusing device[27, 36]. For the sake of the argument, the drain plays the same role as a time reversed source. This analogy with time-reversal imaging clarifies the reason for the spatial symmetry between

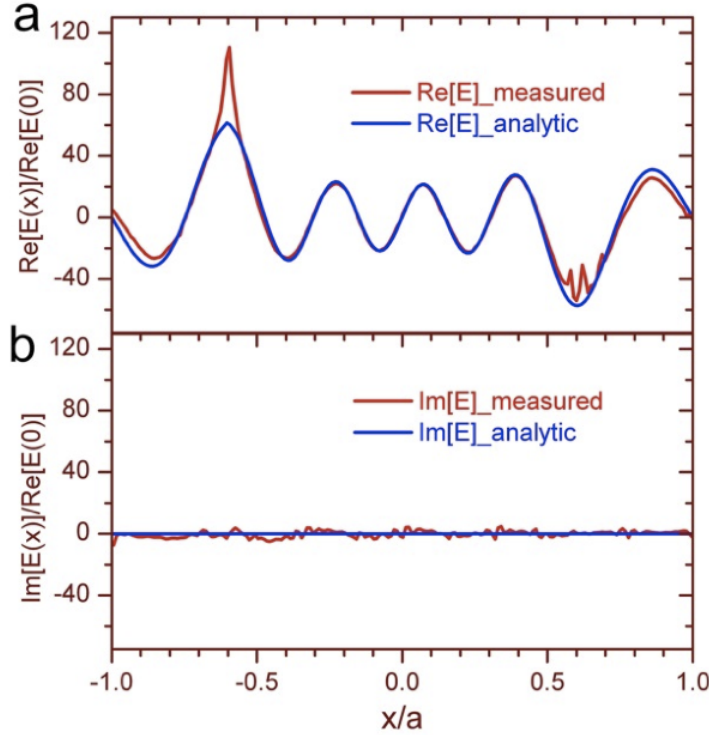


FIGURE 5.4: Comparison with the theory for radiation without an outlet. The field amplitude scanned along the line between the source and the outlet is compared with the analytical expectation. The figure shows a standing wave in very good agreement with theory. The sub-wavelength features near the image originate from the structures of the material used to implement the Fisheye mirror. The deviation near the source is due to its imperfection.

the position of the source and the drain. From the theoretical point of view, time reversal ultimately brings about focusing for any wave-like entity. Upon time reversal a wave that was emitted from a point-like source, gets focused in a point-like drain, provided that the drain is also the time-reversed of the source. We conclude that the experiment confirms the MFE working as an ultimate focusing device. Though, whether the ultimate focusing of waves does necessarily result in the ultimate resolution or not is subject to a deeper study.

### 5.3.2 Resolution

Based on the most widely used definition of spatial resolution, the best way of verifying resolution power is by at least a pair of neighbouring sources and an array of detectors. Here, for sake of documentation, we report an experimental run that had the aim of testing the resolution of MFE. This setup can in principle be regarded as a model for further investigation. However, based on the theory developed in Chapter 6 we do not expect the detection of sub-wavelength resolution in this very current setup, because in reality sources and drains are strongly coupled. This effect is considered in detail in

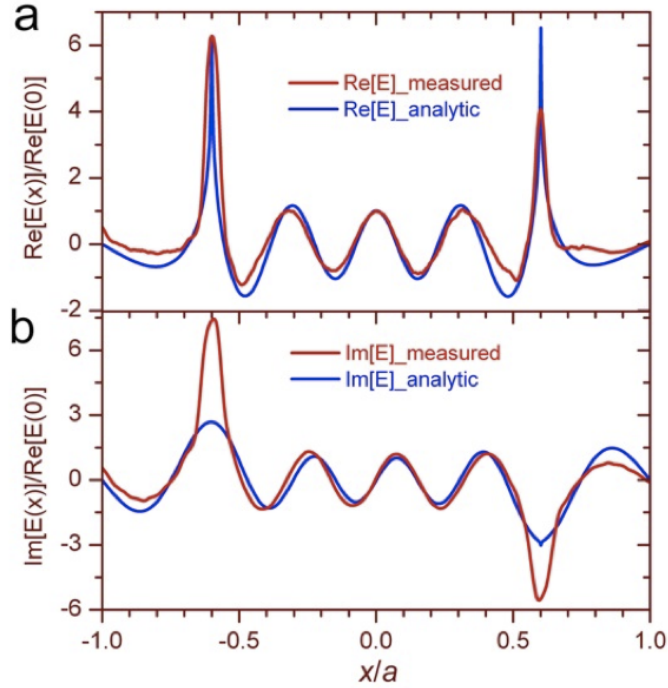


FIGURE 5.5: Comparison with the theory for the wave with the outlet. The field amplitude scanned along the line between the source and the outlet is compared with the analytical expectation. The figure shows a running wave with complex wave function in good agreement with theory: the sharp spike of  $\text{Re}(E)$  is a nearly perfect image of the source.

Chapter 7. The experiment appeared to show sub-wavelength imaging. However, we believe this was the consequence of incorrect assumption by Y.G. Ma's group in the data collection and data interpretation. Nevertheless, because this experiment and its results have appeared in the scientific literature, it needs to be discussed and corrected.

For testing double source resolution, Y.G Ma inserted two source cables  $0.2 \lambda$  distance from each other, where  $\lambda$  denotes the local wavelength  $\lambda_0/n$ . In ordinary imaging [7] the two sources would not be resolvable. They captured the image with an array of ten outlets of 2 mm exposure inserted in the bottom plate in an arc with  $0.05 \lambda$  spacing between them; they represented a detector array. Two of the outlets were at the correct image points, but the others were not: for perfect imaging, only the detectors at the correct points should fire. They did not directly monitor the field intensity extracted by the outlets: their cables terminated in absorbers because it is experimentally easier to scan the field localised at the outlets. Because the intensity at the outlets is proportional to the extracted field intensity, this procedure gives the intensity profile recorded by a detector array. For scanning the field at the image, they inserted another outlet of the same type (2 mm exposure) through the top plate. For scanning the field at the source they used outlets with no exposure. The scanning outlet was connected to the vector

network analyser for measuring the throughput. They moved the top outlet in discrete steps along the arc and recorded the intensity at each step.

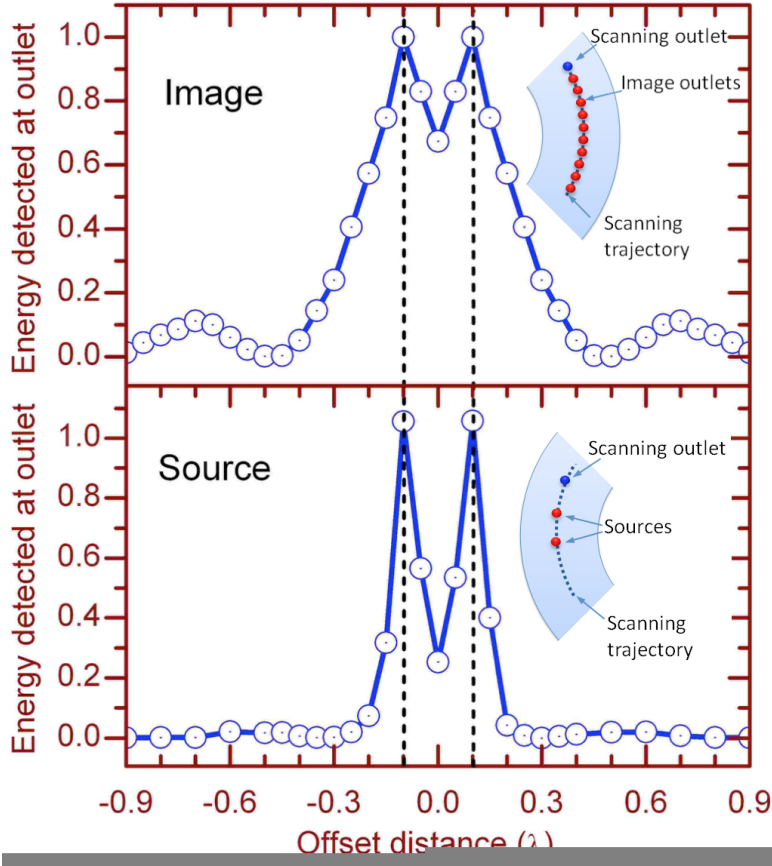


FIGURE 5.6: Diagram is comparing the detected intensity at sources and detectors. It shows the recognisable peaks of intensity on the imaging surface from two point sources separated by only a small fraction of the wavelength. However, a serious misassumption by the experimentalists on the symmetry of the field distribution cause a misleading results [65]. In this diagram, only half of the data was detected and the another half assumed to be mirrored symmetrically[65]. Thus this diagram cannot be taken as evidence for super resolution by MFE.

Our theoretical studies, described in chapters 6 and 7, show that sub-wavelength-distanced sources and drains interact with each other, resulting in dramatic distortions in image formation. This argument is also valid for the experiment with the modified mirrored MFE discussed in the next section. However, in our opinion this dramatic deviation would not necessarily prove MFE incapable of super-resolved focusing or imaging. Moreover, we strongly believe that the localisation of the field, in contrast to what has been claimed in the controversy about perfect imaging with positive refraction [49, 66, 79–86], is not an artefact of the outlets. The role of the drain is to provide the time-reversal symmetry of the source [27].

## 5.4 Experimental Evidences II; Modified Mirrored MFE, Ma *et al.*'s Setup

### 5.4.1 Background

In this section, we describe the experimental setup [8] used to verify the focusing and imaging ability of the modified MFE. In contrast to the original MFE, which has the large refractive index range of 1 to 2 from centre of the device to the border, our modified MFE lens in principle requires an arbitrarily low index contrast between the centre and the edge. The advantage of the modified Fisheye is the ease of manufacturing compared to MFE. The goal of the experiment is to verify whether, despite such a modification in the structure of the lens, the focusing property of the device will remain favourably compare to that of the original MFE. Such a device can be manufactured from conventional graded-index materials. In our implementation, however, we used, because of its low cost, microwave metamaterial. We have demonstrated sub-wavelength imaging test for microwaves because microwave technology provides a degree of detail and precision currently impossible in the optical range of the spectrum. In addition to demonstrating an idea for reducing the demands on the materials required for perfect imaging systems, our experiment illustrates a fundamental point that may also become important in practice: we demonstrate that it is not necessary to detect the field with perfect efficiency. The undetected part of the field does not localise at the detectors with sub-wavelength resolution, but the detected part of the field finds its way into the right detectors. The sub-wavelength image appears in the detectors, but not necessarily in the field around them. However, what counts in practice is only the detected part of the field, which implies that the efficiency of the detectors is less important than their resolution.

### 5.4.2 Setup; Modified Mirrored MFE

Figure 5.7 shows a picture of our device. It is used for microwave radiation of 30 mm free-space wavelength (10 GHz frequency). The lens is placed inside a thin brass dish that acts as a circular mirror at the sides and a ground plate at the bottom. In our device,  $r_0 = 50$  mm and  $r_1 = 65$  mm. It consists of 17 metamaterial rings with a height of 5 mm. The 15 inner rings are made of patterned Rogers Ultralam 3000 circuit board or square-shaped copper structures on one side. The spacing between two neighbouring rings in the radial direction is 2.94 mm: thus the unit size of the cells on each ring is one order of magnitude smaller than the wavelength. The two outer rings are simply made of a 0.1 mm thick mylar substrate. The inset of Figure 5.7 shows the theoretical (blue line) and simulated (red squares) values of  $\epsilon = n^2$  for the rings of the lens. The simulated values are numerically retrieved from the scattering parameters of a stack of planar metamaterial sheets with given patterns [74].

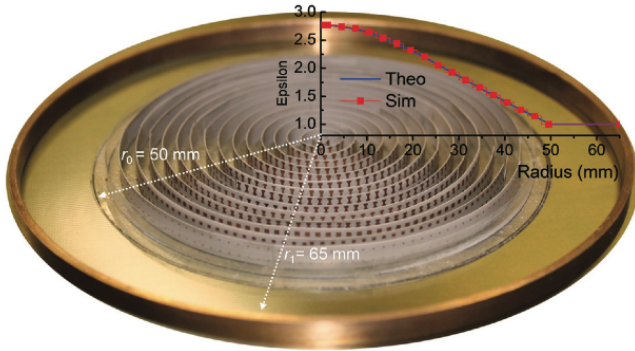


FIGURE 5.7: Microwave image device for the modified Fisheye. The lens sits in a brass dish that serves both as a circular mirror and a ground plate. The modified Fisheye profile is produced by a microwave metamaterial made of a patterned circuit board. The inset shows the theoretical curve of  $\epsilon = n^2$  versus the simulation results for the metamaterial layers

In the experiment, the lens was placed inside a parallel-plate waveguide mounted on a flat stage driven by a computer-controlled  $x - y$  step motor [5, 74]. With the movable waveguide, the experimentalist scan the field through a scanning cable. The scanning resolution is given by the step size, 1 mm. For scanning, Ma's group used a coaxial cable connected to a vector network analyser (HP 8722D) that also synthesised the microwave radiation they injected into the chamber. As sources and drains, they used coaxial cables as well. All cables were Teflon-filled and had a 1.68 mm outer shell diameter and a 0.5 mm inner core diameter. By adjusting the exposure of the inner core, they could control the cross section of the cables. The scanning cable had zero exposure and the source and drain cables have an exposure length of 4.8 mm. Observations showed that in these experiments the cross section of the cables is important for the detection of the ultimate imaging. We believe that this can be explained as follows: In this experiment, due to either a fundamental reason or simply some manufacturing granularity of our device, the electromagnetic waves cannot localise below a certain length scale. If the cross section is smaller than this scale, as the cross section of the scanning cable certainly is, one cannot extract sufficient radiation from the field for forming a sub-wavelength image. The scanning cable simply scans the field and does not alter it significantly. The exposure length of the sources and outlets was optimised for maximal field localisation, which probably means that it was optimised for reaching the cross section that matches the localization length in our device. Our collaborators in Singapore scanned the field at the outlets. They also measured the field going through the outlets as follows: All outlets but one were terminated by impedance-matched absorbers; the one outlet is connected to the detecting port of the vector network analyser where the amplitude was measured. The throughput through each outlet is measured one by one by repeating the experiment within the relevant outlet connected. In this way, we demonstrate the effect of a multiple detector array with just one live detector at a time.

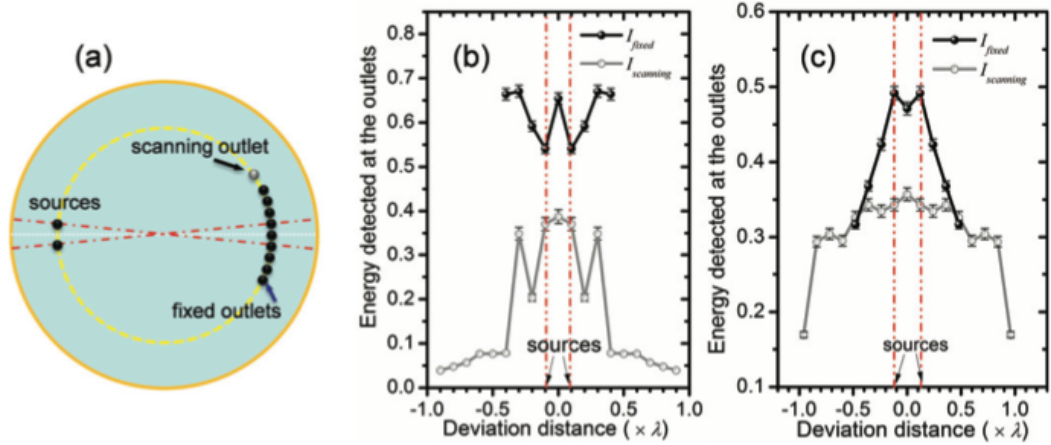


FIGURE 5.8: Microwave image device for modified Fisheye. The lens sits in a brass dish that serves both as a circular mirror and a ground plate. The modified Fisheye profile is produced by a microwave metamaterial made of a patterned circuit board. The inset shows the theoretical curve of  $\epsilon = n^2$  versus the simulation results for the metamaterial layers

Ma's group repeated the entire experiment four times to reduce statistical fluctuations. We investigate two cases: sources and detectors outside the lens (for  $r_0 < r < r_1$ ) and inside the lens (for  $r < r_0$ ) corresponding to the ray trajectories illustrated in Figure 3.5 which shows the results for the attempted imaging outside of the lens and figure 7(c) the results when the sources and detectors are inside the lens area. In both cases the scanned field (grey dots) did not resolve the two sources. In our joint article, [8], we reported that, when the imaging occurs inside the lens the measurements of the throughput (black dots) resolved the sources though they were separated by just 0.2 of the local wavelength. However, as in the previous experiment, described in above section ([5]), we believe the initial data collection process, applied experimentally to test the resolution, was based on a faulty assumption about the spatial symmetry of the outcomes. These assumptions might not be valid. Therefore, we suggest a different preparations for the experiment are needed to determine the true resolution limit of original MFE or Modified MFE. The author of this thesis strongly believes that neither of the implemented experiments nor the simulations, presented in the community, up until today, provide sufficient evidence or physical reason that the Maxwell Fisheye would be incapable of forming in a super-resolved image.

## 5.5 Experimental Evidence III; Imaging at Resonance Frequencies, Miñano *et al.*'s Experiment

The Spherically Geodesic Waveguide (SGW) is an absolute optical device introduced by J. Miñano. By the methods of transformation optics, he showed that the SGW is

optically equivalent to the MFE medium in two dimensions [55], meaning that in both devices the fields behave the same. In this chapter, we briefly review the experimental and numerical findings of J. Miñano and his colleagues. Their results, to our understanding, are valid for the MFE.

### 5.5.1 Comparison Between Two Experiments; MFE in Singapore vs. SWG in Madrid

The Singapore experiment confirmed in practice the sub-wavelength localization of the field in the mirrored MFE equipped with a single drain. However, Y.G. Ma reported it only for a single frequency corresponding to  $\lambda = 3\text{ cm}$ .

Miñano *et al.* presented a steady state simulation on a broad window of frequencies for the SWG, which is an optically equivalent device to the MFE [1].

It turned out that the focusing property of MFE or SWG is limited to certain discrete frequencies, due to cavity resonances. These frequencies, are located in the spectrum very close to frequencies corresponding to the integer values of the  $\nu$  (see Ref. [67]): they are known in geophysics as the Schumann frequencies.<sup>3</sup> Miñano *et al.* report super-resolution of up to  $\lambda/500$  in a numerical study [1], and up to  $\lambda/105$  in an experiment [2]. Their results agree with our Singapore experimental field localization in  $\lambda = 3\text{ cm}$  or equivalently  $\nu = 9.98$ , which is rather close to the Schumann frequency for  $\nu = 10$ .

### 5.5.2 SWG, The Spherically Geodesic Waveguide

The general structure of the SGW suggested by Miñano *et al.* [67] is similar to the MFE experimental setup [5, 8].

The SGW, Figure 5.9, is equipped with two geometrically identical coaxial probes loaded with corresponding impedances as source and drain, which Miñano *et al.* called ports. In the SGW setup [2, 67], in contrast to our initial theoretical model drain does not emulate the perfect point drain: there is no full absorption. Therefore, reflected fields from the drain might present inside the device. Power is injected through the source point, and the radiation is guided through the SGW and partially extracted from the medium through the drain port [2]. For a single source in the system, only a single drain is used.

In this experiment, the method of detection is based on moving the single drain to measure the resolution of the imaging. By gradually dislocating this mobile drain and reading its power output, the resolution of the device can be determined.

---

<sup>3</sup>Schumann frequencies are the resonance frequencies of a spherical waveguide created by the atmosphere around the Earth.

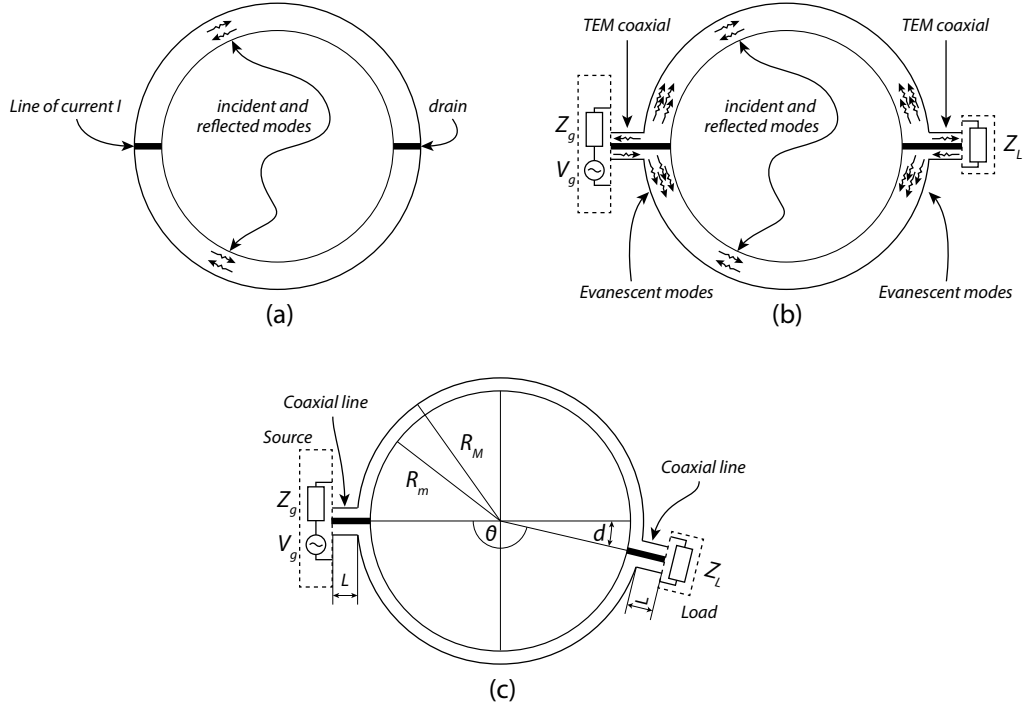


FIGURE 5.9: Microwave (a) SGW with a current line source and a line drain located at the antipodal position. (b) SGW with the source implemented as input coaxial ports with a voltage generator  $V_g$  and an impedance  $Z_g$  and the drain implemented as an output coaxial port loaded with an impedance  $Z_L$ . (c) Concept of super-resolution in the SGW: the drain is displaced an arc length of  $\lambda/N$  from the antipodal position of the source and the output power is measured at each position (Picture adapted from [2]).

To interpret the data from the experiment and simulation, Miñano *et al.* defined the resolution in specific Fisheye-like optical device:

**Definition 5.1.** : *Optical resolution in SWG and similar devices is defined as the arc length in the wavelength units which a drain port needs to be shifted such that the detected intensity of the field drops to 10 percent .*

At first glance, this definition would seem to follow the same principle as Rayleigh's definition. However, the two are in fact different. Therefore, any conclusions or comparisons with conventional cases must be made carefully.

### 5.5.3 Sub-wavelength Localization of The Field at Resonance Frequencies

In the first run, a source port and a drain port were implanted in antipodal locations. In this configuration the flow of energy reaches the maximum at the outlet, but only at

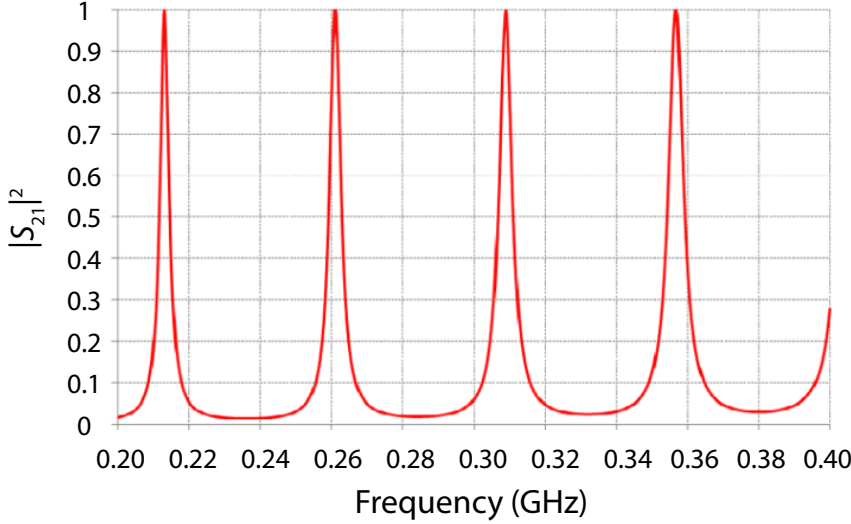


FIGURE 5.10: Intensity as a function of frequency when drain and source ports are at opposite poles. The peaks occur at the Schumann resonance frequencies. (Graph is adapted from [1]).

specific discrete rather than arbitrary frequencies.<sup>4</sup> The system shows a perfect match with theoretical predictions but only at very specific set of frequencies. These frequencies are known as Schumann resonance frequencies and are related to the resonance frequencies of a spherical waveguide (Figure 5.10; figure 5 in [1]).

More significant results appear when one measures the resolution by moving the drain from its antipodal imaging position for  $\frac{\lambda}{30}$ . If the SWG has a capacity of ultimate resolution, we would expect that the off-positioned drain would fail to concentrate the field at the sub-wavelength neighbouring point. Surprisingly, the simulation shows high amplitude intensity except at a very narrow line, where the intensity drops to almost zero for the Schumann frequencies, (Figure 5.11; figure 6 in [1]).

At non-resonance frequencies, for sub-wavelength deviations of the drain from the antipodal position, we have no drops in the detect fields: a point source is imaged into a diffracted spot. This shows that for non-resonance frequencies, the field localization lies within the diffraction limit. On the other hand, the opposite is true for resonance frequencies, a sub-wavelength deviation results in a dramatic fall in the intensity that can be interpreted as an ultimate concentration of the field in the sub-wavelength area at the antipodal point of SGW, but only in extremely narrow bands around several discrete frequencies. The conclusion is that the SWG, and, as a corollary the equivalent

<sup>4</sup>In Chapter 6 we will see the theoretical reason for this feature.

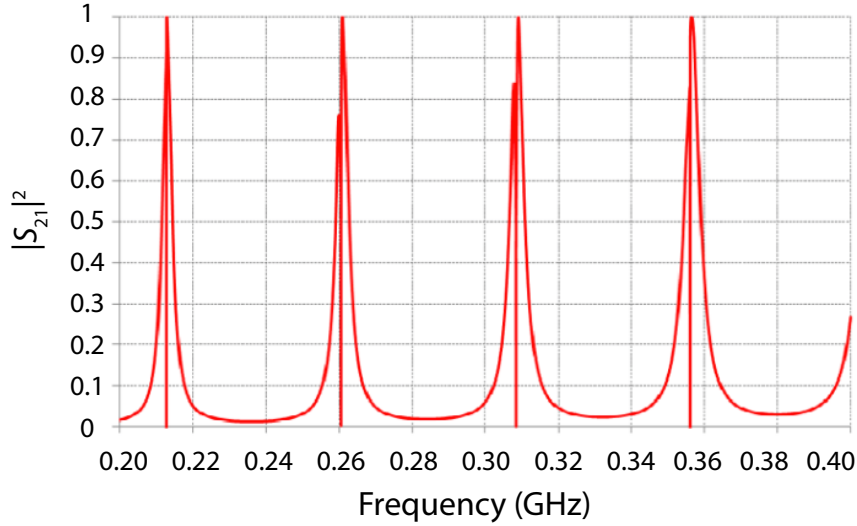


FIGURE 5.11: Intensity versus frequency when the drain port is shifted  $\lambda/30$  ( $\lambda = 1$  m) from the source port antipode. The results are similar to those presented in Figure 5.10 in accordance with the classic prediction, except for the very narrow notches near the Schumann frequencies. (Picture is adapted from [1]).

devices like MFE, perform ultimate focus of the field at resonance frequencies. Based on the experimental and numerical reports in [2] and [68], we conclude that the MFE and its equivalent devices are frequency-dependent focusing systems with a precision beyond that of conventional optical devices.

#### 5.5.4 Interpretation of the Dip in the Intensity Graphs

As Figure 5.10 shows, for resonance frequencies at the antipodal point—the location that theoretically is expected to have the ultimate focus of the field—the intensity of the field is maximal. At resonance frequencies, a slight sub-wavelength deviation results in a dramatic fall in intensity. The absence of the field at neighbouring points is significant. This picture is consistent with a general argument from the Green's function of the system. Asymptotic behaviour of the Green's function for both source and drain is equal: both tends toward the logarithm—in 2D/ delta function—in 3D behaviour. Nevertheless, theory cannot provide clear explanation why at non-resonance frequencies the image turns into a diffracted spot.

In the next chapter, we develop a model to describe the action and reaction of sources and drains with both considered as identical physical entity. A very special configuration of MFE-like instruments with closed optical paths results in the mutual dynamic interaction of source and drains. We show that, because of this mutual interplay, at resonance the

intensity of the field out-of-the-focus (that is, at points neighbouring the antipodal point) would be zero.

### 5.5.5 Miñano’s Model of Detection and Breaking the Diffraction Limit

Strikingly, the resolution limit of a particular device strongly depends on the definition of the term “resolution”.

If one accepts that the Definition 5.1 is an acceptable definition of “resolution” and accepts that the condition is satisfied by the experimental setup described above, then SWG and MFE can both be considered super resolution devices because they can give an image of a single point source much smaller than the wavelength.

However, in practical cases the configuration of sources, drains and their mutual interactions are more complicated than a single point-source–point-drain, therefore, a valid mechanism for the extension to arbitrary real-size objects is essential. More important, in our experimental model, the intensity of two neighbouring points were measured simultaneously, unlike the experimental model of Miñano *et al.*, that the detection of an image is based on a single detector. With a single detector, the measured intensity at one point tell us nothing about the intensity at the neighbouring point, however, to be in agreement with classical –Rayleigh –type– criteria for resolution, the intensity must be known at both points simultaneously. However, though, this single detection is a loophole which allow us to achieve super resolution, but does not necessarily let us truly exceed the fundamental diffraction limit.

## Chapter 6

# The Spectrum of The Maxwell Fisheye Medium; One Dimensional Model

### 6.1 Introduction

Miñano and his colleagues showed that in the SWG a point detector is sensitive to displacements of a point source with an accuracy that is significantly better than the diffraction limit. The outstanding feature of their findings is that sub-resolution behaviour is achievable only specific resonance frequencies [1, 2, 67, 71]. However, no physical explanation for this phenomenon has yet been found. In particular, the physical reason for the appearance of a dip in the diagram of intensity at resonance frequencies, which is a guarantee of a sub-wavelength resolution, was entirely unclear. In this chapter we develop a simple model in one dimension to describe the spectrum observed by Miñano *et al.*. In the next chapter we will extend our model into two dimensions. It is important to emphasise that the key phenomenon missed so far in all of the discussions about MFE is the interaction between source and drain. This mutual relation between source and drain is one of the most novel ideas in this thesis and the original contribution to our understanding of the unusual characteristics of MFE’s imaging behaviour. By bringing this coupling into the calculation, we provide a more elaborate theoretical model to describes the conduct of fields at the focal point of The Maxwell Fisheye. Our analysis is possible thanks to the theoretical model for mutually interacting sources and drains we develop in this paper. Modelling such sources and drains analytically has been a major challenge [49, 86–90]: full numerical simulations [2, 68] have been difficult due to the large difference in the scales involved – specifically, the field localization near the sources and drains versus the wave propagation in the device. Our analytic theory draws from a simple, one-dimensional model [3] that explains the experimental data [1].

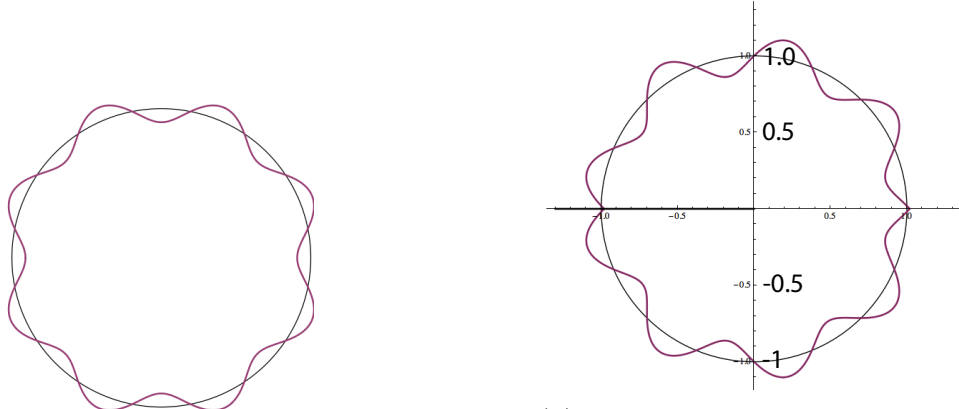
Beginning with the Lagrangian of the electromagnetic field interacting with the current [91], we construct a Lagrangian that reproduces the 1-dimensional model [3] and has the advantage of being extendable to higher dimensions. We extend our model to two dimension in Chapter 7.

## 6.2 Some Characteristic Features of MFE

Before explaining our theoretical model, we will briefly introduce the distinctive characteristics of MFE, which have a significant role in our model of imaging. We hope this discussion give some insights into the controversies about the MFE. The first characteristic feature of the MFE is the drain. The role of the drain in image formation in MFE has been the subject of considerable debates [49, 58, 60, 66, 68, 79–86, 92–94]. However, the author of this thesis believes the role of detection in perfect imaging has to be considered beyond the particular case of the MFE. Any algorithm for super-resolution needs to discuss the contribution of the detecting process, in optical resolution, and might even need to provide non-conventional methods of detection. The perfect transfer of the electromagnetic field from object to image is only possible if the image is probably detected. Moreover, we have just recognised that the coupling between the source and the detector plays a novel role in the formation of the image in the MFE. Another important point is the frequency-dependent behaviour of fields inside the MFE medium. Unlike most optical lenses, MFE is restricted to resonance frequencies. This is because MFE behaves as a spherical cavity. In this section we first show that the confinement of the fields is responsible for the frequency dependence of imaging and then discuss the role of detection, providing a mathematical model for perfect and imperfect drains.

### 6.2.1 Resonance Frequencies

Before addressing the question of why MFE tends to be sensitive to a particular family of discrete frequencies, we consider the mirrored MFE as a spherical cavity for electromagnetic waves and analyse the stability of the modes. The MFM might be regarded as a cavity with a specific geometrical shape; a hypersphere. Therefore, it naturally has a sort of resonance frequencies. In any resonance cavity, internal reflections result in constructive and destructive interference. The interference leads to standing waves, but only for the specific set of frequencies which provide the proper relative phases: only these frequencies can survive destructive interference inside the cavity. In this way the cavity works as a sort of frequency filtering device. The spectrum of frequencies is determined by the geometrical features of the cavity and its boundary conditions, while the stability and the density of the modes dictated by the optical properties of the cavity, usually denoted as the fineness or quality factor. The quality factor for a Fisheye-like



(a) Standing fields at resonance frequency: The angular variable along the circle shows the position in the 1-D MFE. Vertical and horizontal axes shows scale of the amplitude of the EM field. Modes are excited externally without any planted source or drain.

(b) Standing fields at resonance frequency: In both figures (a) and (b), the angular variable along the circle shows the position in the 1-D MFE. Vertical and horizontal axes shows scale of the amplitude of the EM field. Running fields on the surface of MFE with planted source and drain at the off resonance frequency. The dashed green line denotes a source and the thick red line indicates the positioned drain at the antipodal.

FIGURE 6.1: A cross section of a  $S^2$  where waves propagating on the surface; geometry of a two-dimensional MFE

cavity has been calculated, and, MFE is known as one of the most stable types of cavity [95].

On the other hand, the method used to launch or excite the field might interrupt the geometrical feature of the cavity and thus inhibit the stability and spectrum of the field. In a closed spherical cavity like MFE in particular, implementing the source strongly influence stability of the spectrum. For example, a weak external excitation of the modes results in activating the natural resonance frequencies of the spherical cavity (Figure 6.1a), while an implantation of a single point source into the cavity (as in our model of the MFE), results in the opposite, forbidding natural resonance frequencies (Figure 6.1b). <sup>1</sup> The former creates a smooth standing wave while the later includes a singularity in boundary conditions.

To clarify this argument, first examine the 2-dimensional Fisheye-like media; but the same argument is applicable to higher dimensions. The 2-D Fisheye-like medium has a geometry equivalent to a sphere  $S^2$  (Figure 6.2). Symmetry and the conservation of momentum permit us to make an equatorial cross section cut on the  $S^2$  (Figure 6.1a) and restrict ourselves to one-dimension plane on propagation.

Consider the case of an ideal point dipole cable as a source located inside the medium. This introduces singularities which no monochromatic frequency of a resonance spectrum is

<sup>1</sup>Here, by external excitation we mean any method that does not change the structure of cavity—for example, launching the field by a metal tip or a fibre optic.

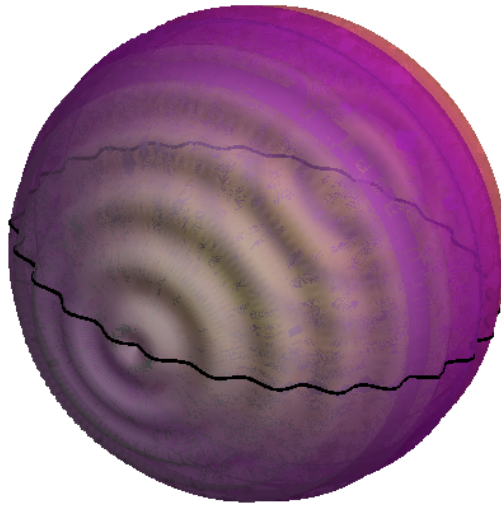


FIGURE 6.2: Running fields on the surface of  $S^2$  equivalent to 2-D Fisheye with planted source and drain at off-resonance frequency. Symmetry allows us to look at a cross section and write the equations in one variable,  $\phi$ .

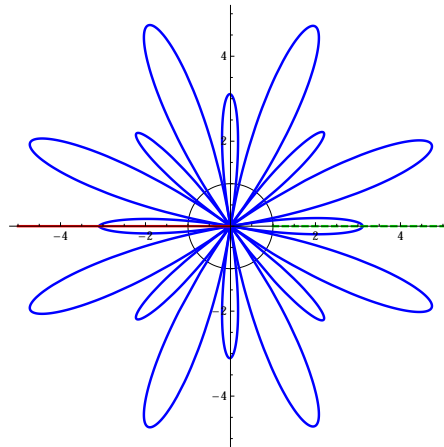


FIGURE 6.3: The angular variable along the circle shows the position in the 1-D MFE. Vertical and horizontal axes shows scale of the amplitude of the EM fieldRunning fields on the surface of 1-D Fisheye with planted source and drain near the resonance frequencies. The fields at resonance frequencies significantly exceed as expected from Leonhardt's solutions.

able to satisfy at the source point, except for catastrophic high intensity fields (Figure 6.3). The latter mathematically appear in Green's function of the MFE as a zero in the denominator:

$$\tilde{D} = \left(r' + \frac{1}{r'}\right) \frac{\sin(2\omega \operatorname{arccot}(r'))}{4(\pi)^2 \sin \pi \omega} \quad (6.1)$$

At resonance frequencies Green's function diverges, which physically results in the enormous buildup of energy.

However, by adding a non-ideal drain (as Miñano's experimental model suggests) at the antipodal point of the system and bringing into account its interaction with source, all frequencies can survive in the system in the form of running fields, without unphysical exposure of the amplitude at resonance Figures 6.1b and 6.3. In the rest of this chapter we provide a mathematical model for the above physical picture. Our mathematical model will help us to determine the crucial role of drain, and, more importantly the mutual interaction between source and drain which results in the stability of the system at resonance frequencies.

### 6.2.2 1-Dimensional MFE; Differential Model

In one dimension, the variable  $\phi$  denotes the position in the MFE. The differential equation of the total fields which propagate in the MFE with an internal source and a drain has the following general form:

$$\nabla^2 \varphi(\phi, t) - \frac{1}{c^2} \partial_t^2 \varphi(\phi, t) = \delta(\phi_s) \mathcal{J}_s(\phi, t) - \delta(\phi_d) \mathcal{J}_d(\phi, t) \quad (6.2)$$

Where  $\phi_s$  denotes the position of the source and  $\phi_d$  denotes the position of the drain, and  $\mathcal{J}_s$  and  $\mathcal{J}_d$  are the currents in the source and drain, respectively.

Equation 6.2 can be decomposed into two equations for mono-source and mono-drain. First, the MFE with a single planted source:

$$\nabla^2 \varphi_s(\phi, t) - \frac{1}{c^2} \partial_t^2 \varphi_s(\phi, t) = \delta(\phi_s) \mathcal{J}_s(\phi, t) \quad (6.3)$$

Second, the MFE with a single planted drain:

$$\nabla^2 \varphi_d(\phi, t) - \frac{1}{c^2} \partial_t^2 \varphi_d(\phi, t) = -\delta(\phi_d) \mathcal{J}_d(\phi, t) \quad (6.4)$$

In our argument, we assume the structural symmetry between source and drain: the drain is assumed to be time-reversed with respect to the source, so we can mathematically model both the same. The only difference is that the drain is passive—by which we mean that there is no external launching into the drain port. Thus Equation 6.4 becomes inhomogeneous only in the presence of an external field that launches through the source. This feature is modelled in the drain's current thus:

$$\mathcal{J}_d = \frac{1}{z_d} \varphi_s(\phi_d) \quad (6.5)$$

This equation implies that the current  $\mathcal{J}_d$  in the drain port is induced by the field of the source: the induced current in the drain  $\mathcal{J}_d$  is the response of the implanted cable to the source field at the antipodal point. To see how the real non-ideal drain in a closed

optical system like the MFE can couple to a source, we analyse the mathematical model of the imperfect drain and include the reflection of the field into our equations.

### 6.2.3 Imperfect drain

The first point we must make concerns sources and detectors. Finding a simple, practical model for detectors in the controversy on perfect imaging, has long been an outstanding problem [49, 68, 86–90]. Usually the source was assumed to be a predetermined current that generates electromagnetic waves and the detector was modelled as a drain. Active drains are produced by predetermined currents just like sources; passive drains are supposed to react to the incoming electromagnetic radiation and absorb it. In truth, both sources and detectors are neither fully active nor fully passive. A detector is a dynamical system responding to the electromagnetic field by absorbing radiation and then feeding energy back to the field: it is both passive and active. Also a realistic source is not simply a predetermined current that generates the field: the source must be able to receive radiation not captured by the detector because otherwise an equilibrium between in- and out-going radiation is impossible. The simplest source is an atom in an excited state emitting light; the simplest detector is an atom in the ground state absorbing light. In the experiment [2] the source was a cable from which microwave radiation was injected by a synthesiser, the detector was a cable connected to a vector analyser. Source and detector are essentially the same. What distinguishes them are the initial conditions: in a source, radiation is injected with a predetermined flux; in a detector radiation is not injected, although it could be, if, for example, the detecting atom were excited or the detector cable connected to a synthesiser. We thus need to consider sources and detectors as identical physical systems with different initial conditions. Previously we argued that a drain located at the antipodal position of the point source is an essential element in the MFE to complete the time-reversal symmetry of the system. There is another physical argument that describes the implementation of the drain: MFE is a closed optical system. Therefore, if we just implant an emitter as an ideal point source and no drain, radiation propagates through the medium and bounces from the (antipodal) image point back to the source. The phase difference between the source and image point is  $\phi = \pi k$ , where  $k$  stands for the wavelength in units of the Fisheye's radius [59]. Naturally, one can expect that after enough rounds only special frequencies remain due to destructive and constructive interferences. This may result in the build up of stored energy to infinity. However, the drain changes the geometry of the system. If it acts perfectly or, even adequately, the reflections will be insignificant: the build up of the stored energy will not be extreme, and we expect all the waves regardless of their frequency to pass through the MFE medium. Thus, while the existence of a drain in the system seems essential for proper functioning, its absorption need not be perfect.

We will see that a real physical drain can achieve the stability of the MFE at resonance frequencies.

A perfectly passive drain responds to excitations of the source with a relative phase. As we have seen, a solo wave equation for such a drain can be written:

$$(\Delta - \frac{\partial^2}{\partial t^2})\psi_d = -4\pi\delta(\vec{r} - \vec{r}')\mathcal{J}_d(\vec{r}, t). \quad (6.6)$$

$$\mathcal{J}_d = \frac{1}{Z_d}\psi_s(\vec{r} - \vec{r}') \quad (6.7)$$

Where  $\mathcal{J}$  is the time dependent current density in the cables (of the source or drain port), and  $d$  and  $s$  stand for drain and source respectively. Accordingly,  $\psi_d$  is a partial element of the field inside the lens associated with the excitation of the drain, and  $\psi_s(\vec{r} - \vec{r}')$  is the source field inside the lens. In general  $\mathcal{J}_d$  is defined by the response of the passive drain port with impedance  $Z_d$  to the external field of the source. In further discussions, we will assume that the source and the drain have identical structure that is, both source and drain are cable ports with the same impedance, diameter, and length. The perfect drain would be a passive drain planted into the system. Consider a pulse coming from an external source and reaching the drain at  $t_0$ :  $\mathcal{J}_d$  would turn on only for a short time interval around  $t_0$ . As the time approaches  $+\infty$ , the existing field  $\varphi_s$  can be assumed to be siphoned off by the drain [64]. If we define the perfect drain as a complete absorber, as we assumed in our initial model [16], then a non-ideal drain results in incomplete absorption and a nonzero reflection. In this case, we would have a flow of energy through the device from source to drain and back.

$$P_{total} = T + R, \quad (6.8)$$

where  $P$  is the total power emitted from the source (assuming the medium is not dissipative),  $T$  is the absorption at the drain, and  $R$  denotes the reflection of the source's field back into the lens with a corresponding phase shift. An imperfectly passive drain acts partially as a time-reversed source (swallows the source's field) and partially as a secondary source (reflecting parts of the field). This reflected field propagates toward the source and induces a secondary excitation of the source port.

#### 6.2.4 Mutual Relation Between Source and the Drain

Imperfection of the drain appears in the calculations by secondary a response of the source port to the reflected field:

$$\mathcal{J}_s(\phi_s, t) = \frac{1}{z_0}\mathcal{J}_0 e^{i\omega t} + \frac{1}{z_s}\varphi_d(\phi_s) \quad (6.9)$$

The total current in the source cable  $\mathcal{J}_s|_{\phi=\phi_s}$  consists of two parts, one from the external synthesizer  $\mathcal{J}_0$  and the other from the response to the reflected fields in the lens. Given that  $\varphi_d \propto \mathcal{J}_d$ , Equation 6.4 becomes:

$$\partial_\phi^2 \varphi_s(\phi) + \nu^2 \varphi_s(\phi) = -\delta(\phi_s) \left( \frac{1}{z_0} \mathcal{J}_0 + \frac{a}{z_s} \mathcal{J}_d \right) \quad (6.10)$$

The terms  $\mathcal{J}_0 e^{i\nu t}$  and  $z_0$  denote the external input current and the corresponding impedance respectively. The characteristic impedance of the source port,  $z_s$  is independent of the input power launched into the system: Characteristic impedance  $z_s$  depends only on the physical features of the source port (in our model, the height, diameter and material of the cable). Usually  $z_s$  is far larger than  $z_0$  and therefore the second term on the right hand side of Equation 6.10 will become significant only when the reflected field from drain port,  $\mathcal{J}_d(\vec{r}_s, t)$ , reaches the high values. As we consider drain to be good enough to absorb, but not perfect,  $\mathcal{J}_d(\vec{r}_s, t)$  will stay negligible except at resonance frequencies. In resonance frequencies, the enhancement of the drain field, switches on the the secondary emission and absorption at the source port. We might consider these mutually interacting source and drain as a dynamic drain. This dynamic response results in the finite distribution of energy at resonance frequencies, which permits those frequencies to stay inside the MFE medium. Our simulations show that the proper phase relation between the source, and the drain, and proper relative vales between the port's impedances, result in finite values for the field at resonance frequencies.

### 6.2.5 Field Solutions

Both figures 6.4 and 6.5 are based on the same Green's function equations:

$$\nabla^2 \varphi(\phi, t) - \frac{1}{c^2} \partial_t^2 \varphi(\phi, t) = -\delta(\phi) \delta(t) \quad (6.11)$$

After applying a Fourier transformation on the equation and choosing a proper unit ( $c = 1$ ) we have:

$$(\partial_\nu^2 + \nu^2) \varphi(\phi, \nu) = -\delta(\phi) \quad (6.12)$$

The general solution has the following form:

$$G^{(\pm)}(\phi, \tau) = \int_{-\infty}^{+\infty} G^{(\pm)}(\phi, \nu) e^{-i\nu\tau} d\nu \quad (6.13)$$

$$G^{(\pm)}(\phi, \nu) = \mathcal{A}^{(\pm)} e^{\pm i\nu\phi} \quad (6.14)$$

To adopt the analogy with time reversal imaging, we can carefully choose the solution. The boundary conditions on source and drain suggest choosing the retarded solution for the source and the advanced solution for the drain [64]. Choosing the retarded solution provides the causality condition discussed in [60]:

$$G^{(+)}(\phi, \tau) = \int_{-\infty}^{t_0} G^{(+)}(\phi, \nu) e^{-\nu t} d\nu = 0 \quad (6.15)$$

For the drain we choose the advanced solution as we demand the extraction of the field at the drain.

$$G^{(-)}(\phi, \tau) = \int_{t_0}^{+\infty} G^{(-)}(\phi, \nu) e^{-\nu t} d\nu = 0 \quad (6.16)$$

Boundary conditions on the source point,  $\phi_s = 0$ , and on the drain point,  $\phi_d = \pi$ , lead to:

$$G_s(\phi, t) = \mathcal{A}^{(+)} \cos(\nu(\pi - |\phi|)) e^{-\nu t} \quad (6.17)$$

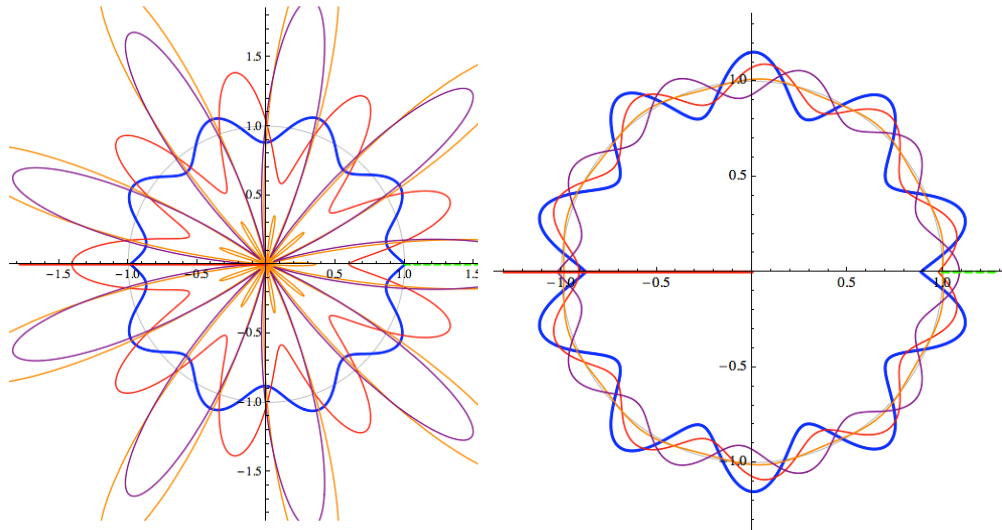
and

$$G_d(\phi, t) = \mathcal{A}^{(-)} \cos(\nu(\pi - |\phi - \pi|)) e^{-\nu t} \quad (6.18)$$

A drain (represented by the advanced solution) is a time reversal source that swallows the field. A perfect point drain swallows all the energy from the system, while an imperfect drain mainly absorbs but partially re-emits (reflects) the energy back into the lens. It is reasonable to assume the reflection is negligible except for resonance frequencies. The total solution for the fields in a single source-single drain MFE, aligned in antipodal position, would be the summation over both solutions:

$$\psi_{total}(\phi, t) = \int G_s^{(+)}(\phi, t; \phi', t') \mathcal{J}_s(\phi', t') d\phi' dt' + \int G_d^{(-)}(\phi, t; \phi'', t'') \mathcal{J}_d(\phi'', t'') d\phi'' dt'' \quad (6.19)$$

By substituting  $G_s^{(+)}$  and  $G_d^{(-)}$  from equations 6.17 and 6.18, and the corresponding currents from Equation 6.9, we can calculate the total field in the MFE lens as well as the currents in the cables. Methodologically, assuming a large value for  $z_s$  and therefore a negligible reaction of the source port to the drain field in off-resonance frequencies, we can calculate the field by recursive substitution. The final results simulated by Mathematica (Figure 6.4a) shows that the presence of source and drain together will change the boundary conditions. At resonance frequency, despite the exceeding high values of the individual elements of the field (source field, drain field, and secondary passive stimulation of the source), the total field remains finite and has a smooth flow from source to the drain (Figure 6.4a).



(A) At resonance frequency: Despite the exceedance by individual elements of the field, the total field remains finite and has a smooth flow from source toward drain.

(B) Off resonance frequency: Secondary excitation of the source (orange graph) has a negligible effect, as the field is not exceeding in off resonance frequencies.

FIGURE 6.4: A cross section of the MFE, including the source and an imperfect passive drain port. Red, purple and orange show the source field, drain field, and the passive stimulation of the source port respectively. Blue is the overall propagating field in the system.

### 6.3 1-Dimensional MFE; Matrix Model

In this section we focus on the injection and extraction of the field through the source and drain ports. We use the physics of the 1-dimensional MFE as described in section 6.1 but illustrate each port as a vertex and apply a matrix approach to calculate the transmission and reflection of the fields. We will see that assuming the interaction between source and drain can describe Miñano’s observations of the sub-wavelength focusing of the field. Let us consider the simplest case of perfect imaging, the 1-D sphere illustrated as a circle in Figure 6.5. Imagine that light is confined to a circle, say a fibre loop or ring resonator. Here light can go in only two directions, right or left. An “image” is formed when the two rays meeting have the same phase, which happens when both are antipodal. Light is coupled in and out of the circle by two 1-D channels that represent the source and the detector. These 1-D channels are idealisations of the cables used for injecting and extracting radiation in the simulation [1] and experiment [2]. Clearly, this 1-dimensional system represents a rather primitive model, but it does reproduce the findings of the experiment [2]: the model is simple, but not too simple.

We show how a point detector is able to sense minute displacements of a point source. Note that this is not imaging in the traditional sense of taking the image of a source

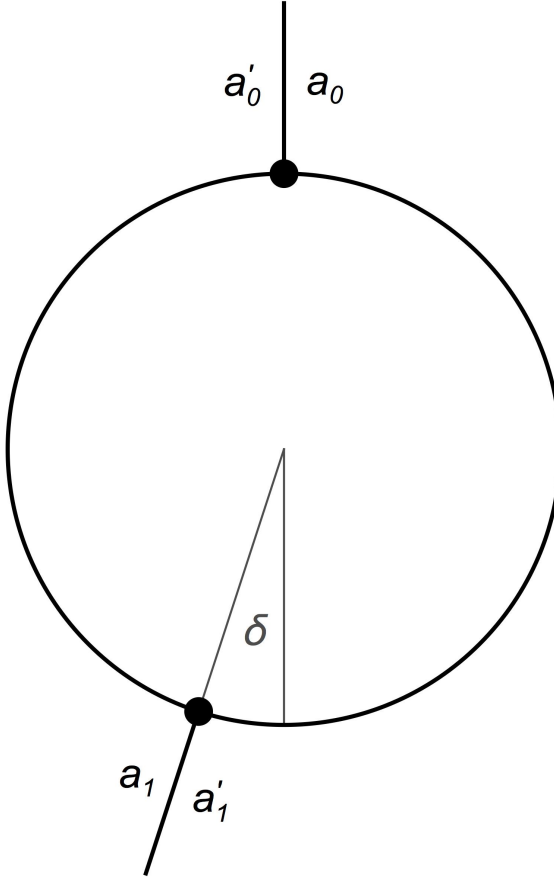


FIGURE 6.5: 1-dimensional model of a perfect-imaging device. The device is represented by a circle where light can propagate clockwise and counter-clockwise. Light is coupled in and out through one-dimensional channels that represent the source with in-coming amplitude  $a_0 = 1$  and the detector with  $a_1 = 0$ . A wave with amplitude  $a'_0$  is reflected back to the source and a wave with amplitude  $a'_1$  is detected. We calculate the transmission  $|a'_1|^2$  as a function of the wavenumber and the misalignment  $\delta$  between the actual detector position and the image of the source.

distribution all at once, but rather corresponds to scanning, as follows. Suppose that the detector is moved across the imaging region of the device. The detector would only produce a signal when it is close to the imaging point of the point source. The resolution is the distance from the actual imaging point where the detector begins to fire. We will show that, for light at the resonance frequency of the instrument, the resolution of the scan is infinitely fine. Well-known and widely-used examples of scanning methods that beat the diffraction limit are near-field scanning optical microscopy [96] and fluorescence microscopy [14]. In contrast to the former, here the detector is placed far away from the source; and in contrast to the latter, only linear optics are used. The idea of Miñano *et al.* [1] of turning an absolute optical instrument into a super resolving scanning device may thus find a place in the arsenal of methods for breaking the diffraction limit. Here we explain how it works.

### 6.3.1 Source and Drain as Coupling Vertices

Describing sources and detectors is particularly easy in our one-dimensional model: both are identical vertices where an external channel is connected to the circle (Figure 6.6). We model them as specific linear multi-ports [97, 98] using the following arguments.

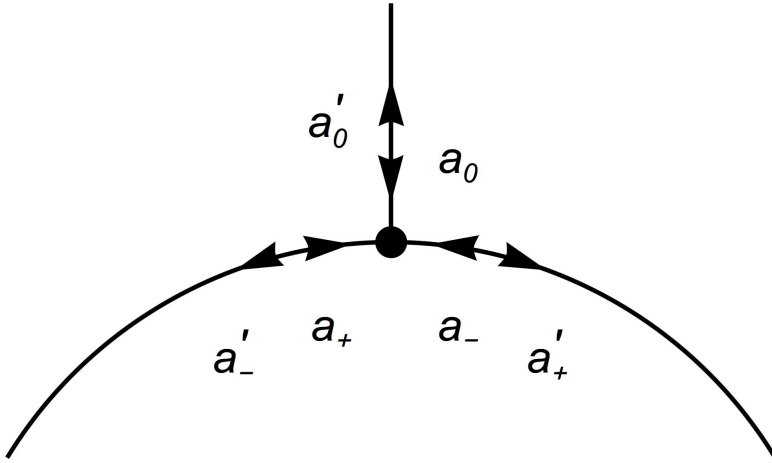


FIGURE 6.6: Coupling vertex. We model both source and detector as a linear coupler where a one-dimensional external channel interacts with the two modes in the device such that the amplitudes  $(a'_0, a'_+, a'_-)$  of the out-going waves are a linear transformation of the amplitudes  $(a_0, a_+, a_-)$  of the in-going waves.

Consider one vertex, the source. The vertex has three in-going modes: the mode incident through the external channel, and one clockwise- and one counter-clockwise-propagating mode. The vertex turns these three in-going modes into three out-going modes: it is a six-port. As the out-going radiation must be proportional to the in-going radiation, the six-port is constrained to be a linear device. We denote the complex amplitude of the incident radiation in the external channel by  $a_0$  and the amplitudes of the clockwise- and counter-clockwise-propagating waves in the circle by  $a_{\pm}$ ; together they constitute the amplitude vector  $\mathbf{a} = (a_0, a_+, a_-)^T$ . To denote the out-going modes we use primes:  $\mathbf{a}' = (a'_0, a'_+, a'_-)^T$ . We require that the vertex performs a linear transformation:

$$\mathbf{a}' = V \mathbf{a}. \quad (6.20)$$

As a consequence of energy conservation, a Hamiltonian for the mode transformation must exist, from which it follows that  $V$  is unitary [97]. In order to deduce the specific form of  $V$ , we make use of the semantics and symmetries of our system. At the source, light is coupled in with a certain efficiency and then distributed equally to the two waves in the device. At the detector, light is captured equally from the two waves and coupled out with a certain efficiency, assumed to be the same as for the source. Let us mentally separate the in- and out-coupling from the equal distribution and gathering, by writing

$V$  as

$$V = S T S^{-1} \quad (6.21)$$

with

$$S = \begin{pmatrix} 1 & 0 & 0 \\ 0 & 1/\sqrt{2} & 1/\sqrt{2} \\ 0 & 1/\sqrt{2} & -1/\sqrt{2} \end{pmatrix}. \quad (6.22)$$

The orthogonal matrix  $S$  describes the equal distribution of an amplitude from an intermediate channel to  $a_{\pm}$ . As intermediate channel we have chosen the second component of the amplitude vector. The  $1/\sqrt{2}$  terms guarantee that the sum of the intensities of the outgoing amplitudes is equal to the modulus squared of the initial amplitude. By the same token, the inverse matrix  $S^{-1}$  describes the equal gathering of the clockwise- and counter-clockwise-propagating waves. The intermediate channel is coupled to the external channel via the matrix  $T$  that depends on the coupling efficiency. We know that  $V$  must be unitary, so  $T$  should be a two-dimensional unitary transformation between the external and the intermediate channel. For simplicity, we assume  $T$  to be real. For perfect coupling  $T$  describes a flip between the two channels, for imperfect coupling an incomplete flip:

$$T = \begin{pmatrix} -\sin \alpha & \cos \alpha & 0 \\ \cos \alpha & \sin \alpha & 0 \\ 0 & 0 & 1 \end{pmatrix}. \quad (6.23)$$

The angle  $\alpha$  parameterizes the coupling efficiency; for  $\alpha = 0$  we get a perfect flip and hence perfect coupling, for general  $\alpha$  the cosine of  $\alpha$  describes the transmissivity  $\tau$  and  $\sin \alpha$  the reflectivity  $\rho$ . It turns out to be wise to parametrise the coupling as

$$g = \sqrt{2} \tan \left( \frac{\pi}{4} - \frac{\alpha}{2} \right) \quad (6.24)$$

where we get for the transmissivity and reflectivity

$$\tau = \cos \alpha = \frac{2\sqrt{2}g}{2+g^2}, \quad \rho = \sin \alpha = \frac{2-g^2}{2+g^2}. \quad (6.25)$$

In terms of  $g$  we find for the vertex matrix

$$V = \begin{pmatrix} \frac{g^2-2}{g^2+2} & \frac{2g}{g^2+2} & \frac{2g}{g^2+2} \\ \frac{2g}{g^2+2} & \frac{2}{g^2+2} & -\frac{g^2}{g^2+2} \\ \frac{2g}{g^2+2} & -\frac{g^2}{g^2+2} & \frac{2}{g^2+2} \end{pmatrix}. \quad (6.26)$$

The form (Equation 6.26) of the vertex matrix reveals an important property:  $V$  is symmetric,

$$V = V^T. \quad (6.27)$$

As  $V$  is an orthogonal matrix,  $V^T$  must be the inverse of  $V$ , and thus

$$V = V^{-1}. \quad (6.28)$$

The in-coupling vertex is also the out-coupling vertex: sources and detectors are fundamentally the same.

Let us briefly discuss two limiting cases,  $g = 0$  and  $g = \infty$ . For  $g = 0$  we obtain  $V = \text{diag}(-1, 1, 1)$ : the incident radiation is perfectly reflected with the reflected radiation changing sign, while the modes inside are not changed at all, but are shielded from the external channel. thus case  $g = 0$  corresponds to zero coupling where the vertex acts as a perfect mirror. For  $g = \infty$  we obtain

$$V = \begin{pmatrix} 1 & 0 & 0 \\ 0 & 0 & -1 \\ 0 & -1 & 0 \end{pmatrix}, \quad (6.29)$$

The incident field is also reflected, but without changing sign, while the waves inside the circle are reflected with change of sign: the case  $g = \infty$  describes a perfect scatterer. Perfect coupling corresponds to  $\alpha = 0$  and thus to  $g = \sqrt{2}$ . In order to find a direct interpretation for  $g$  we derive from Equations 6.20 and 6.26 the relations

$$a'_+ + a_- = a_+ + a'_-, \quad a_0 + a'_0 = g(a'_+ + a_-). \quad (6.30)$$

We may interpret relations 6.30 as conditions on the amplitudes of the fields and in this way obtain an interpretation for  $g$  as follows:

Consider the field in the circle around the source point. We chose the angle  $\vartheta$  as the coordinate around the circle, with the source sits at  $\vartheta = 0$ . The field oscillates  $\nu$  times along the circle,  $\nu$  corresponding to the wavenumber with respect to the angle  $\vartheta$ . If  $\nu$  is an integer the light is resonant. To the right of the source (Figure 6.6) the clockwise-propagating mode is outgoing with amplitude  $a'_+$  and the counter-clockwise mode is incident with amplitude  $a_-$ . To the left of the source the clockwise-propagating mode is incident with  $a_+$  and the counter-clockwise mode is outgoing with  $a'_-$ . Hence we can write the complex field  $\psi$  as

$$\psi = \begin{cases} a'_+ e^{i\nu\vartheta} + a_- e^{-i\nu\vartheta} & \text{for } \vartheta \geq 0, \\ a_+ e^{i\nu\vartheta} + a'_- e^{-i\nu\vartheta} & \text{for } \vartheta \leq 0. \end{cases} \quad (6.31)$$

Relations 6.30 show that the field is required to be continuous at the source. We also see that the intensity  $|a_0 + a'_0|^2$  in the external channel is  $g^2$  times larger than the field intensity inside. For example, for perfect in-coupling  $g = \sqrt{2}$ , so the incident channel must provide twice the intensity of the field inside, as one would expect, because the

incident radiation propagates away in two directions. The parameter  $g$  thus describes the ratio between external and coupled field amplitude, which is a useful parametrization of the coupling.

Having developed a simple model for both the source and the detector, we can now combine it with the propagation in the device (Figure 6.5). The detector is shifted by  $\delta$  from the antipodal position (it sits at  $\vartheta = \pi + \delta$  while the source sits at  $\vartheta = 0$ ). Waves propagating in the positive direction from the source thus experience a phase shift of  $\nu(\pi + \delta)$  followed by a phase shift of  $\nu(\pi - \delta)$  back to the source. For waves propagating in the negative direction the phase shift is  $\nu(\pi - \delta)$  followed by  $\nu(\pi + \delta)$ . The total phase of each round trip is  $2\pi\nu$ , a constant, which is the property of an absolute optical instrument [7, 17, 99] that we use. We describe the propagations with the help of the matrices

$$U_{\pm} = \begin{pmatrix} 1 & 0 & 0 \\ 0 & e^{i\nu(\pi \pm \delta)} & 0 \\ 0 & 0 & e^{i\nu(\pi \mp \delta)} \end{pmatrix}. \quad (6.32)$$

The light coupled in at the source propagates to the detector,

$$\begin{pmatrix} a'_0 \\ b_+ \\ b_- \end{pmatrix} = U_+ V \begin{pmatrix} a_0 \\ a_+ \\ a_- \end{pmatrix}, \quad (6.33)$$

where  $a'_0$  denotes the light reflected back to the source and  $b_{\pm}$  are the wave amplitudes incident at the detector. There the light is partly coupled out, with amplitude  $a'_1$ , and partly reflected back to the source,

$$\begin{pmatrix} a'_1 \\ a_+ \\ a_- \end{pmatrix} = U_- V \begin{pmatrix} a_1 \\ b_+ \\ b_- \end{pmatrix}. \quad (6.34)$$

We require that light with unity amplitude be incident at the source and that no light enters through the detector,

$$a_0 = 1, \quad a_1 = 0. \quad (6.35)$$

The transmission coefficient  $t$  is given by

$$t = |a'_1|^2. \quad (6.36)$$

### 6.3.2 Sub-wavelength Focusing of The Field

Equations 6.33-6.35 with definitions 6.26 and 6.32 establish six inhomogeneous linear equations for the six variables  $a_{\pm}$ ,  $b_{\pm}$ ,  $a'_0$  and  $a'_1$  with a unique solution. Solving this

system we obtain for the transmission coefficient

$$t = \frac{16g^4 \cos^2 \nu \delta \sin^2 \nu \pi}{4g^4 \sin^2 2\nu\pi + ((g^4 + 4) \sin^2 \nu \pi - g^4 \sin^2 \nu \delta)^2}. \quad (6.37)$$

Figure 6.7 shows the transmission as a function of  $\nu$  for various coupling strengths  $g$  and offsets  $\delta$ . Let us discuss the most relevant limiting cases. For perfect alignment,  $\delta = 0$ , we obtain from our result 6.37

$$t_0 \equiv t|_{\delta=0} = \frac{16g^4}{16g^4 + (g^4 - 4)^2 \sin^2 \nu \pi}. \quad (6.38)$$

For perfect alignment the transmission is periodic in  $\nu$ , it reaches unity at resonance where  $\nu$  is an integer, and we obtain for the integral

$$T = \int_0^1 t_0 \, d\nu = \frac{4g^2}{4 + g^4}. \quad (6.39)$$

For perfect coupling,  $g = \sqrt{2}$ , and the transmission 6.38 is unity for all  $\nu$ ; but for different coupling parameters the total transmission 6.39 lies below unity. The device behaves like a typical Fabry-Perot resonator [7]: it spectrally distributes the transmission such that at resonance it always reaches unity. This Fabry-Perot feature of the device is completely expected. The surprising feature of the perfect-imaging device appears for  $\delta \neq 0$ , where source and detector are misaligned. We see from our result 6.37 that

$$t = 0 \quad \text{for } \delta \neq 0 \text{ and } \nu \in \mathbb{N}. \quad (6.40)$$

Exactly at resonance, the Fabry-Perot transmission curve drops to zero for  $\delta \neq 0$ . To deduce a measure for the width of the dip we calculate the second derivative of  $t$  at the resonance (the first derivative vanishes, as zero is obviously a minimum of  $t = |a_1|^2$ ). We find

$$\frac{1}{2} \frac{\partial^2 t}{\partial \nu^2} \Big|_{\nu \in \mathbb{N}} = \frac{16 \pi^2 \cos^2 \nu \delta}{g^4 \sin^4 \nu \delta} \sim \frac{\pi^2}{(g\nu\delta/2)^4} \quad \text{for small } \delta \neq 0. \quad (6.41)$$

The smaller the displacement  $\delta$  of the detector, the sharper the dip. However, regardless how small the displacement, a step change occurs at resonance between alignment and displacement. This ultrasensitive behaviour can be used to measure, with a fixed detector, small displacements of the source, as only the relative angle between source and detector matters. Whether or not our model is of direct practical relevance, it represents the simplest toy model for super-resolution in absolute optical instruments. The diffraction limit of imaging [7] would suggest a resolution of  $\nu\delta/2 \sim 1$ : here the resolution is in principle unlimited for a finite wavenumber. Miñano *et al.* observed the characteristic transmission dips for a two-dimensional system in a computer simulation [1] and then experimentally [2]; we will call them *Miñano dips*. Here we have captured

this characteristic feature in a simple formula<sup>2</sup>.

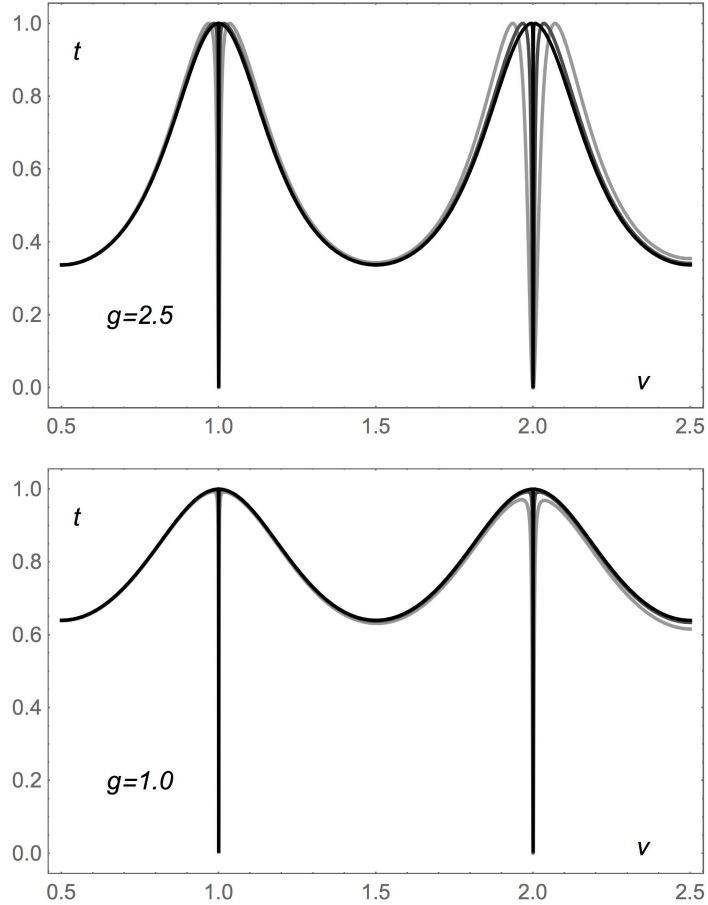


FIGURE 6.7: Transmission through the device. We plot the transmission  $t$  from 6.37 as a function of wavenumber  $\nu$  and for various displacements  $\delta$  (light grey:  $\delta = 0.1$ , grey:  $\delta = 0.05$ , black:  $\delta = 0.01$ ). The transmission curves follow Fabry-Perot resonances that depend on the coupling coefficient  $g$ . Near the resonances where  $\nu$  is an integer, the transmission sharply drops to zero. The smaller the displacement the narrower the dip, as described by Equation 6.41. At exact resonance, the transmission changes abruptly between 0 for  $\delta \neq 0$  and 1 for  $\delta = 0$ .

Moreover, using our simple one-dimensional model for perfect imaging, we can also identify the physical mechanism behind the Miñano dips. At resonance and for misaligned source and detector, the incident radiation would buildup an infinite field inside the device unless, in the stationary regime, it is prevented from entering. For  $\delta \neq 0$  and  $\nu \in \mathbb{N}$  we obtain from the solution of Equations 6.33–6.35:

$$a_+ = a'_+ = a_-^* = a'^*_- = \frac{i e^{-i\nu\delta}}{g \sin \nu\delta}, \quad a'_0 = 1, \quad a_1 = 0. \quad (6.42)$$

---

<sup>2</sup>In practice [1, 2] the Miñano dips were shifted by about  $10^{-3}$  with respect to the exact resonance, which is presumably due to the finite size of the sources and detectors used.

With these coefficients we obtain for the field 6.31

$$\psi = \frac{2 \sin [\nu(\delta - \vartheta)]}{g \sin \nu \delta}. \quad (6.43)$$

The incident radiation is reflected, without changing sign, while a standing wave with finite amplitude is formed inside the device. The incident plus the reflected amplitude amounts to  $a_0 + a'_0 = 2$ , which, according to relations 6.30, is  $g$  times the field amplitude  $\psi(0)$  at the source, as 6.43 shows. Similarly, the standing wave described by 6.43 has a node at the detector, where the total out-coupled field  $a_1 + a'_1$  is zero. We thus see how for  $\delta \neq 0$  the standing wave formed inside the device adjusts itself at equilibrium such that further radiation is prevented from entering, which reduces the transmission to zero, causing the characteristic Miñano dips.

Now consider the case of perfect alignment,  $\delta = 0$ . We obtain from the solution of Equations 6.33–6.35 the amplitudes

$$\begin{aligned} a_+ &= a_- = \frac{\tau}{\sqrt{2}} e^{2i\nu\pi} \rho \eta \quad , \quad a'_+ = a'_- = \frac{\tau}{\sqrt{2}} \eta, \\ a'_0 &= (e^{2i\nu\pi} - 1) \rho \eta \quad , \quad a'_1 = \tau^2 e^{i\nu\pi} \eta \end{aligned} \quad (6.44)$$

in terms of the reflectivity  $\rho$  and transmissivity  $\tau$  according to Equation 6.25 and the coefficient  $\eta$  describing Fabry-Perot multiple reflections:

$$\eta = \frac{1}{1 - e^{2i\nu\pi} \rho^2} = \sum_{m=0}^{\infty} e^{2mi\nu\pi} \rho^{2m}. \quad (6.45)$$

The total transmission 6.39 we can understand as  $\tau^4 \sum_{m=0}^{\infty} \rho^{4m}$ , the product of the transmissions  $\tau^2$  at source and detector times the multiple reflections in the device. We get for the field 6.31

$$\psi = \frac{\tau}{\sqrt{2}} \left( e^{i\nu|\vartheta|} + e^{2i\nu\pi} \rho e^{-i\nu|\vartheta|} \right) \eta. \quad (6.46)$$

The  $\exp(i\nu|\vartheta|)$  and  $\exp(-i\nu|\vartheta|)$  are the Green's functions of wave propagation with two sources, one at  $\vartheta = 0$  and one at  $\vartheta = \pi$ , describing waves running from source to detector and vice versa. The field thus consists of running waves (and their multiple reflections). No standing wave is formed, because it does not need to be formed: for perfect alignment the radiation can run through the device; it is not accumulated at resonance. In the case of perfect coupling we get

$$\psi = \frac{e^{i\nu|\vartheta|}}{\sqrt{2}}, \quad (6.47)$$

which is the one-dimensional equivalent of the propagating wave in the Maxwell Fisheye that performs perfect imaging [16]. The amplitude is reduced by  $\sqrt{2}$  because the incident radiation is distributed into two partial waves, one running to the right and the other to the left.

To summarise, we have developed a simple one-dimensional model for super-resolution in absolute optical instruments that has allowed us to describe the interplay between source and detector. The key innovation of our model is the description of sources and detectors as linear dynamical systems. We used a simple one-dimensional model that we believe can be extended to two- or three-dimensional systems. Our model has captured some of the most characteristic features of super-resolution with positive refraction: we have found analytic expressions for the Miñano dips [1, 2] and their physical explanation.



## Chapter 7

# The Interacting Sources and Directors; A Lagrangian Model

### 7.1 Model

In this chapter, we extend our Lagrangian model from Chapter 6 to the higher dimension. Our aim is to investigate the role of interacting sources and detectors in perfect imaging. We establish limitations and possibilities that arise from interactions and resonances Figure 7.2 and what mutually interacting detectors do. As we will show, an array of detectors can image a point source with arbitrary precision and a single detector can scan an array of near-field sources from a far-field distance with perfect fidelity. However, for this the radiation has to be at resonance and the number of detectors or sources must not exceed the number of waves.

#### 7.1.1 Lagrangian

Consider the electromagnetic field in both the device and the cables. The field shall be polarized such that only one component  $A$  of the vector potential is relevant. We describe the field dynamics by the Lagrangian density,

$$\mathcal{L} = \mathcal{L}_0 + \sum_m \mathcal{L}_m, \quad (7.1)$$

that consisting of the Lagrangian density  $\mathcal{L}_0$  of the field inside the device,

$$\mathcal{L}_0 = \frac{1}{2} \left( n^2 (\partial_t A)^2 - (\nabla A)^2 \right), \quad (7.2)$$

and the Lagrangian densities  $\mathcal{L}_m$  of the field in the cables and their interaction at their ports of entry to the device:

$$\mathcal{L}_m = \frac{1}{2} \left( (\partial_t A)^2 - (\partial_m A)^2 \right) - gA (\partial_m A) \delta(z - z_m). \quad (7.3)$$

Here  $n$  denotes the refractive-index profile in the device. The refractive index profile of MFE written in complex variables, reads:

$$n = \frac{2}{1 + |z|^2}. \quad (7.4)$$

We consider wave propagation in two-dimensional space described by the complex coordinate  $z = x + iy$  on the Cartesian  $(x, y)$  plane. The wave propagation with refractive-index profile Equation 7.4 is equivalent [35] to the free wave propagation on the unit sphere  $(X, Y, Z) = (\sin \theta \cos \phi, \sin \theta \sin \phi, \cos \theta)$ . Both are related to each other by stereographic projection Figure 7.1:

$$z = \frac{X + iY}{1 - Z} = e^{i\phi} \cot \frac{\theta}{2}. \quad (7.5)$$

In the language of transformation optics [35], the unit sphere represents virtual space and the plane with the profile of Equation 7.4 the physical space. We shall mentally switch between the two pictures whenever one is more convenient than the other. As the unit of length we take the radius of the device, and as the unit of time the round-trip duration divided by  $2\pi$ .

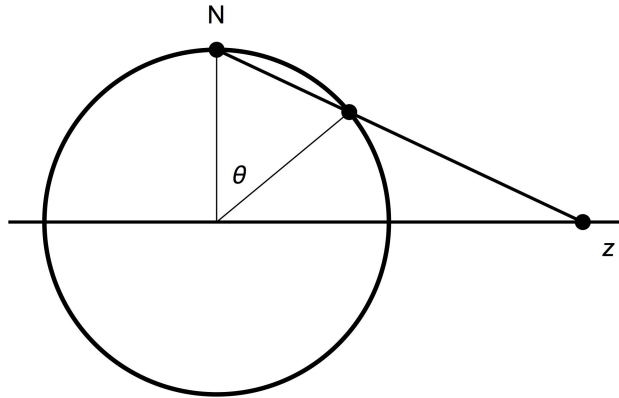


FIGURE 7.1: Stereographic projection. The plane of the MFE is the stereographic projection of the surface of the sphere (shown in a cut). Experiments [5, 8] in the  $z$ -plane with the refractive index profile of Equation 7.4 are equivalent to experiments [2] on the sphere with  $n = 1$ .

In the model of the field in the cables, Equation 7.3, we assume that the field  $A$  inside the device extends to the cables. The cables are idealized as one-dimensional: the propagation coordinate along the  $m$ -th cable we denote by  $s_m$ ; the derivative with

respect to  $s_m$  by  $\partial_m$ ; the port of entrance we put at  $s_m = 0$ . For the interaction term  $gA(\partial_mA)\delta(z - z_m)$  we have assumed that the flux of the field in the cable,  $\partial_mA$ , generates with coupling strength  $g$  a current  $j$  localized at the port of entrance. The current interacts with the field according to the standard electromagnetic coupling  $jA$  in Lagrangian density [91]. In short, we have assumed the cables act as point antennas.

### 7.1.2 Field Equations

Having established the Lagrangian, we obtain the field equations from the Euler–Lagrange equation [91]. We separate them into the field equation inside the device and the field equation in the cables:

$$(n^2\partial_t^2 - \nabla^2) A = -g \sum_m (\partial_mA) \delta(z - z_m), \quad (7.6)$$

$$(\partial_t^2 - \partial_m^2) A = gA(z_m) \partial_m \delta(s_m). \quad (7.7)$$

For the field equation in the cables we have read  $\delta(z - z_m)$  from the perspective of the cables, *i.e.* as  $\delta(s_m)$ . As we consider an equilibrium of the radiation in the device and the cables, we write  $A$  as a monochromatic field oscillating with circular frequency  $k$  (that, thanks to our choice of units, agrees with the free-space wavenumber). Furthermore, we decompose the field into a stationary component  $\Psi$  in the device and the components  $\chi_m$  in the cables:

$$A = (\Psi + \sum_m \chi_m) e^{-ikt}. \quad (7.8)$$

We obtain from Equations 7.6 and 7.7 the stationary wave equations

$$(\nabla^2 + n^2 k^2) \Psi = g \sum_m (\partial_m \chi_m) \delta(z - z_m), \quad (7.9)$$

$$(\partial_m^2 + k^2) \chi_m = -g\Psi(z_m) \partial_m \delta(s_m). \quad (7.10)$$

In the cables we have the oscillatory solutions

$$\chi_m = \begin{cases} a_m e^{iks_m} + a'_m e^{-iks_m} & : s_m \leq 0 \\ 0 & : \text{elsewhere.} \end{cases} \quad (7.11)$$

The coefficients  $a_m$  describe the incoming amplitudes, and the coefficients  $a'_m$  the outgoing amplitudes. For a drain representing a detector, the incoming amplitude  $a_m$  is zero.

### 7.1.3 Consistency with Our One-Dimensional Model

Let us briefly compare our Lagrangian theory with the one-dimensional model of sources and drains developed earlier [3]. Here we assume  $n = 1$ . Consider one port at position  $z = 0$ , with the wave amplitudes  $a = a_m$  and  $a' = a'_m$  in the cable. In one dimension, we can write the solution of the wave Equation 7.9 as

$$\Psi = \begin{cases} a'_+ e^{ikz} + a_- e^{-ikz} & : z > 0 \\ a_+ e^{ikz} + a'_- e^{-ikz} & : z < 0. \end{cases} \quad (7.12)$$

The  $a_{\pm}$  describe the incoming waves at the port from within the device, the  $a'_{\pm}$  the corresponding outgoing waves. We obtain from Equations 7.9 and 7.10:

$$\begin{aligned} a'_+ + a_- &= a_+ + a'_-, \\ a'_+ - a_- - a_+ + a'_- &= g(a - a'), \\ a + a' &= g(a'_+ + a_-). \end{aligned} \quad (7.13)$$

These relations constitute a system of three linear equations for the outgoing amplitudes in terms of the ingoing ones. Its solution agrees with Equation (7) of Ref. [3], which proves that our Lagrangian theory reproduces the one-dimensional model that has explained the experimental data [2].

### 7.1.4 Green's Function

Having confirmed the validity of our Lagrangian in the case of one-dimensional propagation, we return to the case of two-dimensional imaging. We obtain from Equation 7.10 for the amplitudes  $a_m$  and  $a'_m$  of Equation 7.11

$$a_m + a'_m = g\Psi(z_m). \quad (7.14)$$

We assume that the field in the device is only generated through the cables; there is no initial field remaining inside. Then we can write the solution of the wave equation Equation 7.9 in terms of the Green's function  $G(z, z_0)$  as

$$\Psi = ikg \sum_m G(z, z_m) (a_m - a'_m). \quad (7.15)$$

For the MFE and, equivalently, the surface of the sphere, the Green's function is given by the expression [81]

$$G = \frac{P_\nu(\zeta_m)}{4 \sin \nu \pi} \quad (7.16)$$

in terms of the Legendre function  $P_\nu$  [100] with index

$$\nu = \frac{1}{2} \left( \sqrt{4k^2 + 1} - 1 \right). \quad (7.17)$$

At resonances the  $\nu$  is integer; the resonances correspond to the standing waves on the surface of the sphere. The  $\zeta_m$  depend on the coordinate  $z$  and the position  $z_m$  of the  $m$ -the port [81]:

$$\zeta_m = \frac{|z'|^2 - 1}{|z'|^2 + 1}, \quad z' = \frac{z - z_m}{z_m^* z + 1}. \quad (7.18)$$

If the Fisheye is surrounded by a mirror at  $|z| = 1$ , the stereographic projection of the equator of the sphere, we need to use Green's function [16, 81]

$$G' = G(z, z_0) - G(1/z^*, z_0). \quad (7.19)$$

The mirror makes the Maxwell Fisheye practical in application, because it confines the refractive-index profile of Equation 7.4 within  $|z| \leq 1$  where the refractive index varies maximally by a factor of two. Here we are primarily interested in the fundamental capabilities and limitations of perfect imaging with interacting sources and drains, and so we only consider Maxwell's archetype with Green's function Equation 7.16, but our results are easily generalizable.

Note that near a port Green's function must diverge logarithmically [16], because the port acts as a delta-function source for a two-dimensional wave. For the Maxwell Fisheye we obtain for  $z \sim z_m$  where  $\zeta_m \sim -1$  the asymptotics

$$G \sim \frac{1}{4\pi} \left[ \ln \left( \frac{\zeta_m + 1}{2} \right) + 2\gamma + 2\psi(\nu + 1) + \pi \cot \nu\pi \right] \quad (7.20)$$

where  $\gamma$  denotes Euler's constant and  $\psi$  the digamma function [100]. The logarithmic divergence is a consequence of the mismatch dimensionality between the device and the cables taking radiation in and out — two-dimensional radiation originates or disappears at the ports of entry of one-dimensional cables. In practice, we would regularize the divergence, requiring, for example, that the cables have a small but finite diameter. However, in this paper we are mostly concerned with the behaviour of the system near a resonance where  $\nu$  tends to an integer. Here the  $\cot \nu\pi$  term in Equation 7.20 dominates over the logarithmic term if the latter is regularized. We regard the logarithm as a good approximation for a constant, and use simply

$$G \sim \frac{\cot \nu\pi}{4}. \quad (7.21)$$

Now we are prepared to tackle the problem of perfect imaging in the MFE with mutually interacting sources and drains.

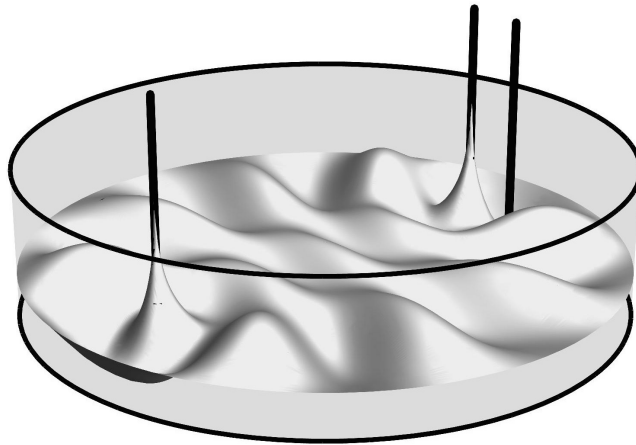


FIGURE 7.2: Scheme: absolute optical instrument with mutually interacting sources and drains. Radiation enters and leaves the device via cables that act as sources and drains. The instrument shown is Maxwell's fish eye [46] surrounded by a mirror [16]. In the figure one source faces two drains. Only the drain opposite to the source couples the radiation out, the other does not transmit. In this case the two drains resolve the position of the source. The roles of sources and drains may be reversed: the figure may also represent two sources scanned by one movable drain. Only when the drain is at the image position of one of the sources it transmits, even if the sources were much closer than the wavelength, provided the radiation is resonant.

## 7.2 Analysis

### 7.2.1 Scattering Matrix

The amplitudes  $a_m$  describe the incoming waves at the ports, and the  $a'_m$  the outgoing waves. We wish to relate the vectors  $\mathbf{a}$  and  $\mathbf{a}'$  of the  $a_m$  and  $a'_m$  as

$$\mathbf{a}' = S\mathbf{a} \quad (7.22)$$

where  $S$  denotes the scattering matrix. We notice that Equation 7.14 and Equation 7.15 at  $z = z_l$  establish a closed system of linear equations for  $a'_m$ . The solution is going to be of the form of Equation 7.22 and, therefore, will give the scattering matrix. Equation 7.15 at  $z = z_l$  depends on Green's function, Equation 7.16 at  $\zeta_{ml} = \zeta_m(z_l) = \zeta_{lm}$ . Note that  $\zeta_{ml}$  becomes  $-1$  for  $l = m$  (the port interacting with itself) where Green's function diverges, unless it is regularized. In this case we use the asymptotic of Equation 7.21 for Green's function.

It is convenient to express the linear system of Equation 7.14 and Equation 6.31 at  $z = z_l$  in terms of the matrix

$$W_{ml} = \begin{cases} \cos \nu\pi - i\sigma \sin \nu\pi & : l = m \\ P_\nu(\zeta_{ml}) & : l \neq m \end{cases} \quad (7.23)$$

with the parameter

$$\sigma = \frac{4}{g^2 k}. \quad (7.24)$$

We see that the linear system appears as

$$W\mathbf{a}' = W^*\mathbf{a}, \quad (7.25)$$

and hence

$$S = W^{-1}W^*. \quad (7.26)$$

As the scattering matrix is given by the ratio between  $W^*$  and  $W$ , it crucially depends on the imaginary part of  $W$ . We see from Equation 7.23 that

$$W = V - i\sigma \sin \nu\pi \mathbb{1}, \quad V = W|_{\sigma=0} \quad (7.27)$$

where  $V$  is a real matrix. At a resonance where  $\nu \in \mathbb{N}$  the imaginary part vanishes;  $S = \mathbb{1}$  if  $\det V \neq 0$ , which means the outgoing radiation is equal to the incoming radiation — the device rejects all incident waves and reflects them. However, in the case of imaging,  $\det V$  vanishes, and so in the limit as  $\nu \rightarrow$  integer it is behaviour becomes complicated. Near a resonance, the calculation of the scattering matrix becomes numerically delicate. It is advisable to compute  $S$  with the help of the eigenvalues and eigenvectors of  $V$ . We see from Equation 7.18, Equation 7.23 and Equation 7.27 that  $V$  is a symmetric real matrix. Hence  $V$  has real eigenvalues  $V_m$  and an orthogonal system of eigenvectors. We express  $V$  as

$$V = R^T \text{diag}(V_m)R \quad (7.28)$$

in terms of the rotation matrix  $R$  of the normalized eigenvectors. From Equation 7.27 follows

$$W = R^T \text{diag}(W_m)R \quad (7.29)$$

with the eigenvalues

$$W_m = V_m - i\sigma \sin \nu\pi. \quad (7.30)$$

Since  $R$  is real, we obtain from Equation 7.26 for the scattering matrix

$$S = R^T \text{diag}(W_m^*/W_m)R, \quad (7.31)$$

which is a numerically more stable expression than Equation 7.26, although it may still require high-precision arithmetics near a resonance. We also see from Equation 7.31 that  $S$  is unitary, as one would expect: we are considering a passive device where the total intensity is conserved,  $\mathbf{a}'^* \cdot \mathbf{a}' = \mathbf{a}^* \cdot \mathbf{a}$ . Furthermore, we see from Equation 7.31 that  $S^{-1} = S^*$  and get from the unitarity  $S = S^T$ : the scattering matrix is symmetric.

### 7.2.2 Single Source, Single Drain

Consider the case [1, 2] in which a single source faces a moveable single detector Equation 7.3. Without loss of generality, we put the source at the south pole of the sphere ( $\theta_1 = \pi$ ) and the drain at an angle  $\delta$  away from the north pole ( $\theta_2 = \delta, \phi_2 = 0$ ). For simplicity, we only consider the wave propagation along the circle  $\phi = 0$  where, according to Equation 7.5 and Equation 7.18,

$$\zeta_m = -\cos(\theta - \theta_m). \quad (7.32)$$

Requiring  $a_1 = 1$  (unit source) and  $a_2 = 0$  (drain) we obtain from the solution of the linear system of Equation 7.25 with matrix  $W$  defined in Equation 7.23

$$\begin{aligned} a'_1 &= \frac{P_\nu(\cos \delta)^2 - \cos^2 \nu \pi - \sigma^2 \sin^2 \nu \pi}{P_\nu(\cos \delta)^2 - (\cos \nu \pi - i\sigma \sin \nu \pi)^2}, \\ a'_2 &= \frac{2i\sigma \sin \nu \pi P_\nu(\cos \delta)}{P_\nu(\cos \delta)^2 - (\cos \nu \pi - i\sigma \sin \nu \pi)^2}. \end{aligned} \quad (7.33)$$

The intensity  $|a'_2|^2$  describes the transmission of the device through the detector port. We see that  $a'_2$  vanishes at resonance where  $\nu \in \mathbb{N}$ , unless  $\delta = 0$ . The transmission shows the Miñano dips [1, 2] characteristic of scanning in absolute optical instruments [3]: when the radiation is resonant, a displacement of the detector, however small, will extinguish the transmission; the incident radiation is completely reflected. For  $\delta = 0$ , on the other hand,  $a'_2$  tends to  $(-1)^\nu$  at resonance: for perfect alignment of source and drain all incident radiation is transmitted. This on-off behaviour may be useful in scanning a single source with arbitrary precision from some distance away.

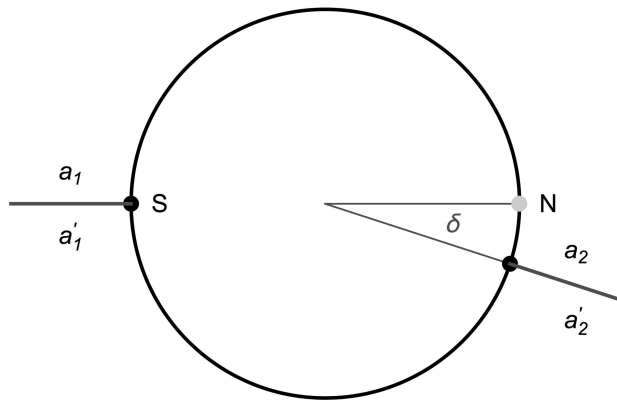


FIGURE 7.3: Single source, single drain — the setup of experiment [2]. Radiation incident at the source S is scanned with a mobile drain an angle  $\delta$  away from N (we rotated the sphere of Figure 7.1).

Figure 7.4 shows the transmission versus wave index  $\nu$ . The figure agrees well with the transmission curve of the simple one-dimensional model [3] and with experiment [2],

apart from a tiny shift of the resonance frequencies that is probably due to the finite sizes of the source and drain. The Miñano dips are narrow features in the transmission curve; we characterize their width by

$$\frac{1}{2} \left. \frac{\partial^2 |a'_2|^2}{\partial \nu^2} \right|_{\nu \in \mathbb{N}} = \left( \frac{2\pi\sigma P_\nu(\cos \delta)}{P_\nu(\cos \delta)^2 - 1} \right)^2 \quad (7.34)$$

that scales like  $\delta^{-4}$  for small  $\delta$ . Minute deviations of the drain are detectable near resonance.

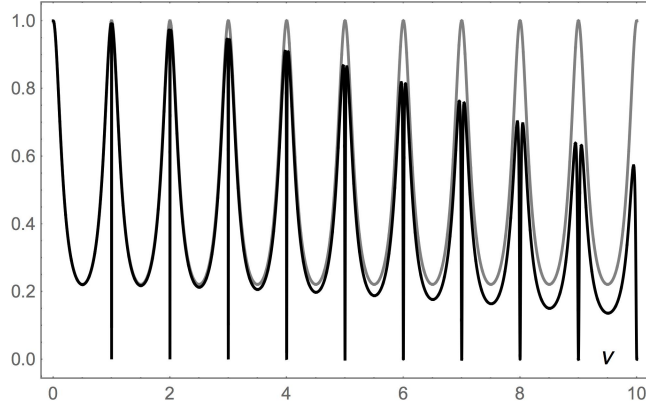


FIGURE 7.4: Miñano dips with the setup of Figure 7.3. Transmission of a single source through the MFE to a single drain;  $|a'_2|^2$  of Equation 7.33 plotted as a function of  $\nu$ . Black curve: the drain is misaligned by the angle  $\delta = 0.1$ . Grey curve:  $\delta = 0$ , and the drain is at the correct imaging position. In both cases we take  $\sigma = 4.0$ . The figure shows the typical Fabry-Perot resonances of the device, but also, for the misaligned drain, sharp drops at the resonances ( $\nu \in \mathbb{N}$ ).

Consider the case of perfect alignment of source and drain,  $\delta = 0$ , for variable  $\nu$ . We obtain from Equation 7.33

$$|a'_2|^2 = \frac{1}{\cos^2 \nu \pi + T^{-2} \sin^2 \nu \pi}, \quad T = \frac{2}{\sigma + \sigma^{-1}}. \quad (7.35)$$

The device behaves like a typical Fabry-Perot resonator with average transmission

$$\int_m^{m+1} |a'_2|^2 d\nu = T. \quad (7.36)$$

At resonance, it transmits perfectly. Out of resonance, the transmission is reduced due to coupling losses, unless  $\sigma = 1$ , which we regard as the case of perfect coupling.

Finally, we calculate the field  $\Psi$  for the case of perfect alignment. We obtain from Equations 7.15, 7.16 and 7.33 for  $\delta = 0$  the field

$$\Psi = \frac{i\sqrt{k}}{\pi} \tau \eta e^{i\nu\pi} [Q_\nu(\zeta) + \rho e^{i\nu\pi} Q_\nu(-\zeta)] \quad (7.37)$$

in terms of the Legendre functions  $Q_\nu$  (defined on the branch cut [100]):

$$Q_\nu(\zeta) = \frac{\pi}{2} \frac{e^{-i\nu\pi} P_\nu(\zeta) - P_\nu(-\zeta)}{\sin \nu\pi} \quad (7.38)$$

and the coefficients

$$\begin{aligned} \tau &= \frac{2\sqrt{\sigma}}{\sigma + 1}, \\ \rho &= \frac{\sigma - 1}{\sigma + 1}, \\ \eta &= \frac{1}{1 - e^{2i\nu\pi}\rho^2}. \end{aligned} \quad (7.39)$$

Note that  $e^{i\nu\pi}Q_\nu(\zeta)$  describes a running wave from the source to the drain [16];  $Q_\nu(-\zeta)$  corresponds to a wave running back from the drain to the source. Note also that  $Q_\nu$  is well-behaved for  $\nu \rightarrow$  integer. We interpret  $\tau$  and  $\rho$  as the transmission and reflection coefficients of the ports, with  $\tau^2 + \rho^2 = 1$ . The factor  $\eta$  sums up the geometric series

$$\eta = \sum_{m=0}^{\infty} e^{2im\nu\pi} \rho^{2m} \quad (7.40)$$

of all the reflections and phase factors during the roundtrips in the device. The field of Equation 7.37 thus describes the characteristic behavior of a wave injected with transmittance  $\tau$  that accumulates a phase shift of  $\nu\pi$  from source to drain, is reflected with reflectance  $\rho$ , gains the phase factor  $\nu\pi$  from drain to source, where it is reflected again etc., until it is recorded at the drain. In the case of perfect coupling, we obtain the sole running wave  $e^{i\nu\pi}Q_\nu(\zeta)$  characteristic of perfect imaging in the two-dimensional MFE [16].

### 7.2.3 Single Source, Multiple Drains

In Sec. III B we investigated in detail a single source observed with a single, movable detector in the MFE. Imagine now that the source faces an array of  $M$  detectors: the source we place at port 1, the drains at the remaining ports. Consider the field  $\Psi$  given by Equation 7.15 close to a resonance where we might expect perfect imaging. The field must remain finite at resonance, but Equation 7.15 diverges when  $\nu \rightarrow$  integer, unless

$$\sum_{m=1}^{M+1} P_\nu(\zeta_m) (a_m - a'_m) = 0. \quad (7.41)$$

Suppose that all the drains are misaligned and also that all the  $P_\nu(\zeta_m)$  are linearly independent functions. It follows that

$$a'_1 = a_1, \quad a'_m = a_m = 0. \quad (7.42)$$

The device rejects the radiation fed in at the source; none of the detectors fires. Suppose now one drain is aligned with the source, say port number 2. In this case  $\zeta_2 = -\zeta_1$  and  $P_\nu(-\zeta) = (-1)^\nu P_\nu(\zeta)$  for  $\nu \in \mathbb{N}$ . We thus have

$$P_\nu(\zeta_1) [a_1 - a'_1 - (-1)^\nu a'_2] - \sum_{m=3}^{M+1} P_\nu(\zeta_m) a'_m = 0. \quad (7.43)$$

We get,

$$a'_m = 0 \quad \text{for } m > 2, \quad (7.44)$$

and none of the auxiliary detectors fire. The problem reduces itself to the problem of a single drain aligned to a single source as we have seen in previous sections:

$$a'_1 = 0, \quad a'_2 = (-1)^\nu a_1 \quad (7.45)$$

at resonance when  $\nu \in \mathbb{N}$ . The detector array thus perfectly discriminates between the correct image position and the incorrect ones, regardless of the distance between the detectors, *i.e.* not affected by the diffraction limit [7, 9, 10, 12].

Figure 7.5 shows the simplest case: one source facing both one aligned and one misaligned drain. We see that the transmission of the misaligned drain exhibits the characteristic Miñano dips [3], while the transmittance of the aligned drain becomes perfect at the resonances.

However, we must make one important qualification. We need to assume that the  $P_\nu(\zeta_m)$  for all the detectors are linearly independent. However, the function space of the stationary waves on the unit sphere is  $(\nu + 1)$ -dimensional for the following reason: the space is as dimensional as the quantum-mechanical state space of an angular momentum with quantum number  $\nu$  [101] restricted to real wave functions. We thus need to require that the number of detectors does not exceed  $\nu + 1$ , the number of linearly-independent waves at resonance.

#### 7.2.4 Multiple Sources

Which of the imaging properties of the single source will remain valid for multiple sources? Consider first  $M$  sources and one moveable detector, the exact opposite of the situation investigated in section 3. We assign port 1 to the detector and the other ports to the sources, and assume resonance. We see from Equation 7.41 that none of the sources is able to inject radiation,  $a'_m = a_m$ , unless the detector is aligned to one of them. In this case, the corresponding source transmits all of its radiation to the detector. At exact resonance this effect is independent of the distances between the sources (it will be detuned from resonance): the detector is thus able to scan near-field features from

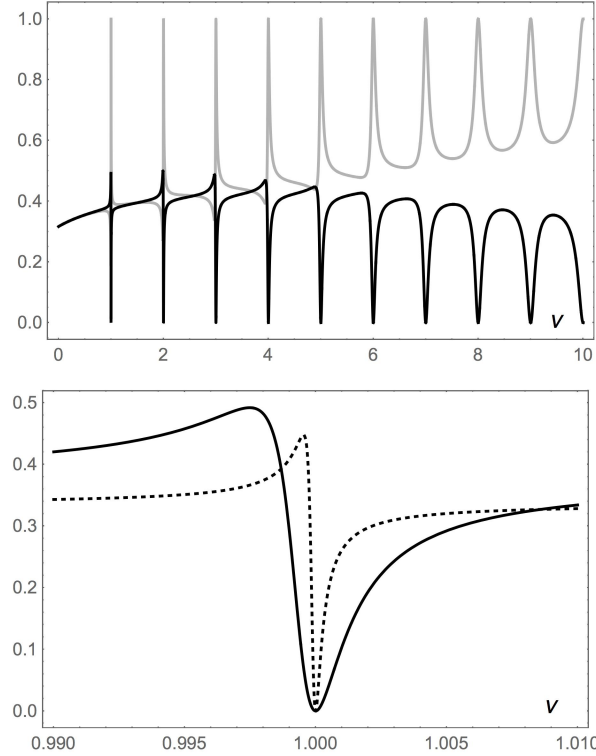


FIGURE 7.5: Miñano dips for multiple drains. Transmission of a single source to two drains (similar to Fig. 7.2), one at the correct imaging position and the other misaligned by the angle  $\delta$  on the virtual sphere. We assume the case of perfect coupling,  $\sigma = 1$ . Top: the black curve shows the transmission through the misaligned drain ( $\delta = 0.1$ ), the light-grey curve the one through the aligned drain. The figure exhibits sharp Miñano dips for sub-wavelength separation, less sharp dips and a growing gap between the two transmission curves for  $\nu\delta > 1/2$ . Bottom: transmission curve of the misaligned drain around a Miñano dip for  $\delta = 0.1$  (solid curve) and  $\delta = 0.05$  (dotted). One sees how the dip narrows for smaller drain separations.

a far-field distance, without the need of switching on the sources selectively, as in the stimulated emission microscopy .

Imagine now several sources with an array of detectors Figure 7.6. Suppose, for example, two sources are placed an angle  $\delta$  apart on the virtual sphere and are observed with a detector array similar to the questionable part of the microwave experiments [5, 8]. There  $\nu = 9.984$ , which was probably too far from the narrow Miñano dip around a resonance. Consider exact resonance. According to Sec. III C the misaligned detectors will not fire; but will the two aligned drains transmit perfectly? Place, without loss of generality, the sources at  $\theta_1 = \pi$ ,  $\theta_2 = \pi + \delta$  and the aligned drains at  $\theta_3 = 0$ ,  $\theta_4 = \delta$ , and all  $\phi_m = 0$ . Figure 7.7 shows the result: the two sources are neither independently nor perfectly transmitted, unless they are farther away than about half a wavelength. Detector arrays interacting with the sources are thus not able to resolve multiple sources closer than the diffraction limit [7, 9, 10, 12].

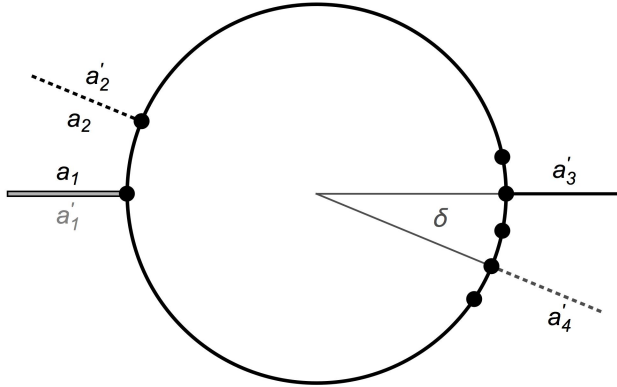


FIGURE 7.6: Multiple sources and array of drains. Two sources with amplitudes  $a_1$  and  $a_2$  are facing an array of drains as in the experiment [5, 8]. At resonance, only the aligned drains transmit with amplitudes  $a'_3$  and  $a'_4$ . Radiation may also leave through the sources with amplitudes  $a'_1$  and  $a'_2$ .

### 7.2.5 Antipodal Fields

We have analysed imaging in the MFE as a scattering problem: the fields incident at the source ports and the lack of them at the drains give rise to the outgoing fields at sources and drains. We have primarily focused on a regime near resonance where we expected — and obtained — some, though not all, of the properties of perfect imaging. Arrays of multiple sources are not perfectly imaged in detector arrays. Yet how do the fields behave?

Consider the field  $\Psi$  given by Equation 7.15 near resonance. Assume an arbitrary number and arrangement of sources and drains. Compare the fields at one position  $z$  with the field at the position that corresponds to the antipodal point on the unit sphere. The antipodes to  $(X, Y, Z)$  reside at  $-(X, Y, Z)$ . We see from the stereographic projection of Equation 7.5 that the antipodal point to  $z$  is  $-1/z^*$ . We see from Equation 7.18 that  $\zeta_m$  is replaced by  $-\zeta_m$  for the antipodal field. As  $P_\nu(-\zeta) = (-1)^\nu P_\nu(\zeta)$  for  $\nu \in \mathbb{N}$  we obtain from Equation 7.15 that

$$\Psi(-1/z^*) = (-1)^\nu \Psi(z). \quad (7.46)$$

The fields at  $z$  and  $-1/z^*$  are thus identical copies, apart from the propagation factor  $(-1)^\nu$ , and without any symmetries in the arrangement of the sources and drains (Figure 7.2 gives already an example). The fields may exhibit sub-wavelength features, for example superoscillations [29] due to a suitable configuration of sources and drains, and yet the fields are perfect copies of each other. A negatively-refractive lens [24] does the same [34]: it copies the field [35]. Perfect imaging with positive refraction thus mimics the imaging with negative refraction. Note, however, that only the fields are copied,

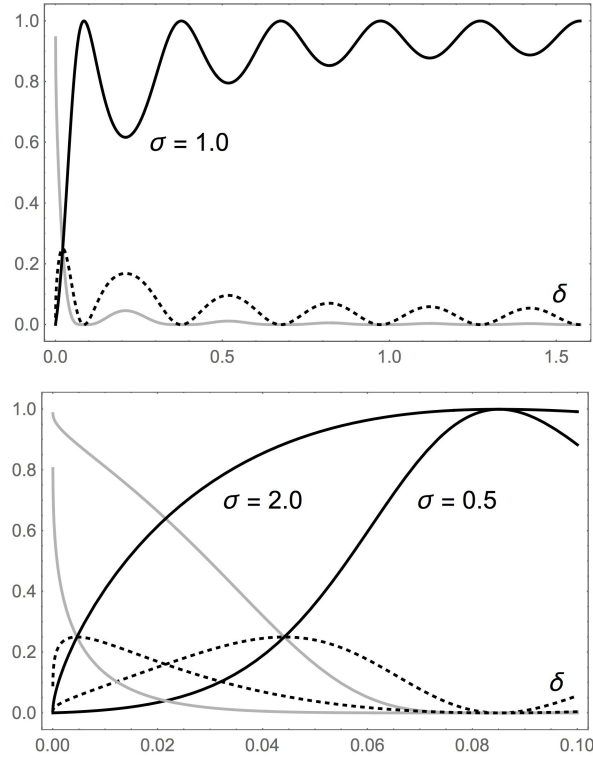


FIGURE 7.7: Two sources, two drains. Transmission of two sources separated by an angle  $\delta$  to two aligned drains as a function of  $\delta$  for  $\nu = 10$ . Only one of the sources is excited ( $a_1 = 1$ ,  $a_2 = 0$ ). The black curves show the transmission  $|a'_3|^2$ , the grey curves the reflected intensity  $|a'_1|^2$ , and the dotted curves  $|a'_2|^2 = |a'_4|^2$ , as indicated in Figure 7.6. Top: beyond the diffraction limit the two drains distinguish the two sources — mostly the correct one transmits. Bottom: for separations smaller than a critical  $\delta$  the transmission curves meet at single points depending on  $\sigma$  and  $\nu$  where they become indistinguishable.

not the sources, and the copies are not recorded in the drains. So this feature, although interesting, is probably of rather limited practical use.

### 7.3 Final Words: Does the Maxwell Fisheye Break the Diffraction Limit?

In the conclusion, we are returning back to the discussion at the end of the Chapter 1, remind the readers, to analyse the resolution of the optical AI devices, such as MFE, and study their imaging perfection in wave regime, we need an applicable measure for perfect focusing applicable in this regime. We end this thesis by providing such a measure whether a system that breaks the diffraction limit. Our measure is based on the definition 1.5. Whether, any of existing optical devices satisfies this condition is subject to examination: theoretically and experimentally.

**Definition 7.1.** An optical device violates the diffraction limit if and only if its point spread function (PSF) is smaller than its own Airy pattern.

To explain the relevance of this criterion, we remind the readers for examining the perfection of an optical device –in the context of our discussion–, one must compare the resolution with the effective wavelength in the medium and not the  $\lambda_0$  of the probing light in vacuum. Unfortunately, taking this point into account, even more, examples of super-resolved devices would exclude from being a candidate for the perfect focusing device. The advantage of our definition is to avoiding such a misinterpretation. The Airy pattern is a particular case of SPF for a simplest aberration free, circular aperture, in fact, Airy pattern is the smallest possible SPF to achieve in a diffraction-limited instrument, even might regard as the perfect image in the astronomical literature. While the radius of the Airy pattern can be calculated by the following formula:

$$r_{\text{Airy}} = 0.61 \frac{\lambda}{\mathcal{N}\mathcal{A}}, \quad (7.47)$$

a true SPF for an unconventional optical device such as AI, needs complicated calculations, sometimes, base on numerical methods. So, based on the classical concepts of optics we provide a measure which applies to a larger category of devices beyond those conventional instruments, particularly, for optical absolute instruments, which is the subject of this thesis. In our research, we studied the imaging property of a particular AI; the Maxwell Fisheye lens. We calculated the PSF for that medium in our paper [60]. For the Maxwell Fisheye, which is highly symmetric, the Airy pattern can be calculated through Fink's definition of diffraction limit, the diameter of the Airy disc for a time reversal focusing system is given by the difference between advanced and retarded Green's function of the system [37]:

$$d_{\text{Fink}} = \frac{1}{2}(G^- - G^+) \quad (7.48)$$

Airy pattern of the MFE is obtain by substituting the Green's function of the MFE,

$$\tilde{D} = \frac{1}{(4\pi)^2} \left( r + \frac{1}{r} \right) \exp [2i\omega \arctan(r)] \quad (7.49)$$

in to the above relation 7.48.

The SPE for the MFE is the asymptotic of its Green's function at the image point:

$$\tilde{D} |_{r \rightarrow \infty} = \frac{1}{(4\pi)^2} \left( r + \frac{1}{r} \right) \exp [2i\omega \arctan(r)] |_{r \rightarrow \infty} \propto \delta(r_0) \quad (7.50)$$

where  $r_0$  denotes the image position. Compare the resulting Airy pattern, which is a finite function, with the SPF for the MFE, a delta function, confirms that, based on

our measure 7.1, the Maxwell Fisheye is a perfect focusing device in wave regime as it is in geometrical optics. However, imaging process is a bit more than focusing. To go from a perfect focusing to the perfect imaging, there are more conditions to satisfy, which in conventional optic systems are trivial. One is the linearity of the system. Most existing optical instruments can not meet the conditions defined in definition 1.5, and those unconventional ones that are able to focus perfectly such as the Maxwell Fisheye, might not be linear. We have shown in this thesis, while the intrinsic properties of MFE leads to a perfect focus for a pair of embedded source and drain, the perfect imaging is not achieved under current circumstances. To have a perfect imaging, one must provide a mechanism for forming an arbitrary image from the multiple ideal image points. In conventional optics, mathematically this mechanism is provided by integration over a proper boundary. However, in the Maxwell Fisheye, the internal interactions between the multiple source/drains ruin this final stage. So Maxwell Fisheye is a perfect focusing device but not a perfect imaging device. Although, being a focusing device, according to the history of diffraction limit, is not a little achievement. The Maxwell Fisheye, already fulfills the requirement in the definition 1.5, for breaking the diffraction limit. In this point, we refer to an argument in [22] about the failure of Maxwell Fisheye based on the results published in [65]. Accordingly, we state that based on any results from Singapore-type experiment [5, 65] which tests the imaging behaviour, one cannot refute the Maxwell Fisheye as perfect focusing device which breaks the diffraction limit, even though this significance, would not have a practical benefit in term of imaging.

# Chapter 8

## Conclusion Chapter

### 8.1 Prospect and Conclusion

“Feynman [6] objected to Abbe’s diffraction limit [7, 9, 10, 12], arguing that as Maxwell’s electromagnetism is a time-reversal invariant, the radiation from a point source may very well become focused in a point drain. Absolute optical instruments [7] such as Maxwell Fisheye [46] can perform the time reversal and may image with perfect resolution [16]. However, the sources and drains in previous experiments [2, 5, 8] were interacting with each other as if Feynman’s drain would act back to the source in the past. Perfect imaging with absolute optical instruments [16, 59] seems therefore restricted by some qualifications: so far it has only worked for a single-source single-drain configuration and near the resonance frequencies of the device. On the other hand, Feynman’s argument appears to be universally valid. What was the problem? In the experiments [2, 5, 8] the sources and drains are interacting with each other. The cables coupling in-and-out microwave radiation to-and-from the device Figure 7.2 They establish an equilibrium of radiation that depends on their transmission and reflection coefficients. In Feynman’s argument, however, the detector ceases to operate when the field is detected, and the drain definitely does not act on the source the future does not act back to the past. An array of detectors can image a point source with arbitrary precision and a single detector can scan an array of near-field sources from a far-field distance with perfect fidelity. However, for this the radiation has to be at resonance and the number of detectors or sources must not exceed the number of waves.

The mutual interaction of sources and drains does ruin some of the promising features of perfect imaging. (We note that different ways of detection might circumvent this feature.) Arrays of sources are not necessarily resolved with arrays of detectors, but it also opens interesting new prospects in scanning near fields from far-field distances. In addition to potential practical applications, the fundamental physics of perfect imaging with interacting sources and drains illustrates how counter intuitive wave propagation

may be. Who would have thought that so much physics is hidden in Maxwell's innocent looking Fisheye?

BIBLIOGRAPHY



# Bibliography

- [1] J. C. Mi nano, R. Marques, J. C. González, P. Benitez, V. Delgado, D. Grabovickic, and M. Freire. Super-resolution for a point source better than  $\lambda/500$  using positive refraction. *New Journal of Physics*, 13(12):125009, 2011.
- [2] J. C. Minano, J. Sanchez-Dehesa, J. C. González, P. Benitez, D. Grabovickic, J. Carbonell, and H. Ahmadpanahi. Experimental evidence of super-resolution better than  $\lambda/105$  with positive refraction. *New Journal of Physics*, 16(3):033015, 2014.
- [3] U. Leonhardt, S. Sahebdivan, A. Kogan, and T. Tyc. A simple model explaining super-resolution in absolute optical instruments. *New Journal of Physics*, 17(5), 2015.
- [4] U. Leonhardt and S. Sahebdivan. Theory of maxwell's fish eye with mutually interacting sources and drains. *Physical Review A*, 92(5):053848, 2015.
- [5] Y. G. Ma, S. Sahebdivan, C K Ong, T. Tyc, and U. Leonhardt. Evidence for sub-wavelength imaging with positive refraction. *New Journal of Physics*, 13(033016), September 2011.
- [6] R. P. Feynman, R. P. Leighton, and M. Sands. *The Feynman Lectures on Physics*, volume 2. Addison-Wesley, San Francisco, 2006.
- [7] M. Born and E. Wolf. *Principle of Optics*. Cambridge University Press, Cambridge, 1999.
- [8] Y. G. Ma, S. Sahebdivan, C K Ong, T. Tyc, and U. Leonhardt. Subwavelength imaging with materials of in-principle arbitrarily low index contrast. *New Journal of Physics*, 14(025001), September 2012.
- [9] E. Abbe. Beitrag zur theorie des mikroskops und der mikroskopischen wahrnehmung. *Archiv fuer mikroskopische Anatomie*, 9(1):413–418, 1873. ISSN 0176-7364.
- [10] E. Abbe. Ueber einen neuen beleuchtungsapparat am mikroskop. *Archiv fuer mikroskopische Anatomie*, 9, 1873.

- [11] H. Fripp. On the limits of the optical capacity of the microscope. *The Monthly Microscopical Journal*, 16(1):15–39, 1876. ISSN 1365-2818.
- [12] E. Abbe. The relation of aperture and power in the microscope. *Journal of the Royal Microscopical Society*, 3(6):790–812, 1883. ISSN 1365-2818.
- [13] The Royal Swedish Academy of Science. Scientific background on the nobel prize in chemistry 2014. 2014. URL [http://www.nobelprize.org/nobel\\_prizes/chemistry/laureates/2014/advanced-chemistryprize2014.pdf](http://www.nobelprize.org/nobel_prizes/chemistry/laureates/2014/advanced-chemistryprize2014.pdf).
- [14] W. S. Hell and J. Wichmann. Breaking the diffraction resolution limit by stimulated emission: stimulated-emission-depletion fluorescence microscopy. *Optics Letter*, 19(11):780–782, 1994.
- [15] T. G. Philbin. Making geometrical optics exact. *Journal of Modern Optics*, 61(7):552–557, 2014.
- [16] U. Leonhardt. Perfect imaging without negative refraction. *New Journal of Physics*, 11(093040), September 2009.
- [17] T. Tyc, L. Herzanova, M. Sarbort, and K. Bering. Absolute instruments and perfect imaging in geometrical optics. *New Journal of Physics*, 13(115004), 2011.
- [18] Bristol Naturalists' Society. *Proceedings of the Bristol Naturalists' Society*. The Society, 1876.
- [19] E. H. K. Stelzer. Light microscopy: Beyond the diffraction limit? *Nature*, 417(6891):806–807, 2002.
- [20] Lord Rayleigh. Investigations in optics, with special reference to the spectroscope. *F.R.S.*, 1879.
- [21] M. E. Testorfand M. A. Fiddy. Superresolution imaging—revisited. *Advances in Imaging and Electron Physics*, 163:165–218, 2010.
- [22] AA Maznev and OB Wright. Upholding the diffraction limit in the focusing of light and sound. *arXiv preprint arXiv:1602.07958*, 2016.
- [23] A. Neice. Chapter 3 - methods and limitations of subwavelength imaging. In P. W. Hawkes, editor, *Advances in Imaging and Electron Physics*, volume 163 of *Advances in Imaging and Electron Physics*, pages 117 – 140. Elsevier, 2010.
- [24] J. Pendry. Negative refraction makes a perfect lens. *Phys. Rev. Lett.*, 85:3966–3969, Oct 2000.

- [25] D. R. Smith, J. Pendry, and M. C. K. Wiltshire. Metamaterials and negative refractive index. *Science*, 305(5685):788–792, 2004.
- [26] V. G. Veselago. The electrodynamics of substances with simultaneously negative values of  $\epsilon$  and  $\mu$ . *Sov. Phys.-Usp.*, 10(4):509, 1968.
- [27] J. de Rosny, , and M. Fink. Overcoming the diffraction limit in wave physics using a time-reversal mirror and a novel acoustic sink. *Phys. Rev. Lett.*, 89:124301, 2002.
- [28] S. Quabis, R. Dorn, M. Eberler, O. Glueckl, and G. Leuchs. Focusing light to a tighter spot. *Optics Communications*, 179:1 – 7, 2000. ISSN 0030-4018.
- [29] E. T. F. Rogers, J. Lindberg, T. Roy, S. Savo, J. E. Chad, M. R. Dennis, and N.I. Zheludev. A super-oscillatory lens optical microscope for subwavelength imaging. *Nature materials*, 11(5):432–435, 2012.
- [30] C. Caloz and T. Itho. *Electromagnetic Metamaterials: Transmission Line Theory and Microwave Applications*. Wiley, 2006.
- [31] J. M. Williams. Some problems with negative refraction. *Physical Review Letters*, 87(p. 249703), 2001.
- [32] D. R. Smith, D. Schurig, M. Rosenbluth, and S. Schultz. Limitations on sub-diffraction imaging with a negative refractive index slab. *Applied Physics Letters*, 82, 2003.
- [33] M. Stockman. Criterion for negative refraction with low optical losses from a fundamental principle of causality. *Phys. Rev. Lett.*, 98:177404, Apr 2007.
- [34] U. Leonhardt and T. G. Philbin. General relativity in electrical engineering. *New Journal of Physics*, 8(10):247, 2006.
- [35] U. Leonhardt and T. G. Philbin. *Geometry and light, The Science of invisibility*. Dover Publications Inc., Mineola, New York, 2010.
- [36] G. Lepage, J. De Rosny, A. Tourin, and M. Fink. Focusing beyond the diffraction limit with far-field time reversal. *Science*, 315(5815):1120–1122, 2007.
- [37] G. Lepage, J. De Rosny, A. Tourin, A. Derode, G. Montaldo, and M. Fink. Time reversal of electromagnetic waves. *Physical review letters*, 92(19):193904, 2004.
- [38] Jerzy F Plebański. On the separation of einsteinian substructures. *Journal of Mathematical Physics*, 18(12):2511–2520, 1977.
- [39] A. J. Ward and J. Pendry. Refraction and geometry in maxwell's equations. *Journal of Modern Optics*, 43(4):773–793, 1996.

- [40] J. Pendry, D. Schurig, and D. R. Smith. Controlling electromagnetic fields. *science*, 312(5781):1780–1782, 2006.
- [41] U. Leonhardt. Optical conformal mapping. *Science*, 312(5781):1777–1780, 2006.
- [42] T. G. Philbin, C. Kuklewicz, S. Robertson, S. Hill, F. König, and U. Leonhardt. Fiber-optical analog of the event horizon. *Science*, 319(5868):1367–1370, 2008.
- [43] D. A. Genov, S. Zhang, and X. Zhang. Mimicking celestial mechanics in metamaterials. *Nature Physics*, 5(9):687–692, 2009.
- [44] C. Sheng, H. Liu, Y. Wang, S. N. Zhu, and D. A. Genov. Trapping light by mimicking gravitational lensing. *Nature Photonics*, 7(11):902–906, 2013.
- [45] D. M. Shyroki. Note on transformation to general curvilinear coordinates for maxwell’s curl equations (is the magnetic field vector axial?). *arXiv preprint*.
- [46] J. C. Maxwell. *Camb. Dublin Math. J.*, (8 188), 1854.
- [47] R. K. Luneburg. *Mathematical Theory of Optics*. University of California Press, Berkeley, Ca, 1964.
- [48] Yu. N. Demkov, V. N. Ostrovskii, and N. B. berezina. Uniqueness of the firsov inversion method and focusing potentials. *Soviet Physics JETP*, 33(5), 1971.
- [49] P. Kinsler. Active drains and causality. *Physical Review A*, 82(055804), 2010.
- [50] Chen T. Tai. Maxwell fish-eye treated by maxwell equations. *Nature*, 182(1600), 1958.
- [51] Chen T. Tai. *Dyadic Green’s Functions in Electromagnetic Theory*. Intext Educational Publishers, College Devision of Intext, Scranton, San Francisco, Toronto, London, 1971.
- [52] T. Tyc and A. Danner. Frequency spectra of absolute optical instruments. *New Journal of Physics*, 14(085023), 2012.
- [53] V. Perlick. On fermat’s principle in general relativity. ii. the conformally stationary case. *Class. Quantum Grav.*, 7, 1999.
- [54] T. Needham. *Visual Complex Analysis*. Clarendon, Oxford, 2002.
- [55] P. Benitez, J. C. Mi nano, and J. C. González. Perfect focusing of scalar wave fields in three dimensions. *Optics Express*, 18(8), 2010.
- [56] R. Szmytkowski. Focusing properties of maxwell’s fisheye medium. *Journal of Physics A: Mathematical and Theoretical*, 44(6), 2011.

- [57] R. Szmytkowski. Focusing properties of maxwell's fisheye medium. *ArXiv preprint*, 131(1107.1768), 2011.
- [58] L. A. Pazynin and G.O. Kryvchikova. Focusing properties of maxwell's fisheye medium. *Progress In Electromagnetics Research*, 131, 2012.
- [59] U. Leonhardt and T. G. Philbin. Perfect imaging with positive refraction in three dimensions. *Phys. Rev. A*, 81:011804, 2010.
- [60] U. Leonhardt and S. Sahebdivan. Perfect imaging: they do not do it with mirrors. *Journal of Optics*, 13(02401), January 2011.
- [61] W. Ch. Chew. *Waves and Fields in Inhomogeneous Media*. IEEE Press, NewYork, 1995.
- [62] V. M. Redkov, N.G. Tokarevskaya, and E.M. Bychkouskaya. Maxwell equations in riemannian space-time, geometrical modeling of medias. *Nonlinear Dynamics and Applications*, 13, 2006.
- [63] T. Mo, , and C. Papas. Electromagnetic field and wave propagation in gravitation. *Phys. Rev. D*, 3:1708–1712, 1971.
- [64] J. D. Jackson. *Classical Electrodynamics*. Whily, Newtork, 1998.
- [65] S. He, F. Sun, S. Guo, S. Zhong, L. Lan, W. Jiang, Y. G. Ma, and T. Wu. Can maxwell's fisheye lens really give perfect imaging? part iii. a careful reconstruction of the “evidence for subwavelength imaging with positive refraction”. *PIER*, 152(12):1–15, 2015.
- [66] R. J. Blaikie. Perfect imaging without refraction? *New Journal of Physics*, 13(125006), 2011.
- [67] J. C. Minano, P. Benitez, and J. C. González. Perfect imaging with geodesic waveguides. *New Journal of Physics*, 12(123023), 2010.
- [68] O. Quevedo-Teruel, R. C. Mitchell-Thomas, and Y. Hao. Frequency dependence and passive drains in fish-eye lenses. *Physical Review A*, 86(053817), 2012.
- [69] J. C. Minano, P. Benitez, and J. C. González. *ArXiv preprint*.
- [70] U. Leonhardt and S. Sahebdivan. (private communications). private communications, 12 2014.
- [71] D. Grabovickic, J. C. González, J. C. Minano, and P. Benitez. Analysis of super imaging properties of spherical geodesic waveguide using comsol multyphiscs. In *Proceedings of the COMSOL Conference in Milan*, 2012.

- [72] J. C. Mi nano, P. Benitez, and J. C. González. Focusing properties of maxwell's fisheye medium. *New J. Phys.*, 12(123023), 2010.
- [73] D. Schurig, J. J. Mock, B. J. Justice, S. A. Cummer, A. F. Starr J Pendry, and D. R. Smith. Metamaterial electromagnetic cloak at microwave frequencies. *Science*, 314(5801), 2006.
- [74] Y. G. Ma, C K Ong, T. Tyc, and U. Leonhardt. An omnidirectional retroreflector based on the transmutation of dielectric singularities. *Nat. Mater.*, 8(639), 2009.
- [75] D. R. Smith and J. Pendry. Homogenization of metamaterials by field averaging. *Journal of the Optical Society of America B*, 23, 2006.
- [76] R. Marques, M. J. Freire, and J. D. Baena. Theory of three-dimensional subdiffraction imaging. *Appl. Phys. Lett.*, 89(211113), 2006.
- [77] S. Cornbleet. *The Optics of Microwave Antenna Design*. London: Academic, 1976.
- [78] L. Zhao, X. Chen, and C K Ong. Visual observation and quantitative measurement of the microwave absorbing effect at x band. *Rev. Sci. Instrum.*, 79(124701), 2008.
- [79] R. J. Blaikie. Comment on "perfect imaging without negative refraction". *New Journal of Physics*, 12(058001), 2010.
- [80] U. Leonhardt. Reply to comment on "perfect imaging without negative refraction". *New Journal of Physics*, 12(058002), 2010.
- [81] U. Leonhardt. Reply to comment on "perfect imaging without negative refraction". *New Journal of Physics*, 13(028002), 2011.
- [82] P. Kinsler and A. Favaro. Comment on "reply to comment on 'perfect imaging without negative refraction'". *New Journal of Physics*, 13(028001), 2011.
- [83] R. Merlin. Comment on "perfect imaging with positive refraction in three dimensions". *Physical Review A*, 82(057801), 2010.
- [84] U. Leonhardt and T. Philbin. Reply to comment on "perfect imaging with positive refraction in three dimensions". *Physical Review A*, 82(057802), 2010.
- [85] R. Merlin. Maxwell's fish-eye lens and the mirage of perfect imaging. *Journal of Optics*, 13(024017), 2011.
- [86] T. Tyc and A. Danner. Resolution of maxwell's fisheye with an optimal active drain. *New Journal of Physics*, 16(063001), 2014.
- [87] J. C. González, P. Benítez, and J. C. Mi nano. Perfect drain for the maxwell fish eye lens. *New J. Phys.*, 13(2), 2011.

- [88] J. C. González, D. Grabovičkić, P. Benítez, and J.C. Mi nano. Circuital model for the spherical geodesic waveguide perfect drain. *New J. Phys.*, 14(8), 2012.
- [89] L. Xu and H. Chen. Coherent perfect absorber makes a perfect drain for maxwell's fish-eye lens. *Europhys. Lett.*, 100(3):34001, 2012.
- [90] Y. Ma, T. Wu, and C K Ong. Subwavelength drains designed for mirror-closed dielectric lenses. *J. Opt.*, 15, 2013.
- [91] L. D. Landau and E. M. Lifshitz. *The Classical Theory of Fields*. Pergamon, Oxford, 1975.
- [92] T. Tyc and X. Zhang. Forum optics: Perfect lenses in focus. *Nature*, 480(0):42, 2011.
- [93] F. Sun and S. He. Can maxwell's fisheye lens really give perfect imaging? *PIER*, 108:307, 2010.
- [94] F. Sun, X.C. Ge, and S. He. Can maxwell's fisheye lens really give perfect imaging? part ii. the case with passive drains. *PIER*, 110:313, 2010.
- [95] J. A. Arnaud. Degenerate optical cavities. iii: Effect of aberrations. *Appl. Opt.*, 9 (5):1192–1200, 1970.
- [96] E. A. Ash and G. Nichols. Super-resolution aperture scanning microscope. *Nature*, 237:510, 1972.
- [97] U. Leonhardt. Quantum physics of simple optical instruments. *Rep. Prog. Phys.*, 66(7):1207, 2003.
- [98] M. Reck, A. Zeilinger, H. J. Bernstein, and P. Bertani. Experimental realization of any discrete unitary operator. *Phys. Rev. Lett.*, 73:58, 1994.
- [99] T. Tyc and M. Sarbort. Spherical media and geodesic lenses in geometrical optics. *Journal of Optic*, 14(7), 2012.
- [100] A. Erdélyi, W. Magnus, F. Oberhettinger, and F. G. Tricomi. *Higher Transcendental Functions*. McGraw-Hill, New York, 1981.
- [101] L. D. Landau and E. M. Lifshitz. *Quantum Mechanics*. Pergamon, Oxford, 1977.
- [102] N. Garcia and M. Nieto-Vesperinas. Left-handed materials do not make a perfect lens. *Phys. Rev. Lett.*, 88:207403, May 2002.